MULTI-MODALITY MAGNETIC RESONANCE IMAGING IN TYPICAL AND ATYPICAL DEVELOPMENTAL HUMAN BRAIN

by

MINHUI OUYANG

DISSERTATION

Submitted in partial fulfillment of the requirements
for the degree of Doctor of Philosophy at
The University of Texas at Arlington
December, 2016

Arlington, Texas

Supervising Committee:

- Hao Huang, Supervising Professor
- Georgios Alexandrakis
- Hanli Liu
- Lina Chalak
- Matthew W. Mosconi

Acknowledgements

I have a great number of people in my life to thank for their support, inspiration and encouragement that have shaped my path, and without them the present work would not have been possible. First and foremost, I would like to thank my Ph.D. supervisor and mentor, Dr. Hao Huang, for his continuous support, advice and patience throughout my graduate studies. I really appreciate him giving me the opportunity to be his student and learn from him. The countless fruitful and productive discussions with him helped me grow academically and professionally in the field of neuroimaging.

I would also like to thank my remaining committee members for their suggestions and support. Dr. George Alexandrakis, Dr. Hanli Liu, Dr. Lina Chalak and Dr. Matthew W. Mosconi took the time and patience to understand my projects. A special thanks to Dr. Hanli Liu, who has provided great support to me from the first day of the graduate school as my program track advisor.

I thank past and present lab members, Virendra Mishra, Tina Jeon, Austin Ouyang, Qiaowen Yu, Hang Li, Qinmu Peng, Huiying Kang, Qinlin Yu, Lei Feng and Jennifer Muller, for the interesting discussions with them and also making my time in the lab more enjoyable.

I would like to thank all past and present faculties and graduate students at Advanced Imaging Research Center (AIRC) in University of Texas Southwestern Medical Center (UTSW), the MEG lab at Radiology Research in Children’s Hospital of Philadelphia. Particularly, I am grateful to Dr. Hanzhang Lu and Dr. Peiying Liu for sharing their time and expertise.

Additionally, I am in debt to my good friends: Xixi Wen, Yue Ding, Cherry Song, Jingyuan Chen, Yujing Wang, Ting Liu and Jingjing Li, for their continued encouragement, support during the tough days. I thank my parents for their

unconditional love and encouragement that allowed me to pursuing my passion in science.

Abstract

MULTI-MODALITY MAGNETIC RESONANCE IMAGING IN TYPICAL AND ATYPICAL DEVELOPMENTAL HUMAN BRAIN

MINHUI OUYANG, Ph.D.

The University of Texas at Arlington, 2016

Supervising Professor: Hao Huang

Human brain development is structurally and functionally a nonlinear process and even with the tremendous advancements in the field of neuroimaging based on Magnetic Resonance Imaging (MRI) several significant questions remain un-answered. Although brain change and adaption are part of a lifelong process, the earliest phases of maturation, especially from birth to early childhood, are perhaps the most dramatic and important. During this early developmental period, the structural and functional organization of the brain are continuously shaped by a combination of synaptogenesis, dendritic arborization, myelination and synaptic pruning. The current research aims to use more recently developed MRI techniques of diffusion magnetic resonance imaging (dMRI) and arterial spin labeling (ASL) to study brain maturation processes in typical and atypical development. The present body of work includes the study of brain functional development and correlation between functional changes with structural changes during early development (3rd trimester), and structural changes during later development in typical and atypical condition (autism spectrum disorder (ASD)).

The first project (Chapter 2) studies the brain functional development, and relationship between functional changes and the cortical microstructure changes during the early stages of development (3rd trimester). To estimate the functional changes, pseudo-continuous ASL (pCASL*) method was used,* which quantifies the cerebral blood flow (CBF). The adult-pCASL protocol is not optimal in the extremely slow blood flow in the brains of neonate population, which was specifically optimized for this study. To measure the cortical microstructure changes, we used dMRI to estimate fractional anisotropy (FA) on cortical skeletonized level. Based on the data acquired from 34 subjects, the global CBF measurement was found to double its value during third 3^{rd} trimester. These CBF increase was heterogeneous across the brain, with significantly higher rate of CBF increase in the frontal lobe than in the occipital lobe. Moreover, the increasing CBF observed in frontal lobe corresponded to lower FA values in the same region, which suggests the dendritic arborization and synaptic formatting might be associated with an elevation of local CBF.

In the second project (Chapter 3), dMRI was used to study the structural changes in a cohort of children with typical developing (TD) and ASD. The deep white matter (WM) voxels were surveyed to detect differences in WM microstructural development between 31 children with ASD ages of 2-7 years and 19 age-matched children with TD, using FA and radial diffusivity (RD) measures from dMRI. The anatomical locations, distribution, and extent of the core WM voxels with atypical age-dependent changes in a specific tract or tract group were delineated and evaluated by integrating the skeletonized WM with a digital atlas. Exclusively, unidirectional FA increases and RD decreases in widespread WM tracts were revealed in children with ASD before 4 years, with bi-directional changes found for children with ASD of 2-7 years. Compared to progressive development that raised FA and lowered RD during 2-7 years in the TD group, flattened curves of WM maturation were found in multiple major WM tracts of all five tract groups, particularly associational and limbic tracts, in the ASD group with trend lines of ASD and TD crossed around 4 years.

Finally, a novel attempt to estimate superficial WM or short-range association fibers (SAF) in typically and atypically developmental human brain is proposed in the

Chapter 4. A lot has been well characterized and understood about deep WM or long-range association fibers (LAF) in early brain development using dMRI, but very little is known about SAF. The normalized SAF (NSAF) index, defined as the ratio of the number of SAF to the number of cortico-cortical connectivity fibers (sum of SAF and LAF) traced from a given cortical gyrus based on dMRI tractography, was proposed to characterize the SAF development. Initially, dMRI data from in 21 healthy subjects, aged 2-25 years, was used to study the typically developmental trajectories of NSAF. The NSAF showed spatiotemporal heterogeneity, decreasing in early childhood and increasing with age, with lowest NSAF reached at various ages among different cortical gyri. Then, NSAF was also applied to data from to 31 children with ASD aged 2-7 years and 19 age-matched children with TD to explore its sensitivity under pathological condition. The decrease of whole brain NSAF was highly correlated with global network efficiency increase (calculated from structural network based on graph theory) in young children with TD but not with ASD, indicating the important role of balance between SAF and LAF during the brain network reconfiguration process. Moreover, significant age-dependent NSAF in prefrontal and default-mode network hub regions were observed in TD but not ASD group.

In conclusion, the present research work demonstrates the feasibility of using ASL to study the regional CBF of neonates during 3rd trimester under normal or pathological conditions (e.g. hypoxic-ischemic encephalopathy or neonatal congenital heart disease) on a 3T MRI scanner. Secondly, the work showed the atypical age-dependent changes of FA and RD widely in ASD and these converging findings from both group comparisons at different age ranges and trajectory analyses may help elucidate the seemingly non-uniform WM finding of children with ASD reported in prior studies. Last, altered maturation of short-range connection in higher-order brain regions were found in children with ASD, which may offer structural basis for the functional over-

connectivity of short-range connection in ASD and also suggest the NSAF could be a potential biomarker for delineation normal brain development and diagnosis of several mental disorders.

Dec. 03, 2016

Table of Contents

List of Illustrations

List of Tables

Chapter 1

Introduction

1.1 Significance of the dynamic time-course of early brain development

The human brain, which is arguably the most complex structure in our body, contains more than 100 billion neurons that communicate with each other via axons and form neural networks (Mori and Zhang, 2006). It represents about 2% of the total body weight, but accounts for over 20% of the total energy expenditure of the human body (Attwell and Laughlin, 2001). The dynamic course of brain development is one of the most fascinating aspects of the human condition. Although change and maturation of brain is a lifelong process, the earliest phases of development, from birth to early childhood, are perhaps the most dramatic and important (Toga et al., 2006). During this early developmental period, the structural architecture, functional organization and network configuration of the brain are continuously shaped by a sequence of events, including synaptogenesis, dendritic arborization (Bystron et al., 2008; Hunttenlocher, 1979), myelination (Benes et al., 1994; Yakovlev and Lecours, 1967) and synaptic pruning (Huttenlocher 1974, 1990).

These dynamic changes during early brain development have been extensively studied using histological approaches. Prior studies have found synaptic overproduction in infancy, persistence of high levels of synaptic density to childhood, followed by a decrease after later childhood (e.g. Huttenlocher et al., 1982, 1990; Petanjek et al., 2011). These histological work showed that the time-course for synaptic blooming and pruning in the human brain varies tremendously by brain region. Specifically, in the visual cortex, synaptic overproduction reaches a peak at about fourth postnatal month, then followed by the synapse elimination process until preschool age. However, in the frontal cortex, a brain region involved in executive, attentional and cognitive functions, synaptic density reaches a maximum at a later age of 3-4 years old. Perturbation of these typical dynamic courses may cause psychiatric disorders, such as autism spectrum disorder (ASD) (e.g. Courchesne et al., 2007), attention-deficit hyperactivity disorder (ADHD) (e.g. Sowell et al., 2003; Shaw et al., 2007) and very early childhood onset schizophrenia (COS) (e.g. Thompson et al., 2001; Gogtay et al., 2008).

1.2 The role of advanced neuroimaging to study brain development

Histological evidence suggests that brain development or maturation is a dynamic process of progressive and regressive changes. However, such an approach is invasive, labor-intensive and destructive by nature, and hence, is a non-ideal choice for examining the whole brain pattern or performing quantitative analyses and also not a practical approach for clinical diagnosis or evaluation. By contrast, magnetic resonance imaging (MRI) methods are uniquely capable to noninvasively provide high-resolution structural and functional images. More recently the development of diffusion MRI (dMRI) and perfusion MRI (pMRI), provide unique functional and structural markers of brain.

These structural and functional MR imaging methods hold the potential to provide new insights into the sequence and timing of both typically and atypically brain developmental processes. For example, structural MRI (e.g. T1-wighted images) in typically developing children and adolescents demonstrate increasing white matter (WM) volume and inverted U-shape gray matter (GM) volumes trajectories (e.g. Sowell et al., 2001, 2004; Lenroot et al., 2007; Gogray et al., 2004). With dMRI, the rapid pace of maturation process of deep WM (WM integrity) (e.g. Mukherjee et al., 2002; Partidge et al., 2004; Schneider et al., 2004; Huppi et al., 1998; Lebel et al., 2002) and structural network (e.g Hagmann et al., 2010; Huang et al., 2015; Yap et al., 2011) of human brain from birth to adult has been observed. And pMRI has been used to study the brain physiology during development (e.g. Jain et al., 2012; Wang et al., 2003). In the following section, a short introduction about dMRI and pMRI is provided (section 1.3-1.4), then the objectives of the present work are discussed (section 1.5).

1.3 Diffusion magnetic resonance imaging (dMRI)

Diffusion, also known as Brownian motion, refers to random movement of water and other small molecules due to thermal collisions. For most fluids and some solid materials such as gels, diffusion is isotropic (same in every direction) and can be characterized by a single diffusion coefficient (D), with a unit of area/time (mm^2/s). For biological tissues, which are highly structured such as the nervous system tissues, diffusion is anisotropic and varies along different directions. Diffusion MRI, a non-invasive MRI technique, can be used to investigate the diffusion property of water molecules by performing a series of experiments with different diffusion-weighting factor (b), with a unit of time/area (s/mm^2).

1.3.1 Basics of diffusion MRI (dMRI)

To better understand how to measure diffusion by MRI, we first need to know the information we obtained from MRI is based on proton signal intensity. A simplified equation for the contribution of these physical properties of water molecules, proton density (PD), T_1 and T_2 relaxation times, and the diffusion coefficient (D) to MR signal (S) in a spin-echo image is shown:

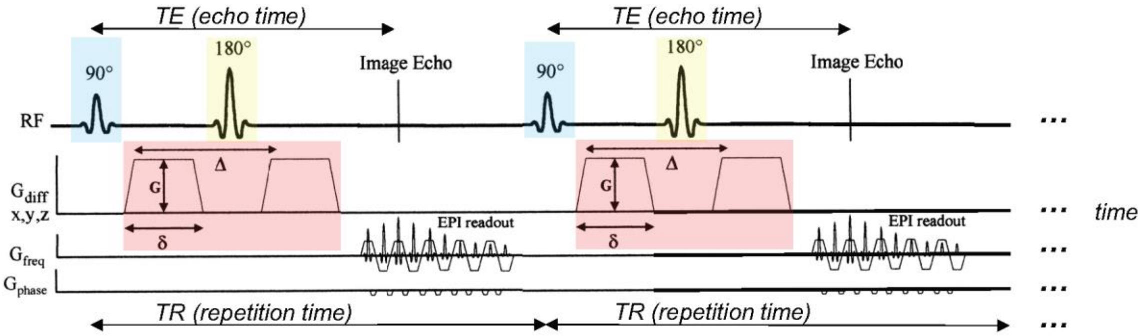

Figure 1.1: A diagram of diffusion MRI (dMRI) pulse sequence with single-shot echo-planar imaging (EPI) as readout module. The 90^o pulse is excitation pulse (in blue shade), then followed by a dephase gradient (the 1st diffusion gradient in pink shade).

After a 180^o refocusing pulse (in yellow shade), there is a rephrase gradient (the 2nd diffusion gradient in pink shade).

$$S = PD * \left(1 - e^{-\frac{TR}{T1}}\right) * e^{-\frac{TE}{T2}} * e^{-bD} \qquad (1.1)$$

where *TR* (repetition time) and *TE* (echo time) are related to the timing of the radio-frequency (RF) pulse and *b* value is diffusion-weighted factor, which reflects the strength and timing of a pair of pulsed field gradients to generate diffusion weighted images (Figure 1.1). The *b*-value determines the degree of diffusion weighting. The higher *b* value, the stronger the diffusion effects. Here, signal intensity from water (S) is the information we obtain from MR scanner; *TR, TE,* and *b* are imaging parameters that we can control, and by changing these parameters we can get different contribution (contrast) of PD, T_1, T_2, and D terms to the signal. In the dMRI sequence, there are two strong gradient pulses (dephase gradient and rephrase gradient, shown in pink-shade in Figure 1.1) of magnitude (*G*) and duration (δ), separated by time interval (Δ). The imaging parameter, *b* value, depends on these two pulsed gradients' strength, duration, and spacing and can be calculated using equation 1.2:

$$b = \gamma^2 G^2 \delta^2 (\Delta - \delta/3) \qquad (1.2)$$

Here, γ is the gyromagnetic ratio of water, which is 42.58 MHz/Tesla. If we perform two experiment and obtain two images with different *b* values (b_1 and b_2) while keep other imaging parameters (*TR* and *TE*) the same, we can retrieve information about the diffusion coefficient, *D*, from following equation (Stejskal and Tanner, 1965):

Experiment 1: $S_1 = PD * \left(1 - e^{-\frac{TR}{T1}}\right) * e^{-\frac{TE}{T2}} * e^{-b_1 D} = S_0 * e^{-b_1 D}$

Experiment 2: $S_2 = PD * \left(1 - e^{-\frac{TR}{T1}}\right) * e^{-\frac{TE}{T2}} * e^{-b_2 D} = S_0 * e^{-b_2 D}$

Since PD, TR, and TE are unchanged in these two experiments, the signal intensity related to them are simplified as S_0 here. Based on these two different signal intensities (S_1 and S_2), the diffusion coefficient, D, can be estimated using following equation:

$$D = -\ln\left(\frac{S_2}{S_1}\right)/(b_2 - b_1) \tag{1.3}$$

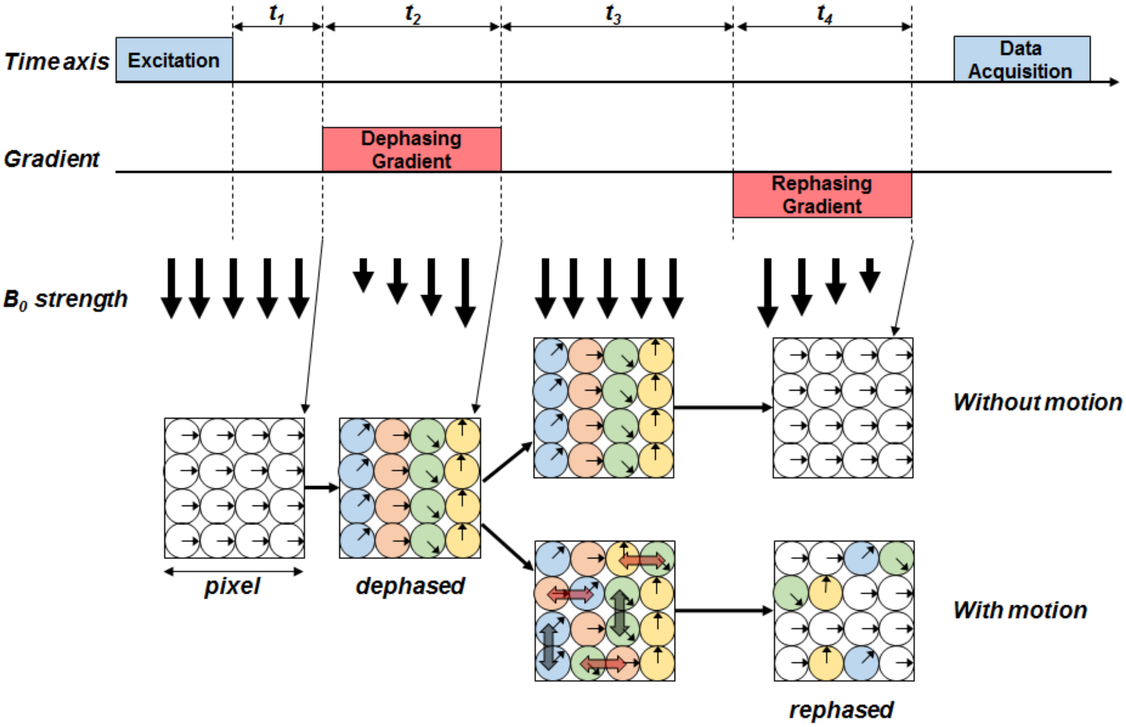

Figure 1.2: A schematic diagram to explain the relationship between water molecules motion and *dephase-rephase* gradient application. Each circle represents water molecules (spins) at different locations within a pixel. Thick vectors indicate the strengths of magnetic field strength (B_0), and small vectors in the circles indicate phases of MR signals from water molecule at each location. If water molecules move in between two gradient application, time interval t_3, the second gradient cannot refocus the phase perfectly, which results in signal losing. In this example, horizontal motion (same direction as applied gradient) leads to the signal loss, but vertical motion does not affect signal intensity (Mori and Zhang, 2006; Mori, 2007)

In the diffusion measurement, the phase difference is used to detect water motion. Figure 1.2 shows an example to explain the relationship between water molecules motion and dephase-reshape pulsed gradient in the diffusion weighted MR signal measuring. Each circle represents water molecules, located in different regions within a pixel. After the excitation pulse and during the time interval t_1, all water molecules are with the same phase and aligned to the main magnetic field (B_0). Then, a dephasing gradient is applied with a time interval of t_2. During this dephasing gradient period, water molecules will experience different magnetic field strengths because of their location difference along the direction of dephasing gradient. This will induce a gradient of signal phase across the sample (all water molecules here). Due to these out-of-phase spins, the signal received at the MR coil will be less. When the dephasing gradient is off, during time interval t_3, water molecules (spins) experience the same magnetic field strength again. However, these spins are not with the same phase and signal received is still less due to previous dephasing gradient. Then, a rephrasing gradient (same gradient strength and interval as dephasing gradient with opposite polarity) is applied (time interval t_4) for the phase refocusing across sample (rewinding of the phase). The refocusing will be perfect if water molecules are not moved between the two-pulsed gradients. However, if there is translation motion (diffusion) of these water molecules (indicated as red arrows in Figure 1.2), such perfect refocusing would not occur. Since the signal intensity in each pixel is obtained as sum of the signals from all water molecules within it, the imperfect refocusing (water diffusion) will lead to signal loss. In this way, we can detect the water molecules diffusion process by applying a pair of gradient pulses.

In equation 1.2, we need two different *b*-values to determine a diffusion coefficient in each pixel. Usually, $b_1 \approx 0\ (s/mm^2)$ is applied as non-diffusion weighted image (S_0). With a second *b* value applied, a diffusion weighted image is obtained. Due to the water molecules motion, this diffusion-weighted image has a lower signal intensity than the S_0. By solving the equation 1.2 in each pixel, a map of diffusion coefficient, which is called as apparent diffusion coefficient (ADC) map, can be obtained. This ADC map reflects not only true diffusion, but depends on spatial orientation of the diffusion gradient (such as horizontal direction in Figure 1.2), microscopic perfusion, bulk tissue motion and also pulse sequence timing.

1.3.2 From dMRI to diffusion tensor imaging (DTI)

From Figure 1.2, we know the ADC measurement by MRI is that it detects the water molecules' motion only along the applied gradient axis (horizontal versa vertical directions in Figure 1.2). In the brain tissue, which are highly structured, the water molecules move more easily along axonal fibers and the fiber orientation should be similar to the measurement orientation with the largest ADC. Here comes a question: how to estimate the orientation with the largest ADC value? Theoretically, we can accurately find the orientation with the largest ADC value by measuring the diffusion along thousands of axes. However, this is not a practical way. To simplify this, the diffusion tensor concept was introduced (Basser et al., 1994). In this diffusion tensor model, diffusion measurements from different orientation are fitted to a three-dimensional ellipsoid. In the diffusion tensor imaging (DTI), we use the anisotropy, which can be characterized by diffusion tensor (a 3×3 matrix, equation 1.4), to estimate the axonal organization inside the brain. Namely, the water molecule should move more easily along the axonal bundles rather than perpendicular to them, because there are fewer obstacles to prevent movement along the fibers.

$$D = \begin{bmatrix} D_{xx} & D_{xy} & D_{xz} \\ D_{yx} & D_{yy} & D_{yz} \\ D_{zx} & D_{zy} & D_{zz} \end{bmatrix} \tag{1.4}$$

Here, the tensor in equation 1.4 can be represented as a three-dimensional ellipsoid where $D_{xx}, D_{yy}\ and\ D_{zz}$ represent diffusion along $x, y\ and\ z$ directions and the off-diagonal elements represent diffusion along i, j direction with $i\ or\ j = x, y\ and\ z$ direnctions. The tensor is symmetric with $D_{ij} = D_{ji}$, and there are 6 independent elements which have to be determined in order to estimate the tensor. The properties of the 3D ellipsoid, namely, the length of longest, middle and shortest axes (also called eigenvalues in the tensor, $\lambda_1, \lambda_2\ and\ \lambda_3$) and the orientations of these three axes (also called eigenvectors in the tensor,$v_1, v_2\ and\ v_3$). If diffusion is isotropic, all the eigenvalues are equal. The eigenvalues and eigenvectors of the tensor can be determined by singular value decomposition (SVD) algorithm. Diffusion in the brain white matter is predominantly in the direction parallel to the underlying axonal fibers instead of perpendicular to them, and DTI can be used to study these complex white matter architectures noninvasively (Jones et al., 1999).

1.3.3 Quantitative measurements derived from DTI

Once the eigenvalues ($\lambda_1, \lambda_2\ and\ \lambda_3$) and eigenvectors ($v_1, v_2\ and\ v_3$) are obtained at each pixel, there are several contrasts or measurements can be generated. Figure 1.3 shows an example of DTI-derived measurements in the human brain from a healthy individual.

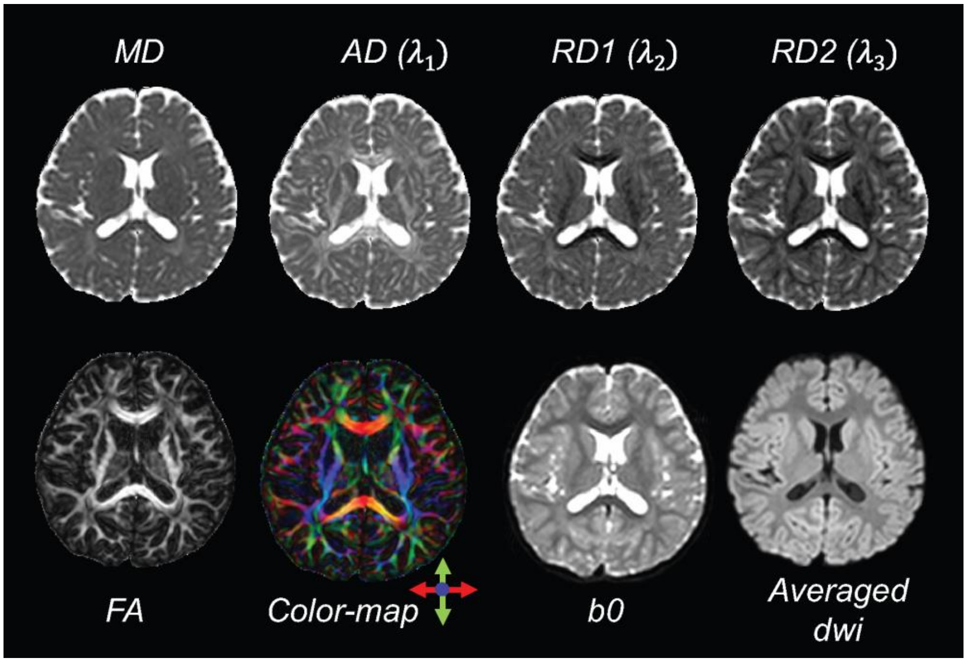

Figure 1.3: An example of measurements derived from diffusion tensor imaging (DTI). In the upper panel: mean diffusivity (MD, axial diffusivity (AD, represented by primary eigenvalue) and two radial diffusivities (RD, second and third eigenvalues). In the lower panel: fractional anisotropy (FA), color-map (color-encoded primary eigenvector

orientation map), b0 image (non-diffusion-weighted) and averaged diffusion-weighted images (dwi).

Fractional anisotropy (FA), a measurement to characterize the shape of 3D ellipsoid with no unit, can be calculated as (Pierpaoli and Basser, 1996):

$$FA = \sqrt{\frac{1}{2}} * \frac{\sqrt{(\lambda_1 - \lambda_2)^2 + (\lambda_2 - \lambda_3)^2 + (\lambda_3 - \lambda_1)^2}}{\sqrt{\lambda_1^2 + \lambda_2^2 + \lambda_3^2}} \tag{1.5}$$

FA is scaled from 0 to 1 and is sensitive to the white matter microstructural disruption (Beaulieu, 2002). When the diffusion is isotropic, FA is equal to 0 and appears as dark or low signal intensity in the FA map. The higher FA indicates more anisotropic of the water diffusion in the pixel (e.g. corpus callosum show up as bright regions in the brain). The orientation of the longest axis of the estimated ellipsoid (primary eigenvector) can be converted to a color at each pixel. By combing the intensity of FA map, a color-encode orientation map can be created. Axial diffusivity (AD), is the primary eigenvalue (λ_1) of the tensor and is thought to describe the axonal integrity of the white matter structure. Radial diffusivity (RD), usually calculated as the average of the second and the third eigenvalues of the tensor and quantifies the magnitude of diffusion orthogonal to the principal diffusion direction, and believed to reflect the extent of white matter myelination (Song et al., 2005). In Figure 1.3, non-diffusion weighted image or b0 image and the averaged diffusion-weighted image (dwi) are also shown in the lower panel.

1.3.4 DTI-based tractography

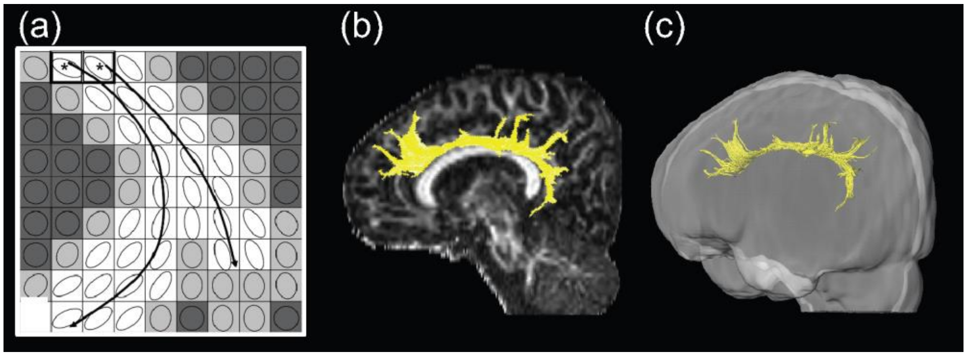

Figure 1.4: Three-dimensional fibers reconstruction. A schematic diagram shows a basic algorithm for fiber reconstruction (a) (Mori and Zhang, 2006) and sagittal view of actual reconstruction reconstructed fiber bundle of cingulum bundle at cingulate gyrus (CGC, shown in yellow) overlaid on FA map (b) and in a 3D transparent reconstructed brain (c).

In DTI-based tractography, we usually assume the orientation of the primary eigenvector or the diffusion tensor (or the largest axis of the ellipsoid, ν_1) to represent the local fiber orientation, which can be reconstructed into 3D streamlined fiber bundle based on the tensor field (Figure 1.4a) (Basser et al., 2000; Jones et al., 1999; Mori et al., 1999). The streamlined fibers initiate from seeds (pixel with asterisks in Figure 1.4a), and propagate based on the orientation of ν_1. In Figure 1.4, cingulum bundle at cingulate gyrus (CGC) white matter fibers were reconstructed with fiber assignment by continuous tracking (FACT) algorithm, also referred as deterministic tracking (Mori et al., 1999) and assigned arbitrary color for visualization overlaid on a FA map (sagittal view, Figure 1.4b) and in a transparent reconstructed brain (Figure 1.4c).

1.4 Perfusion magnetic resonance imaging (pMRI)

Perfusion in the human brain usually refers to the rate of blood flow through the capillary circulation of the brain tissue. It is typically reported in the units of blood flow per mass of tissue (e.g. ml/min/100g). Measurement of perfusion requires the use of tracer molecules or particles, such as H_2O^{15} in positron emission tomography (PET), xenon in x-ray computed tomography (CT) or magnetically-labeled blood water in arterial spin labeling (ASL) perfusion MRI.

1.4.1 Arterial Spin Labeling (ASL)

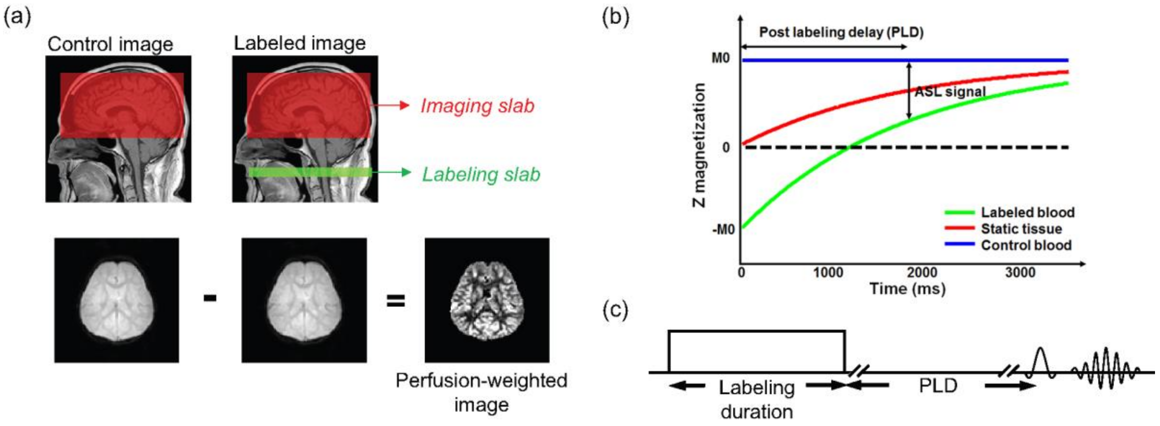

Figure 1.5: The principle in arterial spin labeling (ASL) measurements. Schematic description of a perfusion weighted image of human brain obtained by subtraction of the labeled images from the control images (a), T1 relaxation simulation of labeled blood (green), static tissue (red) and control blood (control blood) (b), schematic diagram of the pseudo-continuous ASL sequence (c).

ASL perfusion MRI allows noninvasive quantification of regional cerebral blood flow (CBF), using magnetically labeled blood water as an endogenous tracer (Detre et al., 2009). A schematic description of the ASL MRI is shown in Figure 1.5. There are two type of images acquired within the same region of interest (imaging slab shown in red in Figure 1.5a) in ASL acquisition: a labeled image in which the arterial blood water has been magnetically labeled or tagged using a radiofrequency pulse in the labeling slab shown in green in Figure 1.5a and a control image in which the arterial blood water hasn't been labeled. In the period of labeling duration, the arterial blood water has been magnetically inverted in the labeling slab, which makes the MRI signal from the inverted blood is negative relative to the signal from control blood (Figure 1.5b). After the labeling, we need to wait for some time, which is called post labeling delay (PLD, Figure 1.5b-1.5c) time, in order to make sure the labeled blood can travel from the labeling slab to the imaging slab and perfuse into the tissue in the imaging slab. Image acquisition will be started after the PLD time. Subtraction of a labeled image from a control image gives a measure of the amount of label which flowed into the tissue. This quantity is closely related to the tissue perfusion (Figure 1.5a). A typical change in image intensity between labeled and control is ~1%, so the signal to noise ratio (SNR) is lower than for a comparable proton density image and sensitivity to motion is great. If the experimental parameters are carefully controlled to fulfill several requirements: 1) the entire labeled bolus is delivered to the target tissue, which can be achieved by making PLD larger than arterial transit time; 2) when there is no outflow of labeled blood water; and 3) the relaxation of the labeled spins are governed by blood T1. When these are met, the perfusion can be quantified using an appropriate mathematic model (Alsop et al., 2015) in following equation:

$$CBF = \frac{6000 \times \lambda \times (SI_{control} - SI_{label}) \times e^{\frac{PLD}{T1_{blood}}}}{2 \times \alpha \times T1_{blood} \times SI_{PD} \times (1 - e^{\frac{-\tau}{T1_{blood}}})} \quad [ml/min/100g] \qquad (1.6)$$

where λ is the brain-blood partition coefficient in ml/g, α is the labeling efficiency, $SI_{control}$ and SI_{label} are the time-averaged signal intensities in the control and labeled images, SI_{PD} is the signal intensity from a proton density-weighted image, $T1_{blood}$ is the longitudinal relaxation time of arterial blood in seconds, τ is the labeling duration and PLD is the post labeling delay time.

1.5 Objectives of this research work

1.5.1 Reveal the cerebral blood flow (CBF) distribution and dynamic in the preterm brain

Birth at an age less than 37 gestational weeks, known as prematurity, is a common health problem across the world. An estimated 15 million babies are born preterm every year and this number continues to rise (Blencowe et al., 2012). It has been shown that premature birth has an influence on structural maturation manifested such as a decrease in cortical and deep gray matter volume, decreased myelination and gray/white matter differentiation (Huppi et al., 1998; Inder et al., 2005; Kapellou et al., 2006). Additionally, preterm infants are also at risk of developing neurological impairment (e.g. stroke; hypoxic-ischemic encephalopathy, HIE) (Varela et al., 2014; De Vis et al., 2013) and cardiovascular impairments (e.g. neonatal congenital heart disease, CHD) (Jain et al., 2014). Thus, to better understand the underlying mechanisms of adverse neurologic outcome, it is essential to understand normal brain development of the preterm brains.

CBF, which estimates the blood flow, hence, is a measure of glucose and oxygen supply to different brain regions for maintaining cellular and molecular process, is closely linked to regional neural activity and tightly coupled to brain metabolism (Raichle 1998). Revealing the CBF distribution and its dynamics in the healthy preterm brain might shed light on the evolution of several neurological pathologies (e.g. HIE, CHD, stroke) and may prove to be a novel prognostic masker. However, estimating the regional CBF measurement in the neonate population accurately is extremely challenging due to their low CBF. The purpose of the first project (Chapter 2) was to develop an arterial spin labeling (ASL) perfusion MRI protocol to obtain CBF measurements in preterm brain noninvasively and reproducibly by sequence optimization, and then explore the CBF distribution and developmental trajectory in the neonate brain from 32 to 45 postmenstrual weeks (PMW).

1.5.2 Investigate the atypical deep white matter (WM) development in children with autism spectrum disorder (ASD) age from 2 to 7 years

Autism spectrum disorder (ASD), is a neural developmental disorder in which the first behavioral symptom appear early in life (1-2 years of age) and can be clinical identified or diagnosed at 2 to 4 years of age (Courchesne et al., 2005). Literature has suggested there are age-specific neurological abnormalities in individuals with ASD, which is early brain overgrowth at the beginning of life and slowing or arrest of growth during the early childhood (Courchesne et al., 2001, 2003; Courchesne and Pierce, 2005). However, the white matter (WM) studies of ASD in young children are relatively rare, and the majority DTI studies to investigate deep WM microstructure in ASD have focused on the age range from mid-childhood and adolescence to adulthood (e.g. Barnea-Goraly, et al., 2005; Travers, et al., 2012) when the clinical manifestations have well emerged (Paus, et al., 2008). Moreover, these findings were not consistent: both strengthened WM integrity with increased FA (e.g. Ben Bashat, et al., 2007; Weinstein, et al., 2011; Wolff, et al., 2012) and reduced WM integrity with lower FA and higher RD (e.g. Sivaswamy, et al., 2010; Walker, et al., 2012) have been reported in various WM regions in children with ASD. Early years of life including 2-7 years mark an important period for the formation of neural wiring patterns (Casey, et al., 2005) and neural circuits (Tau and Peterson, 2010). This period is also critical for brain development and early intervention (Courchesne, et al., 2007; Sowell and Bookheimer, 2012). The goal of the second project (Chapter 3) is to comprehensively survey core WM microstructures with DTI-derived measurements (FA and RD) and delineate their trajectories in early developing brains between the ages of 2-7 years. This study may potentially address the inconsistent findings regarding deep WM integrity in ASD reported in prior dMRI studies.

1.5.3 Explore the short-range association fibers (SAF) in typically and atypically developing human brain

From early childhood to adulthood, the WM, including both deep WM and superficial WM regions, undergoes dramatic modifications including progressive increases of volume, myelination and changes in axonal diameter, in conjunction with brain network reconfiguration (e.g. Gong et al., 2008; Sepulcre et al., 2010). Unlike the well characterized deep WM or long-range association fibers (LAF) (e.g. Huang et al., 2006; Lebel et al., 2012; Wakana et al., 2004), little is known about the short-range association fibers (SAF) and superficial WM during brain development. Although dMRI-based tractography has been successfully used to trace the SAF in both human brain and macaque brain reproducibly (e.g. Oishi et al., 2008, 2011; Zhang et al., 2010), their function, number, trajectories and the role in network configuration in the typically developing (TD) human brain are not sufficiently defined. Moreover, the atypical development of SAF is thought to cause several mental disorders, such as ASD and schizophrenia (Paus et al., 2008; Courchesne and Pierce, 2005). For example, a pattern of short-rang over-connection and long-range under-connection in individual with ASD has been frequently hypothesized (e.g. Courchesne et al., 2007; Vissers et al., 2012; Wass, 2011). Both functional and structural long-distance connectivity appears to be weaker in ASD than in controls (e.g. Martino et al. 2014; Courchesne and Pierce, 2005). However, little is known about spatiotemporal characterization of “structural” short-distance connections in TD children or children with ASD. In the third project (Chapter 4), we developed a new index named normalized SAF (NSAF) based on DTI tractography to characterize the balance of SAF and LAF in the human brain. The goal is to study the developmental trajectories of SAF, and its role in the network reconfiguration of human brain under both TD and pathological conditions.

Chapter 2

Reveal the Spatiotemporal Cerebral Blood Flow (CBF) Dynamic in Preterm Human Brain from 32 to 45 Postmenstrual Weeks

2.1 Introduction

During the 3rd trimester, dramatic cellular and molecular processes, including cell proliferation, migration (Jacobson, 1991; Rabinowicz, 1986), synapse formation, dendritic arborization (Bystron et al., 2008; Huttenlocher, 1979) and myelination (Yakovlev and Lecours, 1967), take place in the cerebral cortex. Both glucose and oxygen, essential substrates for maintaining cellular and molecular processes during brain development, are delivered through cerebral blood flow (CBF). Rapid brain maturation requires both increases in whole brain CBF and localized increases as brain function begins to differentiate (see Silbereis et al., 2016 for review). Quantifying both global and regional CBF thus provide critical information about brain physiology and functional development. Furthermore, cortical microstructural architecture is also dramatically reshaped during 32-45 postmenstrual weeks (PMW) (Bystron et al., 2008; Kostovic and Jovanov-Milosevic, 2006; Rakic, 1972, 1995; Sidman and Rakic, 1973). However, how these regional microstructural changes relate to regional CBF changes has yet to be elucidated.

Arterial spin labeled (ASL) (Detre and Alsop, 1999) perfusion magnetic resonance imaging (MRI) provides a noninvasive approach for quantifying regional CBF without exposure to ionizing radiation or the administration of exogenous contrast agents, and hence is especially suitable for regional CBF measurements of infants and young children. ASL has become a reliable tool to study regional CBF in the brains of infants (e.g. Wang et al., 2008), children (e.g. Jain et al., 2012; Wang et al., 2003), adolescents (e.g. Satterthwaite et al., 2014) and adults (e.g. Chalela et al., 2000). ASL has also been applied to study regional CBF in neonate brains in normal (De Vis et al., 2013; Miranda et al., 2006) and pathological conditions (e.g. congenital heart disease, cardiac arrest or hypoxic-ischemic encephalopathy) (Licht et al., 2004; De Vis et al., 2015; De Vis et al., 2014; Massaro et al., 2013; Nagaraj et al., 2015; Pienaar et al., 2012; Varela et al., 2014; Wintermark et al., 2011). In these studies, regional CBF measures in both frontal and occipital cortex were significant higher in healthy neonates at 40-43PMW than those at 30-33PMW (De Vis et al., 2013). In contrast to research on regional CBF in relatively older children or adults, the major challenge unique in preterm brains is the extremely slow blood velocity (Wu et al., 2010). To date, there has been no standardized ASL protocol established for preterm brains, and optimization of ASL perfusion MRI protocol is needed. Moreover, successful measurement of the spatiotemporal dynamics of regional CBF during the critical developmental period of 32-45PMW would provide new insights into metabolic demand of underlying differentiated cellular activities. The associated brain microstructural changes can be inferred by the metric measurements with diffusion tensor imaging (DTI) (Basser et al., 1994). As an alternative to ASL, phase contrast (PC) MRI has been used to quantify global CBF (Bakker et al., 1999) of children and adolescents in a number of studies (e.g. Aslan et al., 2010; Jain et al., 2012). However, PC MRI slice locations have yet to be optimized to adapt to the complex anatomy of arteries at the neck region of preterm brains (Liu et al., 2014).

In this study, we explored the spatiotemporal dynamics of regional CBF during 32-45PMW using pseudo-continuous ASL (pCASL) (Alsop et al., 2015; Dai et al., 2008). We measured global CBF with PC MRI to reveal the extent of global CBF increase during the age of 33-42PMW. Using fractional anisotropy (FA) derived from DTI as a means of quantifying changes in regional cortical microstructure of the preterm brains (Ball et al., 2013; Yu et al., 2015), we also explored the relationship between regional CBF and cortical microstructure. A pCASL protocol was adjusted to be adapted to the slow cerebral blood velocity seen in preterm neonates, and pCASL, PC MRI and DTI were acquired from part (for pCASL and PC MRI) and the entire (for DTI) cohort of 89 preterm neonates, respectively. Without additional description, the age defined in postmenstrual week according to Engle's policy statement (Engle et al., 2004) was used.

2.2 Material and Methods

2.2.1 Participants

This study was approved by the local Institutional Review Board (IRB) of The University of Texas Southwestern Medical Center. 89 normal preterm infants were recruited from Parkland Memorial Hospital, Dallas, TX, USA, for research of normal prenatal and perinatal human brain development. These infants were selected through rigorous screening procedures by a board-certified neonatologist (LC). Exclusion criteria included the maternal drug or alcohol abuse during pregnancy; grade III-IV intraventricular hemorrhage; periventricular leukomalacia; hypoxic-ischemic encephalopathy; body or heart malformations; chromosomal abnormalities, lung disease or bronchopulmonary dysplasia; sepsis; necrotizing enterocolitis requiring intestinal resection or complex feeding/nutritional disorders; defects or anomalies of the forebrain, brainstem or cerebellum; brain tissue dysplasia or hypoplasia; abnormal meninges; alterations in the pial or ventricular surface; or white matter lesions. A pediatric radiologist (NR) with 25 years of experience confirmed no structural or signal abnormality with a dulcet image pattern appropriate for postmenstrual age after reading the MRI scans. Written and informed consent was obtained from the parents.

2.2.2 MRI sequence optimization and data acquisition

All MRI scans were performed on the preterm and term neonates after their births with a 3T Philips Achieva System. The neonates were fed before the MRI scan and wrapped with a vacuum immobilizer to minimize motion. No sedation was used for all MR data acquisition. All 89 preterm infants underwent the diffusion MRI and structural MRI. The pCASL and PC MRI sequences were applied to a sub-cohort of preterm infants. As there is no standard neonate pCASL sequence as a reference, both 3D gradient spin-echo (GRASE) and 2D multi-slice echo-planar imaging (EPI) were adjusted from adult human protocol to achieve good image quality and used as the readout component of pCASL sequence. Sequence parameters are described in detail in subsequent sections. A total of 16 preterm infants underwent ASL with a 3D GRASE pCASL sequence adjusted to be adapted to neonate brains. Of these, 12 datasets (age at scan: 33.3-41.1weeks, 36.6±2.6weeks; age at birth: 27.7-39.3weeks, 31.9±3.1weeks; 7 Male/5 Female) were retained and 4 datasets affected by severe motion were removed. Another 18 preterm infants underwent ASL with 2D multi-slice pCASL sequence, also adjusted to be adapted to neonate brains. Of these, 10 datasets (age at scan: 32.7-45.1weeks, 37.7±3.8weeks; age at birth: 30.0-41.4weeks, 34.9±3.8weeks; 9 Male/1 Female) were kept for further analysis and 8 datasets affected by severe motion were removed. 19 preterm infants underwent global CBF quantification with a PC sequence. Of these, 14 datasets (age at scan: 33.3-41.6weeks, 36.4±2.2weeks; age at birth: 27.7-41.3weeks, 32.6±3.9weeks; 6 Male/8 Female) were kept for further analysis and 5 datasets affected by severe motion were removed.

2.2.2.1 PC MRI for global CBF measurement

MR images from a representative preterm infant at 35PMW were used to demonstrate the PC MR acquisition (Figure 2.1). A time-of-flight angiogram was acquired with axial slices encompassing a slab covering the foramen magnum (see mid-sagittal image on left panel of Figure 2.1). The imaging parameters of the angiogram were: TR/TE/flip angle = 20ms/3.45ms/18^o; field of view (FOV) = 100×100 mm^2, in-plane imaging resolution = 1×1 mm^2, 20 slices acquired with slice thickness = 1mm, thickness of saturation slab above the imaging slab = 60mm, and the scan duration = 19s. The four feeding arteries, including bilateral internal carotid artery (ICA) and vertebral artery (VA), could be well visualized in the generated angiogram on the right middle panel of Figure 2.1. Based on the angiogram, the slices for the PC MRI of ICAs were placed at the level of the foramen magnum and the slices for the PC MRI of VAs were placed between the two turns in V3 segments (at approximately the level of the C1 vertebral column), shown in the right panel of Figure 2.1. Image parameters of PC MRI were: FOV=120×120 mm^2, in-plane imaging resolution =0.5×0.5 mm^2, single slice with a thickness of 3 mm, maximum velocity encoding =10 cm/s, non-gated, 4 repetitions, and scan duration of each artery =24s. As shown in Figure 2.1, the cross-section of the target artery with higher intensity can be appreciated in each PC image.

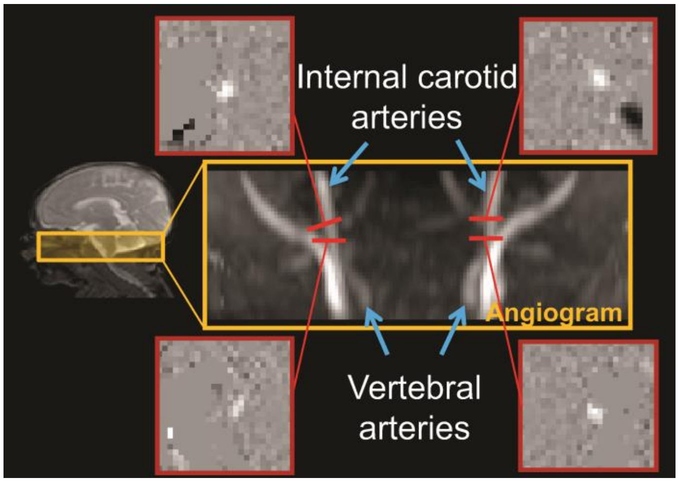

Figure 2.1: Phase-contrast (PC) MRI for global cerebral blood flow (CBF) measurement. The coronal view of the angiogram in the right middle panel shows the feeding arterials, namely internal carotid and vertebral arteries, with anatomical location of the 3D angiography delineated in a T2 weighted sagittal image on the left panel. The four slices of the PC MRI scans were positioned perpendicular to the respective feeding arteries on the angiogram, shown as red bars. The four phase images of the target arteries from the PC MRI scans are shown on the four panels surrounding the angiogram.

2.2.2.2 3D GRASE pCASL and 2D multi-slice pCASL for regional CBF measurement

PCASL labeling (Dai et al., 2008) combined with either 3D GRASE or multi-slice EPI as readout component was used to measure regional CBF. In the first several neonates (data not included in the Results due to non-optimized results before finalized adjustment), the position of labeling slab and post labeling delay (PLD) time were tested on multiple possible values to adapt to slow blood flow velocity of the preterm neonates. The middle of labeling slab was placed between the bottom of the pons and the bottom of the cerebellum as an optimized position of labeling slab (Figure 2.2a). The bottom of the pons was selected as the optimized labeling location, based on clearer gray-white matter contrast and fewer artifacts in the CBF map (shown in the panel of Figure 2.2a with green contour). These adjusted protocols were thereby used in the rest of the study. PLD durations of 1525ms, 1900ms, 2000ms, 2300ms and 2500ms were tested in a few neonates (data not included in the Results due to non-optimized results before finalized adjustment). Extremely slow blood velocity in preterm brain and subsequently longer time for labeled blood to perfuse into the brain tissue in the imaging slab require a longer PLD. Since the ASL signal undergoes T1 decay after labeling, the trade-off of using a longer PLD time is a decrease of the signal and noise ratio (SNR) in labeled images. As shown in the panel with green contour in Figure 2.2b, the longest PLD duration of 2500ms, yielded less artifacts and optimal gray-white matter contrast in the CBF map, was selected for the rest of the study. In addition, two background suppression (BS) pulses were added between labeling and readout component in the 3D GRASE pCASL sequence to suppress the static tissue signal (gray/white matter) and increase the SNR of ASL signal (Ye et al., 2002). After T_1 relaxation simulation of gray/white matter and control/ labeled blood, we found that it is optimal to put BS1 at 2350 ms and BS2 at 3734 ms in the pulse sequence with most gray/white matter tissue signal intensity suppressed (Figure 2.2c). The finalized imaging parameters of 3D GRASE pCASL and 2D multi-slice pCASL sequences for preterm brains are listed in Table 2.1.

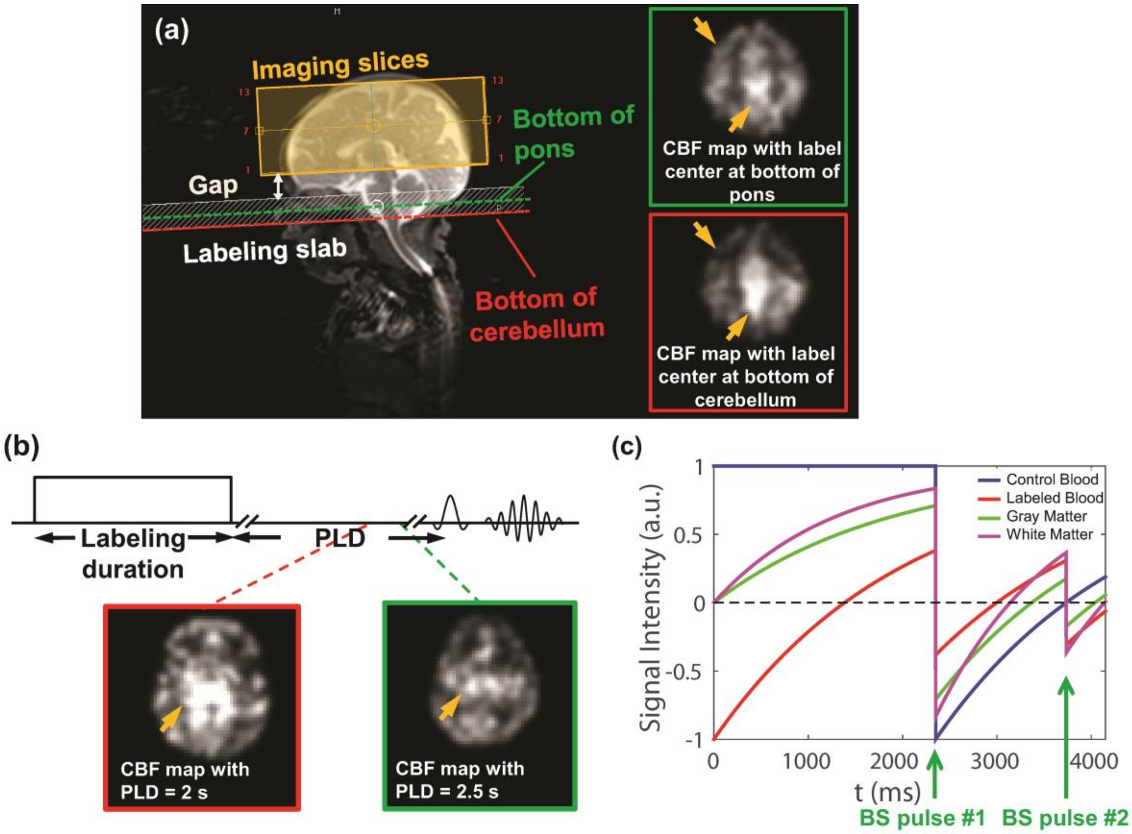

Figure 2.2: Adjustments of major pCASL sequence parameters for preterm brains. (a) Selection of positioning of labeling slab for 3D GRASE and 2D multi-slice pCASL: Imaging slices (yellow shaded box) and labeling slab (white shaded box) were positioned to be parallel to the anterior commissure-posterior commissure (AC-PC) line. The middle of labeling slab was chosen to be located at the bottom of the pons (green dashed line) instead of bottom of cerebellum (red dashed line) in preterm brain. (b) Selection of post labeling delay (PLD) time for 3D GRASE and 2D multi-slice pCASL: PLD was chosen to be 2.5s instead of 2s. The yellow arrows in CBF maps (a, b) point to the regions with less artifacts using the optimized sequence (highlighted with green contour). (c) Optimization of the timing of background suppression (BS) pulses for 3D GRASE pCASL using T1 relaxation simulation. Optimal sequence parameters for 3D GRASE and 2D multi-slice pCASL are listed in Table 2.1. Of the note, the two CBF maps in (b) were from two different subjects.

2.2.2.3 Diffusion MRI acquisition

DTI was acquired on all 89 preterm infants with a single-shot, EPI sequence with Sensitivity Encoding parallel imaging scheme (SENSE, reduction factor = 2). The DTI imaging in-plane resolution was 1.5×1.5 mm^2 with a FOV of 168×168 mm^2. Axial slices of 1.6 mm thickness without gap were acquired parallel to the anterior-posterior commissure (AC-PC) line. A total of 60 slices covered the entire brain. The diffusion weighting was encoded with 30 independent directions (Jones et al., 1999) and the b-value was 1000 s/mm^2.

Table 2.1: Finalized imaging parameters for the 3D GRASE and multi-slice pCASL

Parameter	**3D GRASE pCASL**	**Multi-slice pCASL**
Scan Mode	3D	MS
Fast Imaging Mode	GRASE	EPI
Field of view (mm^2)	140×140	160×160
Matrix	40×40	46×46
Number of slice	13	16
Acquisition resolution (mm^3)	3.5×3.5×4	3.5×3.5×3.5
TR/TE (msec)	4462/18	4380/7.4
Label duration (msec)	1650	1650
Post label delay (msec)	2500	2500
Label slab thickness (mm)	16	16
Label offset (mm)	42	36
Background suppression time 1 (msec)	2350	--
Background suppression time 2 (msec)	3734	--
Middle of Labeling slab location	bottom of Pons	bottom of Pons
Dynamic scan	30	40
SENSE factor	2	2.5
Scan Time	~5 min	~6 min

2.2.2.4 T2-weighted image

T2-weighted image was acquired on all 87 preterm infants with following parameters: turbo spin echo sequence, TR/TE = 3000/135ms, 65 slices, voxel size = 1.5×1.5 ×1.6 mm^3, FOV = 160×160×104 mm^3. T2-weighted images have superior gray and white matter contrast for preterm brains and were used for anatomical guidance and brain volume calculation.

2.2.3 MRI postprocessing

2.2.3.1 Global CBF measurement

PC MRI provides a quantitative measurement of the blood flow velocity, v, in the ICAs and VAs. The blood velocity can be converted to flow rate by integrating over the cross-section of the vessels with equation $F = \int v \, dA$ (2.1), where F is blood flow with the unit ml/sec and A is the cross-sectional area of the blood vessel with the unit mm^2. The brain volume was measured from the T2-weighted image as parenchyma volume (gray matter + white matter volume). The global CBF was calculated with the equation: *global CBF=F/ (ρ*brain volume)* (2.2). The brain tissue density *ρ* was assumed as 1.06 g/mL in Eq (2.2) (Dittmer, 1961; Herscovitch and Raichle, 1985).

2.2.3.2 Regional CBF measurement

In ASL MRI, CBF can be derived from the difference between "label" images in which arterial blood has been magnetically-labeled and "control" image in which the arterial blood has not been labeled. Specifically, regional CBF value can be estimated from pCASL data using the basic model described in ASL white paper (Alsop et al., 2015):

$$f_{pCASL}(x,y,z) = \frac{6000 * \lambda \cdot \Delta M(x,y,z) * e^{\frac{PLD(z)}{T_{1a}}}}{2\alpha \cdot M_b^0 \cdot T_{1a} \cdot \left(1 - e^{\frac{-LabelDur}{T_{1a}}}\right)} \qquad [ml/100g/min] \qquad (2.3)$$

where $f_{pCASL}(x,y,z)$ is the blood flow at voxel (x,y,z) obtained from pCASL in milliliters of blood per minute per 100g brain tissue. $\Delta M(x,y,z)$ is the difference between dynamic-averaged signal intensity in control image and that in the label image at voxel (x, y, z). Here α, the labeling efficiency, is 0.92 according to the relationship of labeling efficiency and blood velocity in the previous study (Aslan et al., 2010) with the blood velocity of 10.77 ± 4.44 cm/sec measured from PC MRI of 14 neonates; λ , the blood-brain partition coefficient, is 0.9 mL/g (Herscovitch and Raichle, 1985); *PLD(z)*, the post labeling delay time at the slice *z*, is 2500ms for images acquired with 3D GRASE pCASL sequence and *2500+(z-1)*w* for images acquired with multi-slice pCASL sequence, where *w = 35ms* is the slice timing delay between adjacent slices; *LabelDur*, the labeling duration, is 1650ms; T_{1a}, T_1 of arterial blood, was obtained for each subject based on blood T1-hematocrit curve (Liu et al., 2015). The subject-specific hematocrit was estimated with the subjects' age at scan based on the hematocrit-age curve (Jopling et al., 2009). To scale the signal intensities of the subtracted ASL images to absolute CBF units, the value of equilibrium magnetization of brain tissue (M_b^0) is needed. This value was obtained with equation (2.4.1) for 3D GRASE pCASL and equation (2.4.2) for multi-slice pCASL:

$$M_b^0 = {M_{thalamus\_slice}} \Big/ \left(1 - 2 \cdot e^{\frac{-(PLD+LabelDur-BS2)}{T_{1tissue}}} + 2 \cdot e^{\frac{-(PLD+LableDur-BS1)}{T_{1tissue}}} - e^{\frac{-(PLD+LableDur)}{T_{1tissue}}}\right) \tag{2.4.1}$$

$$M_b^0 = {M_{thalamus\_slice}} \Big/ \left(1 - e^{\frac{-TR}{T_{1tissue}}}\right) \tag{2.4.2}$$

where $T_{1tissue}$, the *T₁* of brain tissue, is 2500 ms (Conklin et al., 2008; Lu et al., 2004; Williams et al., 2005); the timings of two BS pulses, *BS1* and *BS2*, are 2350 ms and 3734 ms, respectively; $M_{thalamus\_slice}$ is the average signal intensity in the region of interest (ROI) including entire brain on a slice containing thalamus in the control image. To improve the accuracy of regional CBF estimation from 3D GRASE pCASL scan, either a short auxiliary scan (to correct for M_b^0 estimation) or PC MRI can be acquired to scale the absolute CBF calculated from Eq (2.3). The estimation of M_b^0 from an auxiliary scan using identical readout module as 3D GRASE pCASL but without labeling or background suppression components was more accurate than the estimation of M_b^0 directly from the main 3D GRASE pCASL scan using Eq (2.4.1) (Alsop et al., 2015). PC MRI could not be used to normalize the regional CBF because the 3D pCASL scan did not cover the whole brain in this study. Instead, an auxiliary scan was performed to estimate $M_{bauxscan}^0$ using Eq (2.4.2). 4 preterm infants underwent this auxiliary scan successfully, while other infants' auxiliary scans were either not useful due to severe motion or not conducted due to limited scan time. An averaged scaling factor was obtained with these 4 preterm infants' auxiliary scans to correct for all CBF maps from 3D GRASE pCASL acquisition. We calculated an averaged scaling factor (SF) based on auxiliary scans of these 4 preterm infants to correct the absolute CBF using Eq. (2.5) below:

$$f_{pCASL}(x,y,z)_{corrected} = avg(SF) * f_{pCASL}(x,y,z) \tag{2.5}$$

where *avg(SF)*, averaged SF, was 2.61; $f_{pCASL}(x,y,z)$ was calculated from Eq (2.3) in the main text. *avg(SF)* was averaged from SF obtained from auxiliary scan of 4 preterm infants. SF of auxiliary scan of individual infants can be obtained using equation (2.6) below:

$$SF = \frac{SS_{auxscan}}{SS_{pCASL}} * \frac{M^0_{b_{pCASL}}}{M^0_{b_{auxscan}}} \tag{2.6}$$

where $SS_{auxscan}$ and SS_{pCASL}, the scale slope for auxiliary scan and 3D pCASL scan, were obtained from PAR file of Philips raw data, respectively; $M^0_{b_{auxscan}}$ and $M^0_{b_{pCASL}}$ were M^0_b estimated from auxiliary scan and 3D pCASL scan, respectively.

2.2.3.3 Measurement of frontal and occipital CBF with ROI

ROIs were drawn manually in the frontal and occipital cortical regions in both hemispheres of the CBF maps. They were drawn in the same axial slice at consistent anatomical location across subjects. Each ROI included 10 contiguous cortical voxels in each hemisphere. As an example, delineation of the frontal and occipital ROI on CBF maps of a 34.6PMW and a 37.4PMW brain are displayed in Figure 2.3. Averaged CBF in frontal or occipital ROIs were calculated from ROIs drawn on both hemispheres for each subject.

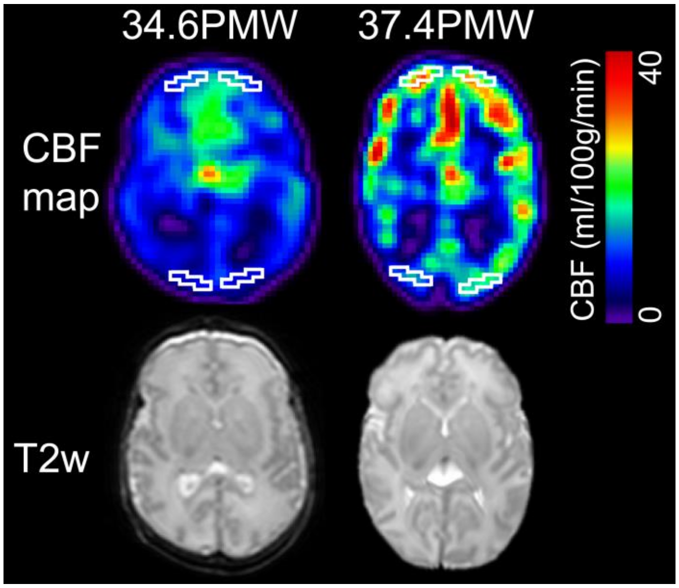

Figure 2.3: Heterogeneous frontal and occipital CBF with regions of interest (ROIs), contoured with white lines, were placed in frontal and occipital areas. Axial CBF maps from a representative preterm brain with younger age (34.6PMW) and a preterm brain with older age (37.4PMW) are displayed in color on left and right panel of the figure, respectively, with color bar encoding the CBF values. Corresponding T2 weighted images are displayed in the bottom for anatomical guidance.

2.2.3.4 Measurement of cortical skeletonized FA with DTI

Automated image registration (AIR) (Woods et al., 1998) was applied to raw diffusion weighted images to correct distortion caused by eddy current. The standard tensor fitting was conducted with DTIStudio (Jiang et al., 2006) to generate the FA map. To minimize partial volume effects, cortical skeletonized FA values (Yu et al., 2015) were used to explore the relationship between regional CBF and FA in the cortex. Cortical skeletons were obtained with the skeletonization function of TBSS in FSL (http://fsl.fmrib.ox.ac.uk/fsl/fslwiki/TBSS) based on averaged cortical FA maps for preterm brains at 33 and 36 PMW or averaged gray matter segmentation maps for neonate brains at 39PMW (Yu et al., 2015). Cortical skeleton of individual preterm brain was obtained by inverse registration from averaged templates at 33, 36 or 39 PMW. The template having the PMW closest to the PMW of the individual preterm brain was used for inverse registration. Note that high FA was observed not only at the WM but also cortical plate for preterm brain FA at 33 and 36 PMW (Yu et al., 2015).

2.2.4 Statistical analysis

2.2.4.1 Reproducibility analysis

3 randomly chosen subjects were scanned twice with separate but identical finalized 3D GRASE pCASL sequence in the same session for reproducibility analysis. Intraclass correlation coefficient (ICC) (Jain et al., 2012; Shrout and Fleiss, 1979) was calculated to assess the reproducibility of CBF maps obtained from two repetitions of ASL scans.

2.2.4.2 Correlation between the global CBF and age

Linear regression between the global CBF measurement and the postmenstrual age at the scan time was performed to evaluate the age dependent global CBF changes during 33-42PMW. To remove the effects of postnatal age (i.e. the chronological age defined in Engle et al., 2004), partial correlation between global CBF and postmenstrual age was conducted with the postnatal age added as a regressor using R software.

2.2.4.3 Paired t-test between frontal and occipital CBF

To test if the CBF distribution is heterogeneous among different brain regions, paired t-test between CBF measurements averaged from frontal ROI voxels and those averaged from occipital ROI voxels was conducted. The frontal and occipital CBF measurements were paired according to the individual subject.

2.2.4.4 Correlation between frontal or occipital CBF and age

Linear regression was conducted between mean CBF in frontal or occipital ROI from both 3D GRASE and 2D multi-slice pCASL acquisitions and the postmenstrual age at the time of scan. To consider the postnatal age effects, postnatal age was added as a regressor in the correlation between CBF and the scan age. In addition, comparison between the slopes of age-dependent linear trend lines of frontal CBF and occipital CBF was conducted with a mixed-effects model as follows:

$$CBF_i = \mu + \beta_1 * I_i + \beta_2 * age_i + \beta_3 * (I \cdot age)_i + \epsilon_i \qquad (2.7)$$

where *CBF$_i$* was CBF frontal or occipital CBF measurement from the *ith* participated neonates; μ was the overall mean of CBF measurement, I_i was the indicator variable with $I_i = 1$ for frontal CBF measurement and $I_i = 0$ for occipital CBF measurement; age_irepresented the age of *ith* neonate; $(I \cdot age)_i$was the age-region interaction term and ϵ_i was the error term; β_1, β_2 and $\beta_3$represented the parameters to be estimated for I_i, age_i and $(I \cdot age)_i$, respectively. The statistical procedures were performed using R software (https://www.r-project.org/).

2.2.4.5 Correlation between cortical CBF and cortical skeletonized FA measurement

Linear regression between averaged regional CBF and averaged cortical skeletonized FA values in the same frontal ROIs as those shown in Figure 2.3 was conducted. Since both CBF-age and FA-age (e.g. Huang et al., 2013; Yu et al., 2015) correlations could be significant, it is possible the correlation between CBF and FA is due to age. To remove the age effect, partial correlation between cortical FA and cortical CBF in the frontal ROIs was conducted using R software.

2.3 Results

2.3.1 Age-dependent increase of global CBF for preterm infants

Figure 2.4 shows the age-dependent increase of global CBF derived from PC MRI of 14 infants aged 33 to 42PMW. Global CBF increases significantly (r=0.65, p=0.01) with postmenstrual age. Specifically, the global CBF increases from 8.4 ml/100g/min at 33PMW to 21.6 ml/100g/min at 42PMW with an increase rate of 1.22 ml/100g/min per PMW. Note that the value of global CBF at 42PWM almost doubles the value of global CBF at 33PMW. After removing the effects of postnatal age, global CBF still shows significant age-dependent increase (r=0.62, p=0.02).

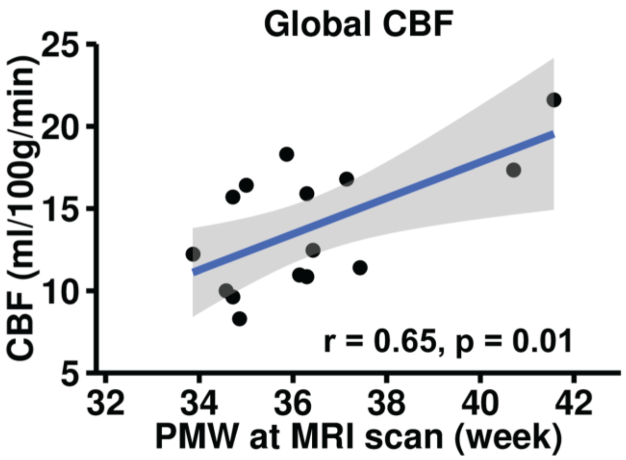

Figure 2.4: Global CBF measurements from PC MRI increase significantly (p<0.01) and dramatically with age in preterm brains of 33-42PMW. Each black circle represents global CBF measurement from a preterm infant.

2.3.2 Heterogeneous regional CBF distributions in the individual preterm brains

Paired t-test shows that CBF measurements at frontal regions are significantly higher (p<0.001) than those at occipital regions for preterm brains during 32-45PMW. This heterogeneity can also be appreciated in CBF maps of two randomly selected preterm brains at 34.6PMW and 37.4PMW shown in Figure 2.3. With incomplete ASL coverage of the brain, summation of ASL CBF across all measured voxels is less than the PC MRI CBF multiplied by the entire brain volume, partly reconciling the measurements from the two MR pulse sequences.

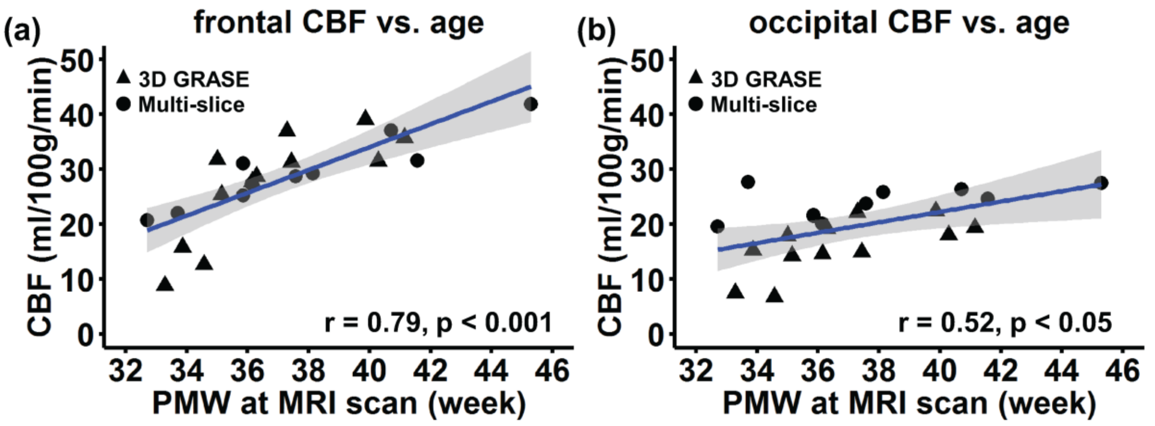

Figure 2.5: Regionally heterogeneous increases of CBF measurements in developing preterm brains revealed by combined datasets from 3D GRASE and 2D multi-slice pCASL acquisitions. Regional CBF measurements increase significantly with age in both frontal (a) and occipital (b) cortex. Relatively higher frontal CBF increase rate can be appreciated. Each data point (black triangle or black circle) in (a, b) represents regional CBF of one preterm infant, with black triangle and black circle indicating regional CBF measurement with 3D GRASE pCASL and multi-slice pCASL, respectively.

2.3.3 Heterogeneous regional CBF increase during 32-45PMW

Age-dependent frontal and occipital CBF trend lines are shown in Figure 2.5a and Figure 2.5b, respectively. Both frontal and occipital CBF values increase significantly with age ($r = 0.79$ and $p < 0.001$ for frontal CBF; and $r=0.52$, $p<0.05$ for occipital CBF). In addition, a significantly faster CBF increase ($p = 0.027$) can be appreciated at the frontal regions with the increase rate of 2.08 ml/100g/min per PMW (Figure 2.5a), which is approximately double of the CBF increase rate of 0.94 ml/100g/min per PMW at the occipital regions (Figure 2.5b). The increase rates were obtained based on fitted linear trend lines of frontal and occipital CBF during 32-45PMW. After regression of postnatal age, significantly age-dependent increases of regional CBF were still found in both frontal ($r=0.75$ and $p=0.001$) and occipital cortex ($r=0.56$ and $p=0.008$). The CBF measurements from two datasets were combined in Figure 2.5 to increase statistical power, after confirming there was no significant difference in regional CBF (frontal or occipital) increase rate measured by background-suppressed 3D GRASE pCASL versus multi-slice pCASL (p=0.057 for frontal region; p=0.077 for occipital region).

2.3.4 Relationship between cortical CBF and cortical FA in the frontal region

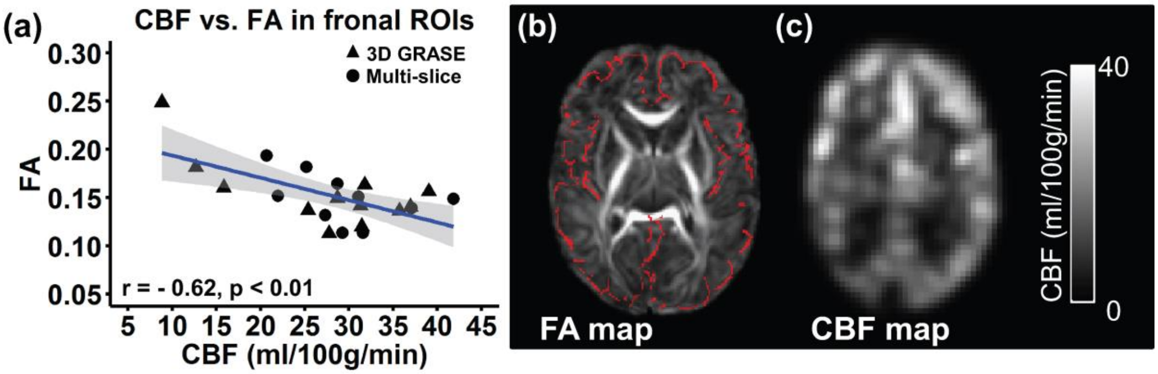

Figure 2.6: Correlation between cortical fractional anisotropy (FA) and CBF in the same corresponding frontal region. (a) Regional CBF is significantly (p<0.01) correlated with cortical FA ; (b) FA map with cortical skeleton shown in red from a representative preterm infant at 37.4PMW; (c) corresponding CBF map from the same preterm infant. Each data point in (a) represents cortical FA and CBF measurement from one neonate, with black triangle and black circle indicating regional CBF measurement with 3D GRASE pCASL and multi-slice pCASL, respectively.

A significant negative correlation (r=-0.62, p<0.01) was observed between cortical CBF and cortical FA in frontal regions of preterm infants aged 32-45PMW, as demonstrated in Figure 2.6a. After removing the age effect, significant negative partial correlation (r=-0.44, p<0.05) was still obtained between cortical CBF and cortical FA in frontal regions. Higher regional CBF is associated with lower cortical FA at the frontal region. Representative cortical FA and CBF maps acquired at 37.4PMW are shown in Figure 2.6b and 2.6c, respectively. As indicated in Figure 2.6b, FA values extracted from a cortical skeleton were used to minimize partial volume effects for cortical FA measurements.

2.3.5 Reproducibility of the CBF measurement

Figure 2.7 shows CBF maps from two repetitions of pCASL scans of 3 randomly chosen preterm infants. The ‘rep1’ and ‘rep2’ present the CBF maps of each preterm infant consecutively scanned with the same pCASL sequence in one session. The ICC values for three preterm infants were 0.75, 0.85 and 0.91 respectively, indicating moderate-to-strong reproducibility (ICC from 0.75 to 0.95).

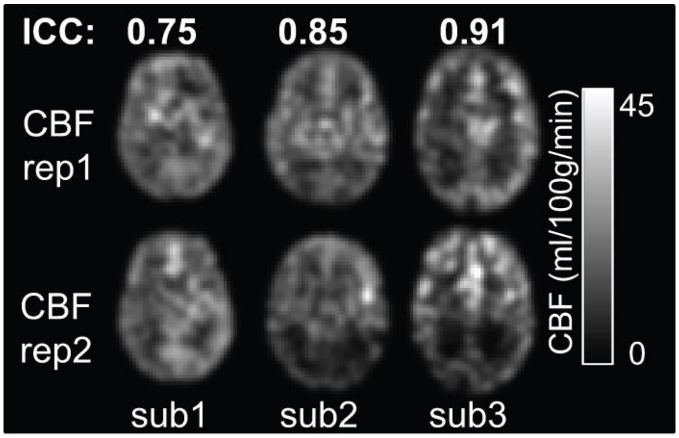

Figure 2.7: Test-retest reliability of the measured CBF maps from three randomly selected preterm infants with optimized 3D GRASE pCASL sequence. Same slices of CBF maps from two repetitions of scans are shown as ‘rep1’ and ‘rep2’. The calculated intraclass correlation coefficients (ICC) are shown on the top of CBF maps. Color bar encodes the CBF values.

2.4 Discussion

Heterogeneous increases of regional cortical CBF were demonstrated using pCASL data of preterm brains in the age range of 32-45 PMW. Frontal CBF increases faster than occipital CBF (Figure 2.5). In parallel to regionally heterogeneous CBF increases, global CBF increases were also demonstrated using PC MRI during this period. Specifically, the measured global CBF value at 42PMW almost doubles the global CBF value at 33PMW (Figure 2.4), suggesting dramatic increase of whole brain metabolic needs during the 3rd trimester. A strong negative correlation between the frontal CBF and frontal cortical FA measurements (Figure 2.6) was also found, suggesting that increasing dendritic arborization reflected by smaller cortical FA is associated with higher amount of regional cortical CBF. Imaging parameters of pCASL sequences were selected to adapt to extremely slow blood velocity of the preterm brains and these sequences had achieved moderate-to-strong reproducibility for regional CBF measurements (Figure 2.7). Relatively comprehensive scan ages of preterm brains ranged from 32 to 45PMW, covering majority of the 3rd trimester. Significant age-dependent increases of both global and regional CBF (after removing the postnatal age effects) during this critical developmental period were revealed for both understanding early brain development and meeting the need for health care of preterm infants.

2.4.1 Significant global CBF increases during preterm brain development

Dramatic and rapid brain development takes place in the 3rd trimester. In such a short period, the cerebral cortex volume increases 4-fold (Huppi et al., 1998; Limperopoulos et al., 2005). Inside the cerebral cortex, cellular and molecular processes including dendritic arborization, synaptic formation, and cell differentiation (Innocenti and Price, 2005; Marín-Padilla, 1992; Rakic, 1988; Sidman and Rakic, 1982) reshape the brain configuration. The scan age of preterm brains in this study, namely 33-42PMW, covers the majority of the 3rd trimester. Despite the difference of intrauterine and extrauterine brain growth (discussed in details in “4.4 Considerations and future perspectives” section below), the observed CBF measurements obtained from preterm brains over 33-42PMW reflect increase of cerebral energy consumption (du Plessis, 2009) associated with cellular processes in the cortical development.

Global CBF measurements obtained around 33-42PMW have previously been reported using various imaging modalities. Global CBF in preterm neonates (mean age at 40PMW) was reported to be 4.9 to 23 ml/100g/min (Altman et al., 1988) using positron emission tomography (PET). With near infrared spectroscopy (NIRS), global CBF was found to range from 7 to 33 ml/100g/min in preterm infants age 26-44PMW (Edwards et al., 1988). Another NIRS study showed that global CBF ranged from 6.3 to 15.2 ml/100g/min in very preterm infants aged 24 to 31PMW (Meek et al., 1998). Using xenon clearance, global CBF was reported to be 4.3-18.9 ml/100g/min in preterm infants less than 33PMW (Greisen and Trojaborg, 1987). Global CBF values obtained in the present study using PC MRI ranged from 8.4 to 21.6 ml/100g/min during 33-42PMW (Figure 2.4), and are consistent with the previous findings.

2.4.2 Heterogeneous regional CBF distributions and increases in preterm brains

Although global CBF increases from 32-45 PMW, CBF changes are also regionally heterogeneous, with significantly different CBF increase rates in frontal and occipital cortices (Figure 2.5). Accordingly, higher frontal CBF increase rates enlarged CBF differences between frontal and occipital regions. Regional differences in CBF during development have also been reported using modalities other than MRI. Using xenon clearance, occipital CBFs have been found significantly lower than frontal and parietal CBF in preterm infants with less than 34 gestational weeks and scanned between 0-240 hours after birth (Baenziger et al., 1995). Similar results were reported in preterm infants aged 26-34PMW with blood flow significantly higher in mesial frontal cortex than that in mesial occipital cortex using single photon emission computed tomography (SPECT) (Borch and Greisen, 1998). Regional heterogeneity in the rates of metabolic maturation for different cerebral cortical regions have also been observed in infants. The PET studies revealed different age-dependent curves of glucose utilization among different brain regions, including primary visual cortex (in occipital cortical region) and middle frontal gyrus, in infants of 0 to 18 months (Chugani and Phelps, 1986). Steeper frontal CBF changes (Figure 2.6) in this study is consistent to steeper frontal cortical FA decrease, implying more intense dendritic formation, compared to cortical FA decrease in occipital or other primary sensorimotor regions observed consistently across different groups in the preterm brains (deIpolyi et al., 2005; Ball et al., 2013; Yu et al., 2015). However, it is widely known that in other developmental periods (e.g. 0-4 years in PET studies in Chuangi and Phelps, 1986; Chuangi, 1998) higher-order cognitive functions related to the frontal regions emerge later than primary functions such as sensorimotor and visual functions. Different developmental pattern of frontal region relative to occipital region in this study may be due to different brain developmental period from that in the previous studies (e.g. Chuangi and Phelps, 1986; Chuangi, 1998). Synaptic density measurements (Casey et al., 2005; Huttenlocher and Dabholkar, 1997) suggested synaptic density increases faster in prefrontal cortex than in visual cortex (occipital cortical region) during the age range in the present study, while prolonged slower prefrontal maturation was observed from 2 months after birth to adolescence (Huttenlocher and Dabholkar, 1997). The observed higher CBF increase rate in the frontal cortex than occipital cortex may not suggest the emergence of higher-order cognitive function in this early developmental stage, namely 32-45PMW. Instead, it may suggest that neuronal processes such as dendritic arborization and synaptic formation, forming the basis for later emergence of the higher-order functions, is more active at frontal cortex in 32-45PMW while such active neuronal processes at other cortices may be almost finished by 32PMW (e.g. Yu et al., 2015). The exact mechanism underlying different frontal change patterns in different developmental periods is unknown, warranting further studies with a consistent metric measurement in various developmental stages including before and after normal time of birth. That all neonates were scanned during their natural sleep with their eyes closed and no visual stimuli may also contribute to the consistently low CBF at occipital cortex.

Compared to regional CBF estimates from pCASL, the global CBF from PC MRI is considered as a more robust CBF measurement. PC MRI yields blood velocity measurements in the major feeder and therefor provides global CBF even for low flow velocities (Liu, et al., 2014; Jain, et al., 2014; Varela et al., 2011). PC MRI has been well validated by ultrasound and used for quantitative flow measurements for more than 2 decades (Evans et al., 1993). On the other hand, PC MRI offers for the entire brain only a single global CBF value which is averaged CBF in the whole brain tissue. Hence, global CBF is much less informative compared to regional CBF measurements (one CBF value per brain voxel) offered by pCASL.

2.4.3 Relationship between cortical CBF and cortical FA in the frontal region

Cortical microstructure is altered by regionally distinctive and rapid cellular and molecular processes during 32-45PMW. With whole brain cortical FA mapping, inhomogeneous regional microstructural changes reflected by cortical FA were found in mid-fetal (Huang et al., 2013) and late-fetal (Ball et al., 2013; Yu et al., 2015) human brain development. The predominantly radially organized structures, radial glial scaffolds (Rakic 1972, 1995; Sidman and Rakic 1973), in the immature cortical plate are associated with high FA. In the cortical plate, migrating neurons (along radial glial scaffold) interact with each other or with existing neurons of the cortical plate through synaptic formation, dendritic arborization and axonal growth (e.g. Sidman and Rakic 1973; Kostovic and Jovanov-Milosevic 2006; Bystron et al., 2008) and disrupt the radially organized structures, causing decreases of cortical FA (McKinstry et al., 2002). Accordingly, the immature cortical plate with less synapses in it may have less metabolic demand. Regionally heterogeneous synaptic formation after regionally differentiated processes such as dendritic arborization may raise metabolic demand. For example, previous PET studies (Chugani and Phelps, 1986) suggested the local cerebral metabolic rate for glucose (LCMRglc) in cerebral cortex may provide an indirect measure of synaptogenesis in the brain. By correlating frontal cortical FA (quantifying cortical microstructure) to corresponding frontal CBF (inferring metabolic need) across the age of 32-45PMW, Figure 2.6 demonstrated that higher CBF is associated with lower FA. It suggested that synaptic formation and cellular differentiation indicated by FA decrease might be associated with the elevated local CBF during preterm brain development.

2.5 Considerations and future perspectives

Due to relatively small sample size of preterm subjects undergoing scan with 3D GRASE pCASL or 2D multi-slice pCASL, we combined datasets acquired with both protocols to study age-dependent regional CBF changes. To integrate two datasets, we corrected absolute CBF measurement from 3D GRASE pCASL by multiplying a scaling factor. Unlike 2D multi-slice pCASL, the 3D GRASE pCASL is known to be affected by inaccurate estimation of M^0_b from its control image (Alsop et al., 2015). To address this issue, we conducted auxiliary scans and obtained a scaling factor to correct for absolute CBF measurement from 3D GRASE pCASL. In addition, we carefully confirmed no significant differences between regional CBF increase rate from 3D GRASE pCASL dataset only and regional CBF increase rate from multi-slice pCASL dataset only. Despite these processes, the age-dependent CBF changes shown in Figure 2.5 and Figure 2.6 may be affected by measurement offsets caused by protocol differences. Future studies with CBF measurements of preterm brains from uniform pCASL protocol are warranted to validate the findings in the present study. The moderate-to-strong reproducibility in Figure 2.7 may be related to the procedure that two tests were conducted within one-session. But regional CBF changes from day to day in neonates. To remove the effects of CBF changes due to rapid brain development between two dates, we conducted reproducible tests within one scan session instead of two scan sessions on different dates. Exposure to the extrauterine environment could affect the measured CBF distribution and dynamics, but these effects would be relatively subtle compared with the dramatic developmental factor during the 3rd trimester (Bourgeois et al., 1989; Kostovic, 1990). After regressing the postnatal age, we found the correlation between frontal or occipital CBF and age was still significant. Of the note, it is likely that the regional CBF deviation from the normal CBF developmental curve due to preterm effects could become apparent in years subsequent to premature birth. Several major imaging parameters of pCASL were adjusted to be adapted to preterm brains. To better estimate the regional CBF from ASL, future studies will benefit from collecting subject-specific information for adjusting these imaging parameters. For example, individual subject's hematocrit can be used for subject-specific blood T1 estimation (Liu, et al, 2015). In addition, larger sample size may reveal nonlinear regional CBF change curves instead of simple linear lines used in this study, and longitudinal dataset may remove the effects caused by the individual differences.

2.6 Conclusion

In summary, the present study revealed spatiotemporally heterogeneous increases of cortical regional CBF in preterm brains scanned with pCASL MRI during 32-45PMW, a period of rapid brain development. Dramatic global CBF increases were found with PC MRI in parallel with heterogeneous regional CBF increases based on pCASL MRI. In addition, significant correlations between cortical CBF and cortical FA measurements in the frontal cortex suggest an association between active cellular processes causing microstructural changes and local CBF increases meeting the metabolic demand of these processes. Multimodal MRI provides a noninvasive means for characterizing changes in cortical structure and function during preterm brain development, and the metabolic need of complicated yet precisely organized cellular processes during 3rd trimester brain development can be assessed using MRI-based measures of CBF. Relatively high reproducibility of CBF measurements obtained in present study demonstrate the feasibility of using pCASL to study the regional CBF of preterm brains aged 32-45PMW on a 3T MRI scanner.

Chapter 3

Investigate the Atypical White Matter (WM) Development in Children with Autism Spectrum Disorder (ASD) aged from 2 to 7 years

3.1 Introduction

Autism spectrum disorder (ASD) is a neurodevelopmental disorder with multiple causes (Penagarikano, et al., 2011; Zhao, et al., 2007). It is behaviorally defined based on impairments in communication and social interactions, repetitive and ritualized behaviors, and restricted interests (APA, 2000; Kanner, 1968). The diagnosis of ASD often can be reliably determined by age 2 years (Baird, et al., 2003), although the mean age at which children are initially diagnosed is frequently higher (range 38-120 months) (Daniels and Mandell, 2013). Identifying atypical brain white matter (WM) processes in early childhood is critical to understanding the neurobiology of the disorder and may be informative for identifying the disorder earlier in its course.

Diffusion tensor imaging (DTI), one type of magnetic resonance imaging (MRI) capable of delineating macroscopic WM tract pathways and detecting WM microstructural pathology by measuring water diffusion in the brain (Basser, et al., 1994), may be particularly useful for identifying early emerging WM neurodevelopmental alterations in ASD. The directional dependence of water diffusion preferentially along the axis of an axonal bundle makes noninvasive tracing of WM tracts possible with DTI tractography (Mori, et al., 1999; Wakana, et al., 2007). Fractional anisotropy (FA), one of the most widely used DTI derived metrics, characterizes the shape of the diffusion tensor and is sensitive to WM microstructural disruption (Beaulieu, 2002). Radial diffusivity (RD), quantifying the magnitude of diffusion orthogonal to the principal diffusion direction, is believed to reflect the extent of WM myelination (Song, et al., 2005). The WM anatomy can be delineated with a digital WM atlas and parcellated into 48 major WM tracts (Mori, et al., 2008). These WM tracts are categorized into five functionally distinguished tract groups (Huang, et al., 2012a; Wakana, et al., 2004), namely commissural (right-left hemispheric connections), association (cortex-cortex connections), limbic (connectivity in the limbic system), projection (cortex-spinal cord, cortex-thalamus connections) and brainstem (including brain stem and cerebellar WM) tract groups.

The majority of DTI studies investigating ASD have focused on the age range from mid-childhood and adolescence to adulthood (e.g. Barnea-Goraly, et al., 2005; Travers, et al., 2012) when the clinical manifestations have well emerged (Paus, et al., 2008). These studies demonstrated decreased FA, increased mean diffusivity (MD) and increased RD in individuals with ASD compared to those with typical development (TD). DTI studies of children with ASD less than 10 years of age are relatively rare and results have been inconsistent, suggesting variable age-related effects in ASD. For example, strengthened WM integrity with increased FA has been reported for various WM regions in ASD children of 1.8-3.3 years (Ben Bashat, et al., 2007), 1.5-5.8 years (Weinstein, et al., 2011) and 0.5 to 2 years (Wolff, et al., 2012). In contrast, reduced WM integrity with lower FA and higher RD has also been found in various WM regions in children with ASD of 2.6-9 years (Sivaswamy, et al., 2010) and 2-8 years (Walker, et al., 2012). Thus, WM microstructural changes of ASD are both region- and age-dependent, especially in early development. Comprehensively surveying WM microstructure and delineating the WM trajectories in early developing brains of 2-7 years of ages may potentially address the inconsistency described above.

Early years of life including 2-7 years mark an important period for the formation of neural wiring patterns (Casey, et al., 2005). This period is critical for brain development and early intervention (Courchesne, et al., 2007; Sowell and Bookheimer, 2012). To date, only one reported study (Walker, et al., 2012) has been found for examining entire brain WM for children with ASD spanning age range of 2-8 years using

FA and MD from DTI. However, with critical functional and connectional role of WM tract and tract group, there has been no systematic characterization of microstructural maturation of entire WM in the context of tracts or tract groups in individuals with ASD across early childhood (ages 2-7 years). This type of study is important for determining the anatomical locations, distribution, and extent of atypical WM development within specific tract or tract group. With WM tracts underlying structural connectivity among different brain regions, quantifying the age-dependent effects of ASD on WM microstructural changes with individual tract as a reference has significance for understanding heterogeneous clinical manifestations related to different WM tract function and furthermore early brain developmental mechanisms associated with ASD.

In this study, we hypothesized that children with ASD would show early enhanced WM microstructural development but reduced WM maturation later in childhood compared to children with TD in most of major tracts. DTI data from 31 children with ASD and 19 children with TD between 2 to 7 years of age was acquired. FA and RD were measured at core WM voxels to characterize the WM microstructural changes in ASD across all 48 major WM tracts.

3.2 Material and Methods

3.2.1 Participants

All participants were male children recruited at Beijing Children's Hospital. 31 children with ASD aged 2.33 to 7.00 years (4.11±1.42 years) and 19 children with TD aged 1.99 to 6.83 years (4.00±1.42 years) participated in this study. The children with ASD were not receiving any CNS-active medications before MRI studies. Namely, they were all medication naïve children with ASD at the scan. The diagnosis of ASD was established using the Autism Diagnostic Interview-Revised (ADI-R) (Lord, et al., 1994), Childhood Autism Rating Scale (CARS), Clancy Autism Behavior Scale (CABS) (Clancy, et al., 1969) and Autism Behavior Checklist (Krug, et al., 1980), and diagnoses were confirmed based on expert opinion according to DSM-IV criteria (APA, 2000). The detailed age and clinical assessment scores for children with ASD were provided in Table 3.1. The 19 children with TD at the time of MR scan were refereed for fever (n=8), intermittent headache (n=9), and strabismus (n=2). All 19 children with TD had normal neurological examinations documented in medical record. The exclusion criteria for TD children consisted of known nervous system disease, or history of psychiatric, neurodevelopmental or systemic illness. Every child's parents provided signed consent and the protocol was approved by Beijing Children's Hospital Research Ethics Committee.

Table 3.1: Age and clinical assessment scores of children with autism spectrum disorder (ASD)

	Median	Minimum	Maximum	Interquartile range
Age(year)	3.39	2.33	7.00	2.16
Clinical assessment score				
Autism Behavior Checklist	94.00	79.00	107.00	11.50
Autism Diagnostic Interview (ADI)	53.00	41.00	67.00	7.50
Childhood Autism Rating Scale (CARS)	41.00	36.00	50.00	3.50
Clancy Autism Behavior Scale (CABS)	18.00	14.00	22.00	2.00

3.2.2 MRI acquisition for in vivo human brain

All MR scans were performed on a 3T Philips Achieva Magnetic Resonance System with sedation. DTI data were acquired using a single-shot, echo-planar imaging (EPI) sequence with Sensitivity Encoding parallel imaging scheme (SENSE, reduction factor = 2). The imaging matrix size was 128×128 with a field of view (FOV) of 256×256 mm^2. Axial slices of 2 mm thickness were acquired parallel to the anterior-posterior commissure (AC-PC) line. A total of 70 slices covered the entire brain without a slice gap. The repetition time (TR) and echo time (TE) were 7960 ms and 83 ms. Diffusion weighting was encoded along 30 independent directions and the b-value was 1000 s/mm^2. To increase the signal-to-noise ratio (SNR), two repetitions were performed.

3.2.3 MRI data processing

3.2.3.1 Quantifying the motion in DTI scan of children

Since diffusion MRI scans are quite sensitive to motion, and this is a particular concern in young children aged from 2 to 7 undergoing scanning. To address this concern, we first quantified the motion in DTI scans of all participants. In current study, all subjects were sedated during MR scans so that very limited motion artifacts were found in the DTI datasets. To quantify head motion in each DTI scan, all diffusion weighted image (DWI) volumes were aligned to the first stable image volume in the scan using automatic image registration (AIR) in DTIStudio (Jiang et al., 2006). The volume-by-volume translation and rotation from the rigid registration were calculated using the protocol in the literature (Yendiki et al., 2014). The specific measurements quantifying motions are as follows. 1) *Average volume-by-volume translation:* The translation vector between each pair of consecutive volumes was obtained from the translation component of the rigid registration. Then averaged magnitude of these translation vectors over all DWI volumes in each scan was calculated. 2) *Average Volume*-by-volume rotation: The rotation angle between each pair of consecutive volumes was obtained from the rotation component of the rigid registration. Then averaged sum of the absolute values of these rotation angles over all DWI volumes in each scan was calculated.

3.2.3.2 DTI tensor fitting and measurements of DTI-derived metrics

Automated image registration (Woods, et al., 1998) was applied to raw diffusion weighted images to correct distortion caused by eddy current. Head motions in diffusion MRI data were quantified for all subjects as described in above section. Six elements of the 3×3 diffusion tensor were determined by multivariate least-square fitting of DTI dataset. The diffusion tensor was diagonalized to obtain three eigenvalues (λ_{1-3}) and eigenvectors (v_{1-3}). The standard tensor fitting and DTI-derived metrics (FA and RD) calculation was conducted with DTIStudio (Jiang, et al., 2006).

3.2.3.3 Parcellation of WM into tracts and tract groups

A deterministic digital WM atlas (JHU ICBM-DTI-81) (Mori, et al., 2008) was used to parcellate WM into 48 major tracts with each tract having a discrete labeling from 1 to 48. These tracts were identified with unique numbers and further categorized into five tract groups including limbic, commissural, association, projection and brainstem tract groups, for characterization of the WM microstructural changes at the level of tract group (Wakana, et al., 2004).

3.2.4 Statistic analysis

3.2.4.1 Group comparisons of DTI-derived metrics between ASD and TD groups with voxel-wise and cluster analysis

DTI-derived metrics (FA and RD measurements) of ASD and TD groups were registered to ICBM-DTI-81 atlas space and compared at the WM skeleton voxels to label the WM and effectively alleviate partial volume effects (Smith, et al., 2006). Nonlinear registration tool, FNIRT in FSL (http://fsl.fmrib.ox.ac.uk/fsl/fslwiki/TBSS) package (Rueckert, et al., 1999), was applied to register FA maps of all subjects to the EVA single-subject FA template (Huang, et al., 2012a,b), for alignment to the JHU ICBM-DTI-81 atlas space. The registered FA maps of all subjects were averaged to generate a mean FA map, from which a FA skeleton mask was created. Skeletonized FA images of all subjects were obtained by projecting the registered FA images onto the mean FA skeleton mask. In the ICBM-DTI-81 atlas space, voxel-wise comparison was carried out with the skeletonized FA maps using permutation-based nonparametric statistics (Randomise, FSL tool; http://fsl.fmrib.ox.ac.uk/fsl/fslwiki/Randomise) with 5,000 permutations and the threshold free cluster enhancement (TFCE) (Smith and Nichols, 2009) method at cluster level threshold of $p<0.05$ corrected for multiple comparisons

(TFCE-corrected). Age was entered into the voxel-wise statistics as a covariate to test group differences on FA or RD measurements. The WM labeling from the JHU ICBM-DTI-81 atlas was used to label each cluster to a corresponding WM tract. Similarly, RD values were projected onto the skeleton mask obtained from mean FA image and compared between ASD and TD groups with the procedures described above.

Comparisons of FA or RD maps between ASD and TD group were conducted for all participated children of 2-7 years (31 children with ASD and 19 children with TD) and a subgroup of children with less than 4 years of age (16 children with ASD and 13 children with TD).

3.2.4.2 Comparisons of age-dependent DTI-derived metrics linear trend lines between ASD and TD groups

In addition to analysis of group differences, comparisons of age-dependent linear trend lines of the FA or RD measurements between ASD and TD groups were performed on all WM skeleton voxels in the ICBM-DTI-81 atlas space. Despite the cross-sectional nature in this study, age correlations provide a useful preliminary strategy for examining neurodevelopmental growth trajectories. General linear model (GLM), widely used for age-related trajectories, was applied to fit the age-dependent curves of the FA or RD and test differences of maturation rates of FA or RD between ASD and TD. Take FA measurement as an example. For FA measurement at any skeleton voxel from any participated subject, $FA_{i,j}$ was defined where i was the ith skeleton voxel, j denoted the participated child with ASD or TD. There were a total of M voxels in the skeleton and 50 subjects. Hence, i was from 1 to M and j was from 1 to 50. FA measurement for the skeleton voxel i of subject j can be constructed with mixed-effects model as follows:

$$FA_{i,j} = u_i + \beta_{1i} I_j + \beta_{2i} \tau_j + \beta_{3i} (Ia)_{ij} + \epsilon_{i,j} \qquad (3.1)$$

where u_i was the overall mean of the FA measurements in ith voxel; I_j was the indicator variable with I_j =1 for ASD and I_j =0 for healthy control; τ_j represented the age of jth subject; $(I\alpha)_{ij}$ was the age-group interaction term and $\partial_{i,j}$ was the error term; β_{1i}, β_{2i} and β_{3i} represent the parameters to be estimated for I_j, τ_j and $(I\alpha)_{ij}$, respectively. In ith voxel, if the age-group interaction is significantly different from zero, the effect of age on FA measurements depends on group (ASD or TD), which means the age-dependence of FA in ith voxel are different between the ASD group and TD group. The statistical procedures were performed using R version 3.0.2 (http://www.r-project.org/).

We also confirmed no statistical difference between linear and nonlinear fitting of FA or RD trend lines (see Appendix A for comparisons of linear and nonlinear fitting). The findings in the Results section below are then based on linear fitting with GLM in R software. The clusters with atypical age-dependent FA or RD changes were first identified by voxels with significant age-group interaction (non-corrected $p<0.05$) in GLM. To correct for multiple comparisons, a small-volume correction with false discovery rate (FDR), which has been used in a previous autism study (Cheng, et al., 2010), was conducted. Specifically, for each cluster selected in GLM described above, adjusted p-values were calculated for skeleton voxels in a small volume surrounding the cluster and consisting of skeleton voxels with 100 times the number of voxels of each cluster using FDR in R. Only clusters with continuous voxels > 3 and $p < 0.05$ (FDR corrected) were retained to avoid spurious results.

3.2.4.3 Quantifying the extent of atypical age-dependent changes for each WM tract and tract group

To assess the extent of atypical age-dependent changes on each individual WM tract, an affected percentage index was calculated for each tract. As shown in Figure 3.1, by integrating the labeling of the individual WM tract in Figure 3.1b (e.g. genu of corpus callosum (GCC)) to the WM skeleton transformed into the atlas space (Figure 3.1a), we can assign the skeleton WM voxels with major WM tract labels (Figure 3.1c for

GCC). In this way, the atlas labeling is overlaid to the mean skeleton in the JHU ICBM-DTI-81 space such that each skeleton voxel could be categorized into one of the major tracts. The tract (GCC in this example) from the atlas was three-dimensionally (3D) reconstructed in a transparent brain as anatomical guidance (Figure 3.1d). The affected percentage of a tract was determined by the ratio between the skeleton voxel number of abnormal clusters in this tract and the total skeleton voxel number of this tract. Similarly, to assess the extent of the atypical age-dependent changes in each tract group, the affected percentage for a tract group was determined by the ratio between the skeleton voxel number of abnormal clusters in this tract group and the total skeleton voxel number of this tract group.

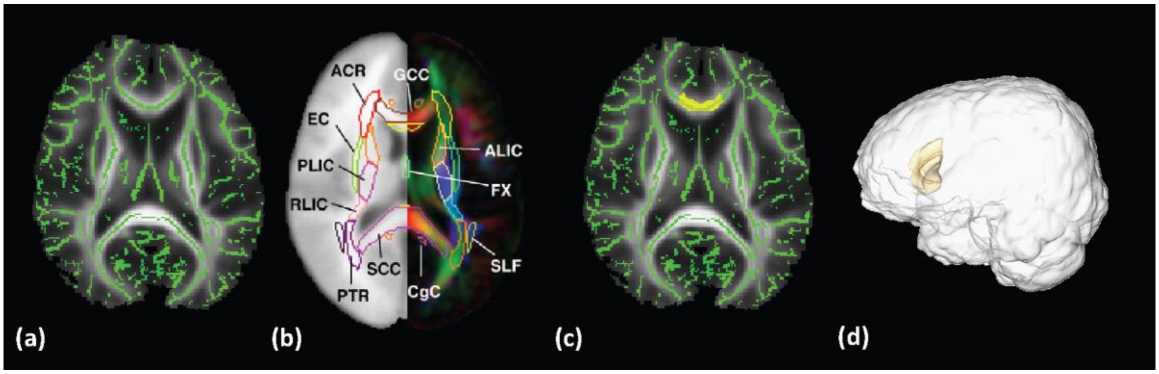

Figure 3.1: Parcellation of core white matter (WM) into different tracts with a digital atlas. (a) Green skeleton representing core WM is overlaid on the averaged FA map; (b) the ICBM-DTI-81 digital WM atlas; (c) as an example, the genu of corpus callosum (GCC) (yellow) is transferred from the digital atlas to cover the green skeleton overlaid on the averaged FA map; (d) 3D depiction of GCC in reconstructed brain. *Abbreviations of commissural tracts:* BCC, body of corpus callosum; GCC, genu of corpus callosum; SCC, splenium of corpus callosum. *Abbreviations of limbic tracts:* BFX, body of fornix; CGC, cingulum bundle at cingulate gyrus; CGH, cingulum bundle at hippocampus; FX, fornix. *Abbreviations of projection tracts:* ACR, anterior corona radiata; ALIC, anterior limb of internal capsule; ATR, anterior thalamic radiation; CST, corticospinal tract; PCR, posterior corona radiata; PLIC, posterior limb of internal capsule; PTR, posterior thalamic radiation; RLIC, retrolenticular part of internal capsule; SCR, superior corona radiata. *Abbreviations of association tracts:* EC, external capsule; IFO, inferior fronto-occipital fasciculus; ILF, inferior longitudinal fasciculus; SFO, superior fronto-occipital fasciculus; SLF, superior longitudinal fasciculus; SLF(temporal part), superior longitudinal fasciculus (temporal part); SS, sagittal stratum; UNC, uncinate fasciculus. *Abbreviations of brainstem tracts:* CP, cerebellar peduncle; ICP, inferior cerebellar peduncle; MCP, middle cerebellar peduncle; ML, medial lemniscus; SCP, superior cerebellar peduncle. L and R indicate left and right, respectively

3.2.4.4 Age intersection of ASD and TD age-dependent WM trend lines

As we hypothesized early enhanced WM microstructural development and subsequent underdevelopment of WM tracts in ASD in the age of 2-7 years, we calculated the intersected age of two growth curves for each cluster voxel where atypical age-dependent change was found with FA or RD measurements of ASD and TD groups. Linear fitting was applied to all FA-age and RD-age fitting as there is no significant difference between linear and nonlinear (logarithmic) fitting (see Appendix A for comparisons of linear and nonlinear fitting). Take FA measurement as an example. After removing the age-group intersection term in Equation 3.1, the separate linear fitting between FA measurements from ASD or TD groups and age was modeled as Equation 3.2.1 and 3.2.2, respectively.

$$FA_{i,ASDj} = u_{i,ASD} + \beta_{i,ASD}\tau_{ASDj} + \epsilon_{i,ASDj} \tag{3.2.1}$$

$$FA_{i,TDj} = u_{i,TD} + \beta_{i,TD}\tau_{TDj} + \epsilon_{i,TDj} \tag{3.2.2}$$

where *i* was the *i*th abnormal cluster, *ASDj* or *TDj* denoted the participated child with ASD or TD; $u_{i,ASD}$or $u_{i,TD}$was the overall mean of the FA measurements in *i*th cluster in ASD group or TD group; τ_{ASDj} or τ_{TDj} represented the age of *ASDj*th or *TDj*th subject in each group; $\epsilon_{i,ASDj}$ and $\epsilon_{i,TDj}$ was the error term; $\beta_{i,ASD}$ and $\beta_{i,TD}$ represented the parameters to be estimated for each cluster in each group. The intersected age $\tau_{i\_intersect}$ of the two fitted lines from ASD and TD group was calculated in Equation 3 below:

$$\tau_{i\_intersect} = \frac{u_{i,ASD} - u_{i,TD}}{\beta_{i,TD} - \beta_{i,ASD}} \tag{3.3}$$

Histograms of the intersected ages at the cluster voxels from FA and RD measurements were plotted.

3.3 Results

3.3.1 Characterization of the motion in the DTI scan of children with ASD and TD

For visual inspection, Figure 3.2 shows the DTI maps from representative subjects covering each year from 2 to 7 years of age. Figure 3.3 shows the histograms of the averaged volume-by-volume translation (0.46 ± 0.08 mm) and rotation (0.12 ± 0.04 degrees) measurements from scans of all 50 participated subjects. Few motion artifacts were observed in the present groups of DTI datasets.

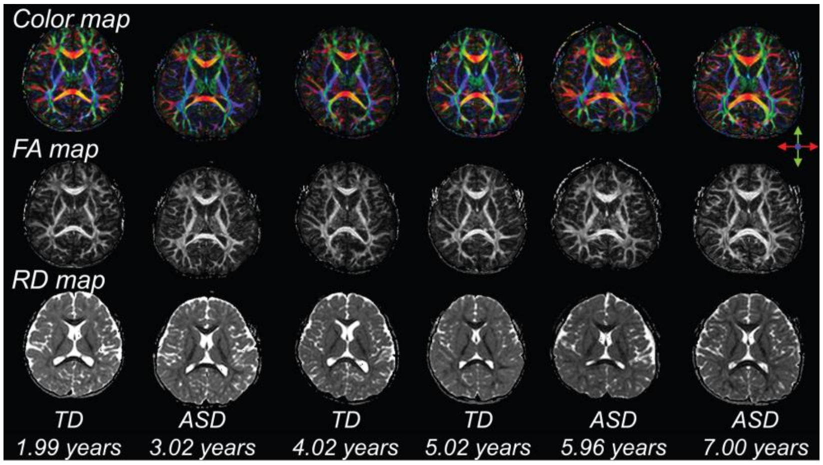

Figure 3.2: DTI map, namely direction-encoded colormap (upper row), FA map (middle row) and RD map (lower row) from 6 representative subjects with the age range from 1.99 to 7 years old. DTI maps of from representative subjects of around 2, 3, 4, 5, 6 and 7 years of age are shown from left to right. Images from both children with ASD and those with TD are included above.

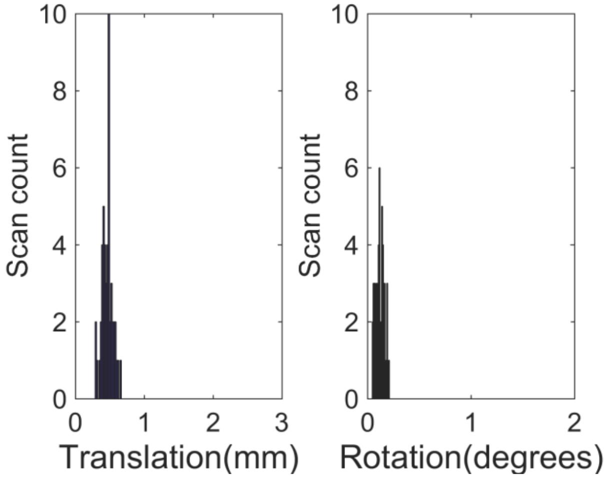

Figure 3.3: Histograms of the averaged volume-by-volume translation measurement and rotation measurement for the scans of all participated subjects (31 children with ASD and 19 children with TD) included in our analysis.

3.3.2 Enhanced WM microstructural development of children with ASD less than 4 years of age

From Figure 3.4a and Table 3.2, exclusively higher FA and exclusively lower RD were found for children with ASD of 2-4 years of age compared to age-matched children with TD, suggesting enhanced WM microstructural development for children with ASD by 4 years of age. On the contrary, differences of FA and RD between ASD and TD groups have two directions when the age range expands from 2-4 years to 2-7 years, as shown in Figure 3.4b and Table 3.3. The mixed WM microstructural changes indicate age-dependent ASD effects, which can be further delineated with the atypical age-dependent WM microstructural trend lines described below.

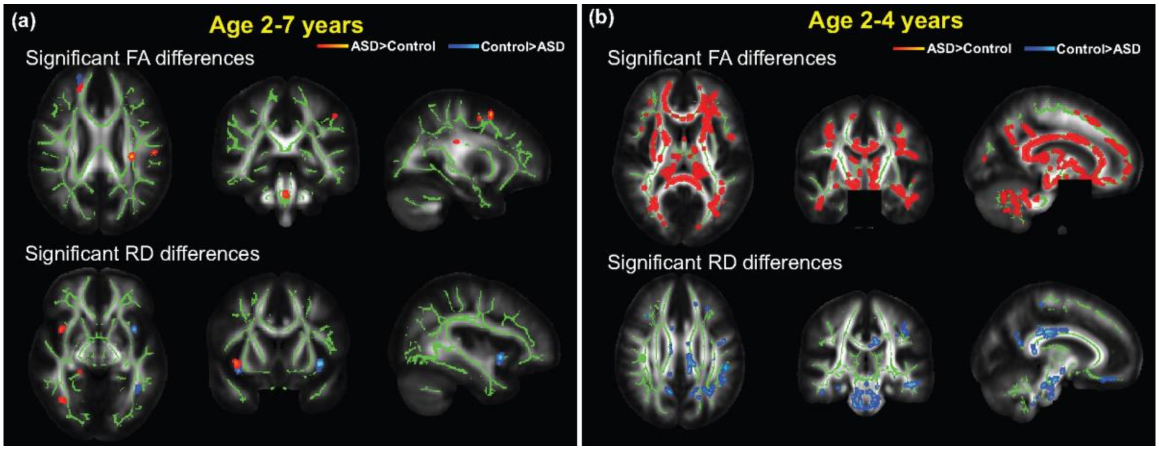

Figure 3.4: Exclusively higher FA (red-yellow; upper panels) and lower RD (blue-cyan; lower panels) widely distributed in the WM were found in ASD less than 4 years of age, compared to age-matched TD (a); Bi-directional FA (red-yellow for one change direction and blue-cyan for another; upper panels) and RD (red-yellow for one change direction and blue-cyan for another; lower panels) changes sparsely distributed in the WM were found in ASD of 2-7 years of age compared to age-matched TD (b). Voxels with statistically significant FA or RD differences between ASD and TD are displayed in red-yellow (ASD>TD) or in blue-cyan (TD >ASD). WM skeleton voxels are shown in green. In (a) or (b), axial, coronal and sagittal views are shown from left to right.

3.3.3 Atypical age-dependent microstructural linear trend lines widely distributed in WM in ASD

Atypical age-dependent WM microstructural linear trend lines of ASD compared to those of TD were observed in widespread clusters distributed in multiple tracts of all five tract groups, limbic (Figure 3.5a), association (Figure 3.5b), brainstem (Figure 3.6a), commissural (Figure 3.6b), and projection (Figure 3.6c) tract group. The progressive increases of FA values averaged from the largest cluster in each affected tract were observed for TD group with significant correlations ($p<0.05$ for all scatter plots in the left panels in Figure 3.5-3.6) between FA and age, while flattened developmental trend lines (reduced WM microstructural maturation with age) of FA values were observed for ASD group with no significant correlation ($p>0.05$) for most scatter plots in the left panels in Figure 3.5-3.6 between FA and age.

Table 3.2: FA (a) and RD (b) values, number of voxels, t and p values of the identified largest cluster in each affected WM tract from group comparison at skeleton voxels between ASD and TD subgroups with age less than 4 years. L and R indicate left and right, respectively. See legend of Figure 3.3 for WM tract abbreviations

Table 3.2 (a)

White matter tract	**FA of TD (n=13)**	**FA of ASD (n=16)**	**# of Voxels**	**t**	**p**
ASD>TD from FA measurements					
Commissural tract group					
Forceps major	0.51±0.03	0.54±0.03	1738	2.77	0.0100
Forceps minor	0.47±0.03	0.49±0.03	2973	2.14	0.0413
Limbic system tract group					
CGC-R	0.46±0.04	0.52±0.06	14	3.19	0.0036
CGC-L	0.44±0.04	0.47±0.03	359	2.78	0.0098
CGH-R	0.41±0.03	0.45±0.06	55	2.47	0.0199
CGH-L	0.41±0.02	0.43±0.04	203	2.70	0.0119
Projection tract group					
ATR-R	0.40±0.01	0.42±0.02	1459	2.23	0.0345
ATR-L	0.37±0.02	0.38±0.02	2155	2.14	0.0415
CST-R	0.56±0.02	0.57±0.02	1153	2.67	0.0126
CST-L	0.57±0.02	0.58±0.02	705	2.40	0.0235
Association tract group					
IFO-R	0.42±0.03	0.44±0.03	2111	2.26	0.0323
IFO-L	0.41±0.02	0.43±0.02	2403	2.66	0.0129
ILF-R	0.42±0.02	0.44±0.02	1026	2.06	0.0493
ILF-L	0.39±0.02	0.42±0.02	1465	2.97	0.0062
SLF-R	0.42±0.02	0.44±0.02	1216	2.75	0.0104
SLF-L	0.40±0.02	0.43±0.02	2475	3.83	0.0007
UNC-R	0.42±0.03	0.44±0.03	358	2.60	0.0150
UNC-L	0.39±0.03	0.42±0.02	903	2.67	0.0128
SLF(temporal part)-R	0.45±0.02	0.47±0.02	530	2.39	0.0242
SLF(temporal part)-L	0.43±0.02	0.45±0.02	1379	3.35	0.0024
Brainstem tract group					
MCP	0.57±0.03	0.60±0.03	256	2.23	0.0342
ML-R	0.40±0.04	0.44±0.04	48	2.19	0.0372
ML-L	0.43±0.04	0.46±0.03	51	2.23	0.0355
SCP-R	0.67±0.03	0.69±0.03	56	2.37	0.0258
CP-R	0.53±0.05	0.57±0.05	14	2.17	0.0392
CP-L	0.63±0.04	0.66±0.03	95	2.75	0.0109

Table 3.2 (b):

White matter tract	**RD (x10^{3}mm^2/s)of TD (n=13)**	**RD (x10^{3}mm^2/s) of ASD (n=16)**	**# of Voxels**	**t**	**p**
ASD<TD from RD measurements					
Commissural tract group					
Forceps major	0.59±0.04	0.56±0.04	1670	2.30	0.0293
Limbic system tract group					
CGC-R	0.62±0.05	0.57±0.04	13	3.22	0.0033
CGC-L	0.61±0.04	0.59±0.04	304	2.07	0.0486
CGH-R	0.65±0.05	0.61±0.06	36	2.18	0.0379
CGH-L	0.64±0.03	0.62±0.04	175	2.22	0.0352
Projection tract group					
ATR-R	0.64±0.03	0.61±0.02	1373	2.86	0.0080
ATR-L	0.65±0.03	0.62±0.02	1823	2.54	0.0172
CST-R	0.51±0.03	0.49±0.03	1161	2.19	0.0375
CST-L	0.50±0.03	0.48±0.03	972	2.08	0.0473
Association tract group					
IFO-R	0.63±0.04	0.61±0.03	614	2.32	0.0283
IFO-L	0.65±0.04	0.63±0.03	2249	2.12	0.0435
ILF-L	0.66±0.04	0.63±0.03	1446	2.23	0.0345
SLF-L	0.63±0.03	0.61±0.03	2319	2.29	0.0300
UNC-R	0.60±0.04	0.58±0.04	173	2.31	0.0291
UNC-L	0.68±0.05	0.65±0.04	64	2.37	0.0249
SLF(temporal part)-L	0.62±0.03	0.60±0.03	1260	2.13	0.0428
Brainstem tract group					
MCP	0.50±0.04	0.45±0.04	171	3.21	0.0036
ML-R	0.51±0.03	0.49±0.03	74	2.26	0.0335
SCP-R	0.41±0.03	0.39±0.02	75	2.83	0.0093
CP-R	0.48±0.03	0.44±0.03	127	3.59	0.0013
CP-L	0.48±0.04	0.43±0.03	116	3.63	0.0014

Table 3.3: FA (a) and RD (b) values, number of voxels, t and p values of the identified largest cluster in each affected WM tract from group comparison at skeleton voxels between ASD and TD group of all subjects with age of 2 to 7 years. L and R indicate left and right, respectively. See legend of Figure 3.3 for WM tract abbreviations

Table 3.3 (a):

White matter tract	**FA of TD (n=19)**	**FA of ASD (n=31)**	**# of voxels**	**t**	**p**
ASD>TD from FA measurements					
Commissural tract group					
Forceps minor	0.27±0.02	0.30±0.03	121	2.93	0.0055
Forceps minor	0.26±0.04	0.29±0.04	29	2.18	0.0345
Limbic system tract group					
CGC-R	0.28±0.05	0.33±0.05	32	2.89	0.0060
CGC-R	0.23±0.04	0.27±0.05	14	2.86	0.0064
Projection tract group					
ATR-L	0.32±0.03	0.36±0.03	155	3.85	0.0004
CST-R	0.51±0.03	0.53±0.04	18	2.10	0.0415
CST-R	0.41±0.03	0.44±0.06	15	2.33	0.0235
ATR-R	0.29±0.02	0.31±0.02	12	2.70	0.0096
Association tract group					
UNC-L	0.30±0.02	0.32±0.02	69	2.15	0.0372
SLF-L	0.34±0.03	0.38±0.04	55	3.53	0.0009
SLF-L	0.26±0.04	0.31±0.05	16	2.60	0.0126
IFO-R	0.26±0.07	0.31±0.07	11	2.31	0.0257
ASD<TD from FA measurements					
Association tract group					
SLF-R	0.37±0.09	0.31±0.09	13	2.48	0.0174

Table 3.3 (b)

White matter tract	**RD (x10^{3}mm^{2}/s) of TD (n=19)**	**RD (x10^{-3}mm^{2}/s) of ASD (n=31)**	**# of voxels**	**t**	**p**
ASD<TD from RD measurements					
Limbic system tract group					
CGC-R	0.68±0.04	0.64±0.04	59	2.86	0.0068
Projection tract group					
CST-R	0.73±0.10	0.66±0.05	10	2.53	0.0181
Association tract group					
UNC-R	0.88±0.10	0.82±0.10	18	2.03	0.0490
IFO-R	0.71±0.06	0.67±0.07	11	2.36	0.0224
ASD>TD from RD measurements					
Limbic system tract group					
CGH-L	0.61±0.07	0.67±0.10	11	2.38	0.0213
Association tract group					
SLF-R	0.64±0.07	0.69±0.07	12	2.21	0.0325
IFO-R	0.75±0.03	0.79±0.03	11	3.72	0.0006

(a) Limbic tract group

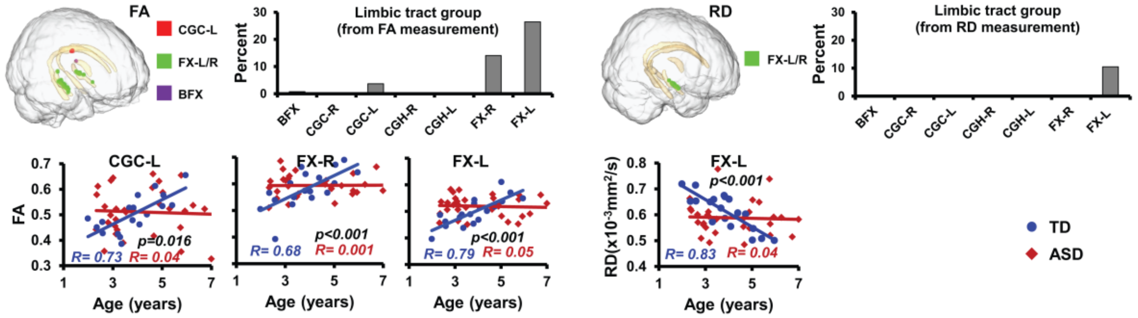

(b) Association tract group

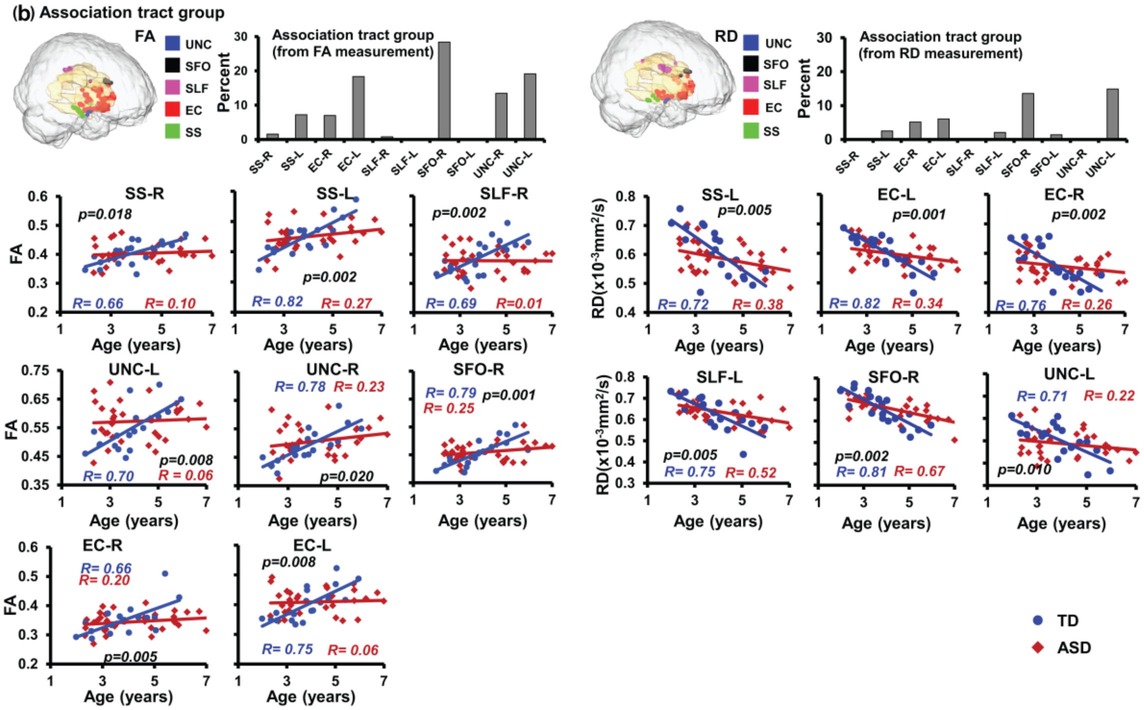

Figure 3.5: Clusters with significant age-group interactions in the limbic system (a) and association tract group (b) with FA and RD measurements. The locations and distributions of significant clusters in reconstructed limbic tracts (a) and association tracts (b) (light yellow and directly from the digital WM atlas) are visualized in 3D in the top left panel of each measurement. Significant clusters in different limbic tracts (a) and association tract (b) are coded with different colors, also shown in the top left panel of each measurement. The entire brain (gray) is also shown as anatomical reference. The percentage values of affected voxels within each limbic tract (a) and association tract (b) are shown in the bar plots in the top right panel of each measurement. Scatter plots of FA or RD averaged from the largest cluster of atypical age-dependent WM changes in each affected limbic tract (a) and association tract (b) are shown in lower panels for ASD and TD children. Each red diamond or blue circle in the scatter plot represents FA or RD measurement from one ASD or TD child, respectively. The solid lines (blue for TD and red for ASD) were linearly fitted from these measurements. R values (blue for TD and red for ASD) are correlation coefficients of FA or RD measurements and age. FDR-corrected p value in each scatter plot indicates the difference of trend line rate of these metrics between ASD and TD groups. L and R indicate left and right, respectively. See legend of Figure 3.1 for WM tract abbreviations.

Similarly, progressive RD decreases in TD group and flattened RD trend lines in ASD group were found for another set of clusters also widely distributed in WM of all five tract groups, shown in scatter plots in the right panels of Figure 3.5-3.6. The atypical WM FA or RD age-dependent trend lines of ASD are nonparallel or overlapping to those of TD, resulting in the crossing of the trend lines, shown in the scatter plots of Figure 3.5-3.6. In addition, these FA or RD change rate differences are significant for all displayed clusters in the 3D images of Figure 3.5-3.6 with FDR-corrected p values less than 0.05. For example, FDR-corrected p value is 0.011 for FA change rate difference between ASD and TD in the cluster at GCC (left panel in Figure 3.6b). FDR-corrected p value is less than 0.001 for RD change rate difference between ASD and TD in the cluster at left cerebellar peduncle (CP-L) (right panel in Figure 3.6a). The percentages of voxels with atypical age-dependent microstructural changes inside each WM tract are shown in the bar plots of Figures 3.5-3.6.

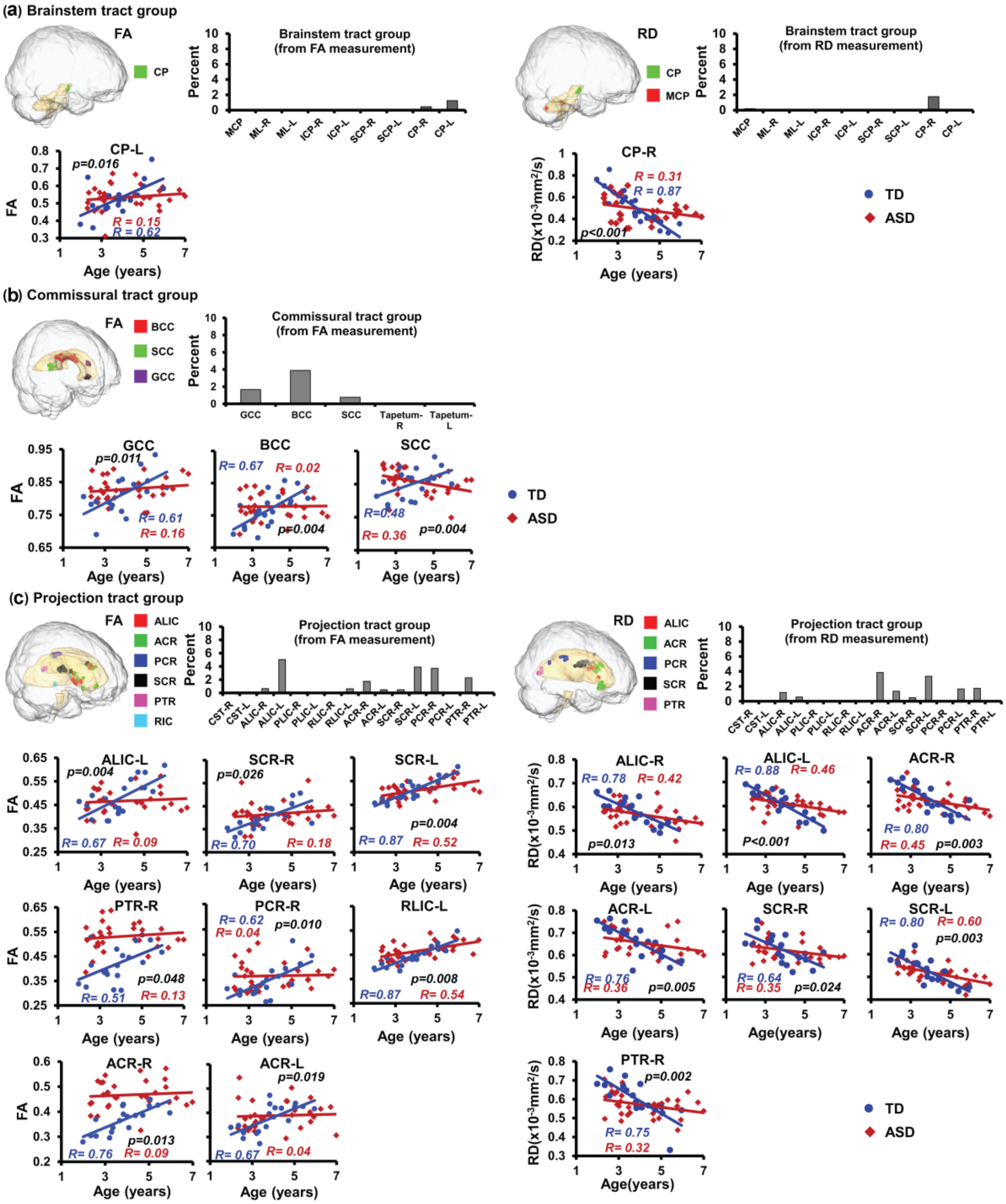

Figure 3.6: Clusters with significantly age-group interactions in the brainstem (a), commissural (b) and project tract group (c) with FA and RD measurements. See legend Figure 3.5 for details.

3.3.4 Heterogeneous extent of WM clusters with atypical age-dependent microstructural trend lines within each tract group and among different tract groups

While it is consistent that slower change rates of FA and RD of ASD were observed for the clusters in all affected WM tracts, the extents and distributions of these clusters were evidently varied across different tracts of each tract group, as shown in bar plots in Figure 3.5-3.6. Moreover, the extents of the clusters with atypical age-dependent microstructural trend lines in ASD group were varied among different tract groups, as shown in Figure 3.7a and 3.7c. Specifically, based on both FA and RD measurements, the limbic and association tract groups were more severely affected with higher percentage of WM voxels with atypical age-dependent microstructural trend lines while brainstem, commissural and projection tract groups were less severely affected. The exact percentage values of WM voxels with atypical age-dependent trend lines in ASD within each tract or each tract group from FA or RD measurements are listed in Appendix C.

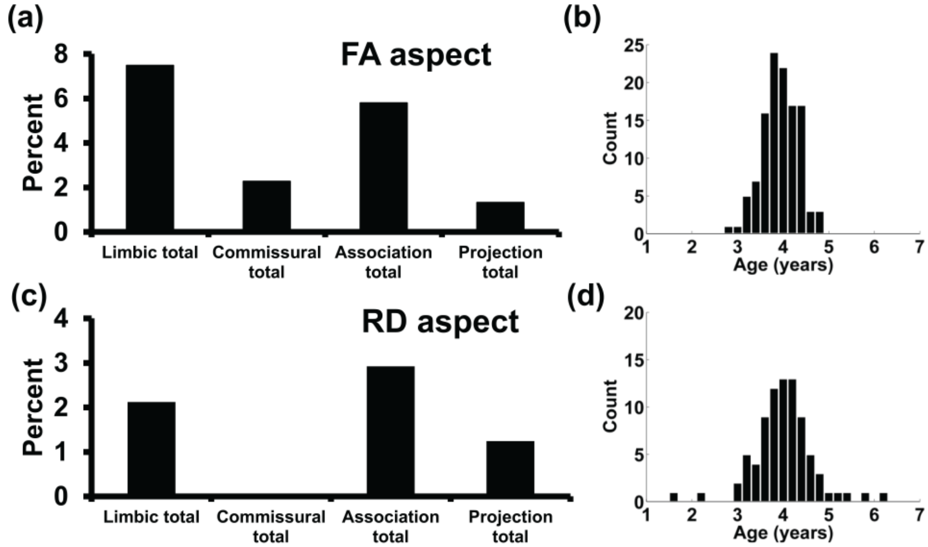

Figure 3.7: The percentage values of affected voxels within each WM tract group for FA (a) and RD (c) measurements of five major tract groups. (b) and (d) demonstrate the histograms of ages from intersections of trajectories of FA (b) and RD (d) measurements of children with ASD and those with TD, respectively.

3.3.5 Distributions of the intersected ages of age-dependent WM linear trend lines of children with ASD and TD

With intersections of FA or RD curves of ASD and those of TD clearly observed in all tract groups (Figures 3.5-3.6), the distribution of the ages of these intersections is demonstrated in Figure 3.7b and Figure 3.7d. Most trend lines intersections occurred around 4 years with both FA (3.93 ±0.39 years) and RD measurements (4.00±0.66 years).

3.4 Discussion

Atypical age-dependent WM microstructural changes of children with ASD revealed by surveying all WM tracts and tract groups offer comprehensive information for understanding WM developmental pattern affected by ASD. Specifically, the results suggest that WM undergoes early enhanced microstructural development in most major WM tracts in ASD group before 4 years of age followed by reduced rates of tract maturation through 7 years of age (Figure 3.4-3.6). Furthermore, the atypical age-dependent WM microstructural changes are heterogeneous among different WM tract groups with more prominent atypical developmental patterns observed in limbic and association tracts, compared to brainstem, commissural and projection tracts (Figure 3.7a and 3.7c). To our knowledge, this study is one of the first attempts to systematically determine the anatomical location, distribution and extent of atypical age-dependent trend lines across all major WM tracts and tract groups in young children with ASD. With each individual WM tract forming the neuroanatomical basis of global and local brain circuits, these findings provide important new evidence to understand the pattern and timing of atypical WM development in ASD with implications for how they might contribute to alterations in the circuit level organization of brain function and behavior. The comprehensive results from group comparisons at different age ranges and trajectory analyses may also help elucidate the seemingly controversial and inconsistent WM finding of children with ASD, as different patterns of WM microstructural abnormality appear to be present at different ages (e.g. Ben Bashat, et al., 2007; Sivaswamy, et al., 2010; Walker, et al., 2012; Weinstein, et al., 2011; Wolff, et al., 2012).

With FA inferring the overall WM microstructural integrity (Beaulieu, 2012) and RD being more specific to quantitatively inferring WM myelination (Song, et al., 2005), group comparisons of WM FA or RD with age as a covariate yielded ambiguous results showing both enhanced and reduced WM integrity and myelination (Figure 3.4b); on the other hand, the exclusively enhanced WM integrity and myelination was found for children with ASD less than 4 years of age (Figure 3.4a). In light of identified trend line intersection ages shown in Figure 3.7b and 3.7d, the bi-directional results in Figure 3.4b could come from mixed effects of early enhanced WM microstructural development by 4 years (Figure 3.4a) and undergrowth after 4 years. The results of Figure 3.4a-3.4b combined with the revealed age-dependent microstructural trend lines in Figure 3.5-3.6 may shed light on the inconsistent WM findings for children with ASD at this age range (2-7 years) in the literature (e.g. Ben Bashat, et al., 2007; Sivaswamy, et al., 2010; Walker, et al., 2012; Weinstein, et al., 2011; Wolff, et al., 2012). That is, mixed overgrowth before a certain age and undergrowth after that age in individuals with ASD may result in the seemingly controversial results. It suggests an age window, even a narrow one, may play a critical role for elucidating nuanced developmental differences associated with ASD.

DTI offers microstructural measurements of FA and RD to access WM maturation. Progressive FA increases and RD decreases have been found in normal WM maturational process in childhood (Lebel and Beaulieu, 2011). Figure 3.5-3.6 inferred high level of WM microstructural maturation for children with ASD until around 4-5 years of age but the maturation progressed more slowly after that age. Namely, FA or

RD of widespread WM in all five major tract groups for children with ASD before 4-5 years of age reached to a level equivalent to that of older children with TD (Figure 3.5-3.6). Stronger WM microstructural enhancement in children with ASD before 4 years of age could be associated to poorer ASD clinical symptoms, as suggested by Appendix B Figure where higher FA measurements of right cingulum bundle at hippocampus (CGH-R) and lower RD measurements of CGH-L are correlated to higher CABS. By combining the group comparison analysis and analysis of interaction of age-dependent microstructural trend lines, we were able to document the widespread nature of early WM microstructural enhancement in ASD, the intersection point at which WM growth in TD individuals catches up to that growth, and the early phase of brain growth beyond age 4 that leads to the pattern of lower FA and higher RD in ASD from late childhood to adulthood.

The widespread locations of atypical age-dependent linear trend lines in all five WM tract groups of children with ASD are possibly related to the feature of ASD as a heterogeneous spectrum disorder with a wide range of symptom severity. It affects brain functions in multiple aspects including social impairment, communication deficits and repetitive behaviors (Lord, et al., 1994; Amaral, et al., 2008). The atypical age-dependent trend lines are especially prominent in the limbic and association tract groups (Figure 3.7a and 3.7c). Alterations in trend lines of limbic WM tract (Figure 3.5a) may explain disruption of limbic circuitry (e.g. Haznedar, et al., 2000) and some clinical manifestations of ASD (e.g. Bauman and Kemper, 1987) that lead to reduced social learning experiences and impaired social development (e.g. Dawson, et al., 2004). Left superior longitudinal fasciculus (SLF), as a major association tract, connects between Broca's area and Wernicke's area, both related to language. The alterations of microstructural trajectory of FA and RD in left SLF in Figure 3.5b suggest abnormality in myelin development and might be related to slower neural transmission (Shukla, et al.,

2011) and therefore the impairment of language development seen in some children with ASD (e.g. Weinstein, et al., 2011). Atypical age-dependent microstructural trend lines of the superior fronto-occipital fasciculus (SFO) and the uncinate fasciculus (UNC) (Figure 3.5b) may contribute to impairment of attention, emotion processing, memory and language functions which these two tracts are involved with (Catani and Thiebaut de Schotten, 2008; Radua, et al., 2011). Less prominent atypical age-dependent trend lines of children with ASD were found in brain stem, commissural and projection tracts (Figure 3.7a and 3.7c), however, clusters of significant trend line differences between children with ASD and those with TD were found in these tract groups too (Figure 3.6). Previous autism study reported cerebellar dysfunction affected the establishment of neural circuitry (e.g. Allen, 2005; Mosconi, et al., 2015) involving CP and we also found atypical age-dependent WM changes in CP (Figure 3.6a). The atypical microstructural development in CC (shown in Figure 3.6b), as the large commissural tract, has been probably mostly reported in previous autism studies (e.g. Alexander, et al., 2007; Barnea-Goraly, et al., 2005). The involved projection tracts (Figure 3.6c) including internal capsule (IC) and corona radiata (CR) are related to perceptual, motor functions and other higher cognitive functions (Schmahmann and Pandya, 2008) known to be impaired in ASD (e.g. Mosconi, et al., 2015).

3.5 Limitation of current study and future perspective

Integration of WM skeleton and tract parcellation (Figure 3.1) that effectively alleviated the partial volume effects and revealed the anatomical locations in the context of WM tracts offered technical advantage of this study. While the present WM microstructural findings further develop and are consistent with the view that there is an atypical pattern of brain development in ASD, the age-dependent FA or RD curves came from cross-sectional datasets, but not longitudinal datasets from either children with ASD or children with TD. Relevantly the distribution of ages from the crossings of the fitted linear trend lines in Figure 3.7b and 3.7d cannot be interpreted as the crossings of real trajectories, either. Hence the intersections of the fitted trend lines are indirect indication of crossed ages and also depend on the model selected (see Appendix A for selection of curve fitting model). Stronger confirmation of the FA or RD trajectories and crossed ages between children with ASD and those of TD will come from future longitudinal studies (see e.g. Hedman, et al., 2012 for review of longitudinal brain volume measurements and Lebel and Beaulieu, 2011 for longitudinal trajectories of FA and MD). Corrections of multiple comparisons were conducted for both group comparisons of FA or RD maps and analyses of intersections of FA or RD linear trend lines between ASD and TD groups. Caution needs to be taken to interpret results of FA and RD which are used to infer the WM microstructural integrity and myelin, respectively, but are not direct measures of axonal density or myelin level (Wheeler-Kingshott and Cercignani, 2009).

3.6 Conclusion

In conclusion, we identified microstructural enhancement in widely distributed multiple WM tracts, particularly in associational and limbic tracts, in children with ASD before 4 years of age and a reduced rate of WM maturation after that age. With WM tracts underlying brain circuits and connectivity, characterizing the atypical age-dependent WM trend lines, specifically the anatomical locations, distribution and extent of the affected WM within specific tracts and tract groups, have potential implications for identifying children at highest risk for ASD and targeted preventive interventions.

Chapter 4

Short-range association fibers in human brain with typical development and autism spectrum disorder (ASD)

4.1 Introduction

The white matter (WM), including both deep and superficial ones, consists of fibers that connect different brain regions. Among these fibers, the cortico-cortical connections are called association fibers. From early childhood to adulthood, the WM undergoes dramatic modifications including progressive increases of volume, myelination and changes in axonal diameter, in conjunction with brain network reconfiguration (e.g. Gong et al., 2008; Sepulcre et al., 2010). Short-range association fibers (SAF), also known as U-fibers, connect adjacent gyri and locate in superficial WM (SWM) region laying immediately beneath cortical gray matter (GM). SWM constitutes the majority of white matter (WM) in the human brain (Schüz and Braitenberg, 2002). However, unlike long-range association fibers (LAF) or deep WM (DWM) region, whose location (e.g. Wakana et al., 2004 and 2007), trajectories (e.g. Lebel et al., 2012) and functions (e.g. Catani and de Schotten, 2008) have been well characterized, little is known about the SAFs during the brain developing. How SAFs reshape the brain network configuration during typical and atypical development is also not sufficiently studied.

Diffusion magnetic resonance imaging (dMRI), a type of MRI technique, is capable of delineating in vivo microstructural changes of WM fibers noninvasively by measuring the water diffusion in these fibers (Basser et al., 1994). With dMRI-based tractography (e.g. Behrens et al., 2007; Mori et al., 1999), WM fibers can be traced to infer structural connectivity in the human brain. Numerous studies have been conducted previously to characterize developmental human brain connectivity (Huang et al., 2006; Lebel and Beaulieu, 2011; Yu et al., 2014) and network (e.g. Dennis et al., 2013;

Hagmann et al., 2010; Huang et al., 2015; Yap et al., 2011) based on dMRI tractography.

Recent studies on structural network of developing brains (e.g. Dennis et al., 2013; Hagmann et al., 2010; Huang et al., 2015; Yap et al., 2011) suggest that emergence of the maturing brain networks are associated with both enhancement of some WM fibers and synaptic pruning of other fibers. In addition, network-based measurements representing local connectivity efficiencies were found to decrease significantly possibly due to synaptic pruning (Huang et al., 2015). However, the developmental brain connectome is incomplete without an understanding of SAFs. Further insights into the underlying mechanism of growing human brain networks requires information on not only microstructural enhancement of LAFs, but also pruning of SAFs. Delineation and quantification of SAFs, combined with the existing knowledge of LAFs, will provide a more complete characterization of the structural basis of observed mesoscale network changes during development. Direct measurement of the elimination of SAFs holds the key to filling an existing knowledge gap of developmental brain connectome under normal and pathological circumstances.

Effectively characterizing SAF has major impact on delineating normal brain development and has translational potential as a biomarker for a suite of mental disorders. The perturbation of the developmental trajectory of SAF may cause mental disorders such as autism spectrum disorder (ASD) and schizophrenia (e.g. Courchesne and Pierce, 2005; Innocenti and Price, 2005; Paus et al., 2008). In individual with ASD, a pattern of local or short-distance “functional over-connectivity”, in parallel to the long-range under-connectivity, has been frequently suggested (e.g. Courchesne et al., 2007; Keown et al., 2013; Rudie et al., 2013; Supekar et al., 2013; Vissers et al., 2012; Wass, 2011). Both functional and structural long-distance connectivity appears to be weaker in ASD than in controls (e.g. Courchesne and Pierce, 2005; Martino et al., 2014). However, little is known about spatiotemporal characterization of “structural” short-distance connections in typically developing (TD) children or children with ASD. We hypothesized that altered trajectories of SAF are not uniform across brain regions, and altered trajectories occur in higher-order brain regions in children in ASD.

In this study, we developed and measured a novel index named normalized short-range association fibers (NSAF), defined as the ratio of the number of SAFs to the number of brain cortico-cortical connectivity fibers (sum of SAF and LAF) traced from a given cortical gyrus, to study the short-range connection in human brain. Both regional and whole brain NSAF was established with quantification of SAF reconstructed with dMRI-based tractography. We first evaluated the spatiotemporal pattern of both whole brain and regional NSAF with 21 healthy subjects 2-25 years. Estimates of NSAF values were then used to explore how SAF underlies brain network reconfiguration with network measurement in young children with TD aged 2-7 years. Finally, we applied NSAF measurements to a group of young children with ASD aged 2-7 years to examine the maturation of short-range connectivity under pathological condition.

4.2 Material and Methods

4.2.1 Participants

All participants were recruited and scanned at the Beijing Children’s Hospital of Capital Medical University in Beijing, China. The study was approved by the Institutional Review Board (IRB) at Beijing Children’s Hospital. Subjects or their guardians (if subjects are under 18 years old) gave written informed consents for all study procedures.

4.2.1.1 Study 1: Whole brain and regional NSAF in typical developmental human brain

A total of 21 healthy children, adolescents and young adults between the ages of 2 and 25 years (16 male and 5 female; 13.03±8.32 years) were participated in study 1 and all of them were medically healthy and had no known neurological or psychiatric disorders. They were not under any intervention or medication known to affect the central nervous system.

4.2.1.2 Study 2: SAFs underlie brain network reconfiguration and sensitivity of NSAF in typically and atypically developing children

31 children with ASD aged 2.33 to 7.00 years (all male; 4.11±1.42 years) and 20 children with TD aged 1.99 to 6.83 years (all male; 3.98±1.07 years) participated in this study. The children with ASD were not receiving any CNS-active medications before MRI studies. Namely, they were all medication naïve children with ASD at the scan. The diagnosis of ASD was established using the Autism Diagnostic Interview-Revised (ADI-R) (Lord, et al., 1994), Childhood Autism Rating Scale (CARS), Clancy Autism Behavior Scale (CABS) (Clancy, et al., 1969) and Autism Behavior Checklist (Krug, et al., 1980), and diagnoses were confirmed based on expert opinion according to DSM-IV criteria (APA, 2000). The 20 children with TD at the time of MR scan were refereed for fever (n=8), intermittent headache (n=9), and strabismus (n=3). All 20 children with TD had normal neurological examinations documented in medical record. The exclusion criteria for TD children consisted of known nervous system disease, or history of psychiatric, neurodevelopmental or systemic illness.

4.2.2 Acquisition of dMRI and T_1 weighted image

For both studies, all MR scans were performed on a Philips 3T Achieva Magnetic Resonance System (Philips Healthcare, Best, The Netherlands). dMRI were acquired using single-shot, echo-planar imaging (EPI) sequence with Sensitivity Encoding parallel imaging scheme (SENSE, reduction factor = 2.3). Diffusion parameters were as follows: TR/TE=7960/83ms, field of view (FOV) = 224x224mm^2, in-plane imaging resolution= 2x2mm^2, axial slice thickness=2mm, slice number=65 covering the entire brain without a slice gap, 30 independent diffusion-weighted directions [23], uniformly distributed in space, with b-value of 0 and 1000 sec/mm^2. T_1 weighted images were acquired using magnetization-prepared rapid gradient-echo (MPRAGE) sequence with FOV = 200x180mm^2, in-plane imaging resolution= 1x1mm^2, slice thickness=1mm, slice number=160 covering the entire brain. The T_1 weighted images provided superior gray and white matter contrast and were used for parcellation of the cerebral cortex. dMRI and T_1 weighted images were acquired within the same session.

4.2.3 Normalized short-range association fibers (NSAF)

Fiber tracing from a parcellated cortical gyrus: The pipeline for WM fiber tracing from a certain cortical gyrus (inferior parietal gyrus or IPG was used as an example), namely cortical parcellation determining the tractography seed region of interest (ROI), is demonstrated in Figure 4.1a-4.1h. Based on the T_1 weighted image of each subject (Figure 4.1a) the brain cortical surface of each hemisphere was rendered and parcellated into 34 gyral labels (Desikan et al., 2006) (Figure 4.1b) using *FreeSurfer* (http://surfer.nmr.mgh.harvard.edu, Version 5.0.1), a semi-automated software suit. Fiber assignment of continuous tractography (FACT) (Mori et al., 1999) was used to trace the whole brain fibers (Figure 4.1f) for all subjects in *DiffusionToolkit* (http://www.trackvis.org/dtk/). After tensor fitting, a principal eigenvector turning angle threshold of 60 degrees were used for FACT tractography. Linear affine transformation was applied to reorient and transform the parcellated cortical labels into dMRI space with skull-stripped b0 image (Figure 4.1e) and skull-stripped T_1 weighted images as the transformation target and subject, respectively with *Diffeomap* (http://www.mristudio.org). The same linear transformation re-sliced the gyral labeled image using nearest neighbor interpolation. Due to the dense WM zones just beneath the infragranular layers of the cortex impeding tracking (Reveley et al., 2015), the parcellated cortical ribbon in dMRI space (Figure 4.1c) was then dilated by 8mm (dilated IPG shown in green overlaid on skull-stripped b0 image in Figure 4.1g) using a custom program written in IDL (Interactive Data Language 8.2.3, http://www.exelisvis.com) to get through the dense WM zone for initiating fiber tracking (Reveley et al., 2015). The depth of dilation has been evaluated in our previous study (Jeon et al., 2015). Using the whole brain dilated cortical ribbon as a binary mask, cortico-cortical association fibers with both terminations within the mask were retained (cortex-spinal cord, cortex-brainstem, and cortex-thalamus fibers were excluded in this study). Cortico-cortical association fibers initiated from IPG as a seed ROI are shown in Figure 4.1h.

Categorization of long- and short-range fibers based on termination location of the other end of fibers: For all 68 pacellated cortical gyrus, the adjacent and non-adjacent gyral labels to each cortical gyral label were identified. Using IPG (shown in green in both 3D reconstructed brain and 2D slice) in Figure 4.1i as an example, its adjacent gyri are superior parietal gyrus(yellow), lateral occipital gyrus(red) and supra marginal gyrus(blue) and all other gyri are non-adjacent gyri to IPG. Then cortico-cortical association fibers initiated from IPG can be categorized into short- and long-range association fibers based on the other end of fibers terminating in adjacent gyri and non-adjacent gyri to IPG respectively (Figure 4.1j). Regional NSAF of IPG was calculated as the ratio between the number of SAF and the total number of association fibers initiated from IPG (including both SAF and LAF). Whole brain NSAF was calculated as the ratio between the total number of SAF and that of whole brain association fibers from all 68 gyral labels.

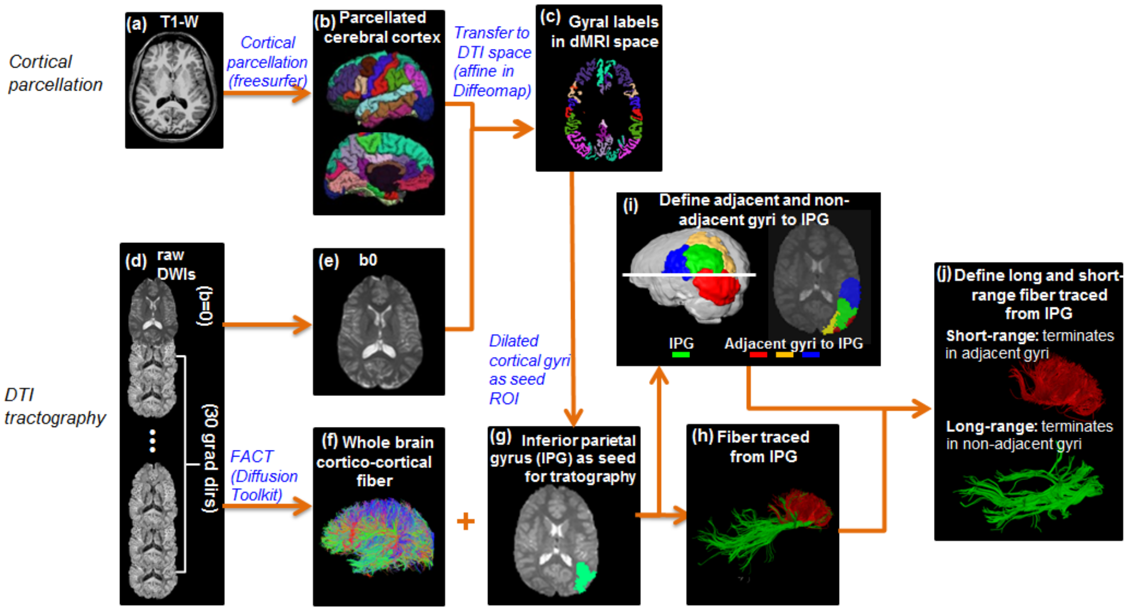

Figure 4.1: The schematic pipeline of the cortical parcellation (a-c), fiber tracing (d-h) and categorization of long- and short-range fibers (i-j) from a certain cortical gyrus with T1-weighted (a) and dMRI data (d).

4.2.4 Structural network construction and network analysis

To investigate how SAF, reflected by NSAF measurement, underlie the brain network reconfiguration during development, structural network based on dMRI tractography was constructed. Nodes and edges are two fundamental elements of a network. In this study, the 68 cortical regions, parcellated with T1-weighted images (Figure 4.2d-4.2e) and transferred to dMRI space (Figure 4.2a), were included for constructing the WM network, each representing a done of the brain network. Similarly as NSAF calculation, the cortical regions were dilated 8 mm in order to get through the dense WM zone for initiating fiber tracking (Figure 4.2f). FACT (Mori et al., 1999) was used to trace the whole brain fiber with an angular threshold of 60 degree (Figure 4.2 a-4.2c). Two cortical regions were considered structurally connected if there exist at least one fiber or reconstructed streamline with two end-points located in these two regions. A symmetric 68×68 brain connection matrix was constructed using the number of fibers multiplied by the mean fractional anisotropy (FA) (FN×FA) of all connected fibers between two cortical regions to define the weight of the edge (Figure 4.2c, 4.2f-4.2g). Three-dimensional representation of WM structural network is shown using *BrainNetViewer* software (https://www.nitrc.org/projects/bnv) (Figure 4.2g) .All network analyses were performed using Gretna (http://www.nitrc.org/projects/gretna/).

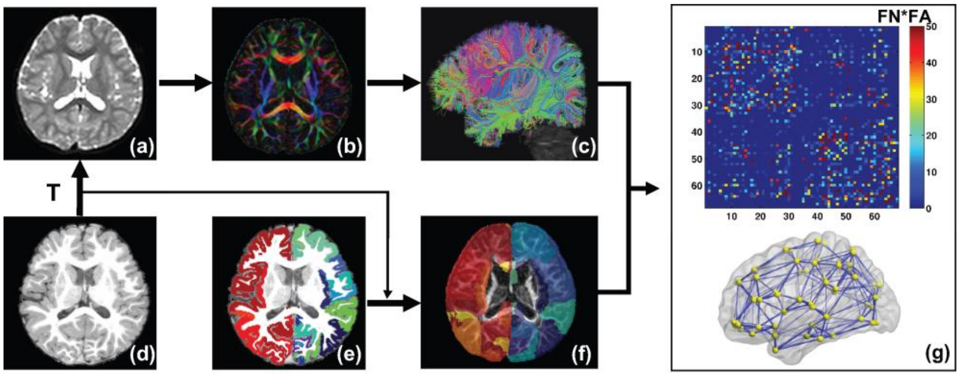

Figure 4.2: The flowchart of structural brain network construction using diffusion MRI. The schematic pipeline of fiber tracing (a-c), cortical parcellation (d, e), and structural brain network construction (c, f, g).

In this study, the global efficiency of the brain structural network graph (G), reflecting the efficiency of the parallel information transfer in a network (Latora and Marchiori, 2001), was computed with equation 4.1:

$$E_{global}\,(G) = \frac{1}{N(N-1)} \sum_{i \neq j \in G} \frac{1}{L_{ij}} \qquad (4.1)$$

where L_{ij} is the shortest path length, defined as the sum of the edge lengths along this path, between node i and node j in network G.

4.2.5 Statistic analysis

Study 1: Whole brain and regional NSAF developmental trajectory analysis from early childhood to adulthood: To explore the developmental change of whole brain or regional NSAF, complex growth models (the quadratic model and the cubic model) were used. The following equation was used for fitting a quadratic or cubic model between y (whole brain or regional NSAF) and age t,

$$y = \beta_0 + \beta_1 * t + \beta_2 * t^2 + \beta_3 * t^3 + \varepsilon \qquad (4.2)$$

Where β_0, β_1, β_2 and β_3 were parameters to be estimated and ε was an error term. Note that β_3 is for cubic fitting only. For whole brain or regional NSAF, the age at which the lowest value of NSAF reached (the point where decrease gives ways to increase) can be determined from the first order derivative of the fitted developmental curves, which may be potentially useful index of cortical maturation. Hence, lowest NSAF of the whole brain and three representative cortical regions: primary somatosensory cortex (S1), visual cortex (V1) and prefrontal cortex were also calculated. Statistical analysis was computed using R statistical software version 3.0.2 (https://www.r-project.org/).

Study 2: SAF underlie brain network reconfiguration in typically and atypically developing children: To investigate the relationship between whole brain NSAF and global network efficiency, linear regression was performed.

Study 2: Developmental curves of regional NSAF in young children with ASD or TD aged 2-7 years: To investigate the developmental cure of regional NSAF, linear regression was performed between NSAF values and age in four representative functional regions: prefrontal cortex, default-mode network (DMN) hub (precuneus cortex), S1 and V1 cortex.

4.3 Results

4.3.1 Study 1: Whole brain and regional NSAF in TD brain from early childhood to adulthood

Long- and short-range association fibers traced from a certain cortical gyrus: Figure 4.3 shows the categorization and balance of SAF and LAF initiated from a given cortical gyrus of three representative subjects at 2 years (young child), 12 years (adolescent) and 22 years (adult) of age, using IPG (ROI shown in green and overlaid on the fibers) as an example. It is clear that LAF traced from IPG are strengthened and denser in older subjects (12 years and 22years) when compared to that from younger subject (2 years), while SAF look similar.

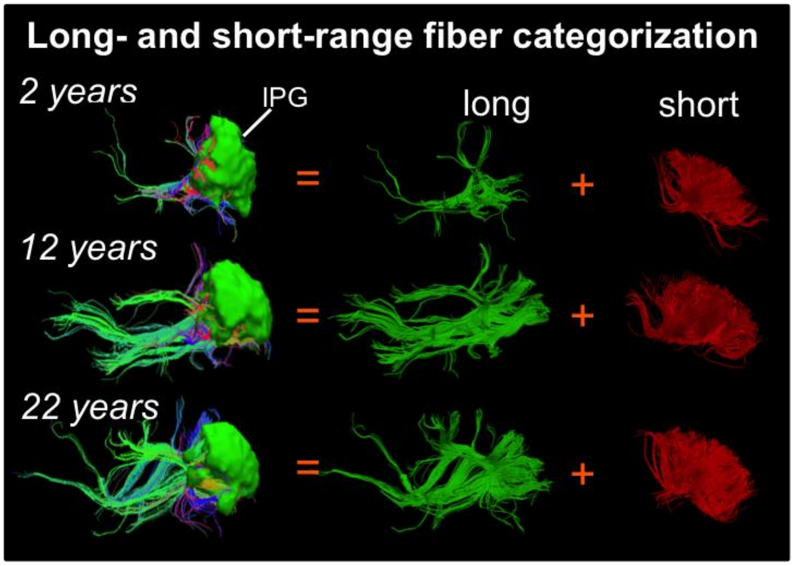

Figure 4.3: Long-, short-range association fiber categorization from a representative gyrus (inferior parietal gyrus, IPG) from 3 typical developing subjects at 2, 12 and 22 years of age.

<u>Whole brain and regional NSAF developmental trend lines:</u> Figure 4.4 demonstrates the developmental curve of whole brain NSAF (fitted with quadratic model) and regional NSAF (fitted with cubic model). Whole brain NSAF decreases initially from 2 to around 16 years of age, followed by an increase from 16 to 25 years of age as seen in Figure 4.4a. In addition, we examined the developmental curves of regional NSAF in three representative functional regions of human brain: S1, V1 and prefrontal cortex (Figure 4.4b-4.4d). Similar to whole brain NSAF, the developmental curves of regional NSAF from all three functional regions in Figure 4.4b-4.4d show an initial decrease followed by a later increase. The developmental curves also suggested spatiotemperally heterogeneous NSAF dynamics. Specifically, the NSAF reaches its lowest value at different ages across these functional regions. The prefrontal cortex drops to its lowest

NSAF (~17 years) later than S1 (~9 years) and V1 (~14 years), suggesting later maturation of higher-order functional regions than primary sensorimotor regions.

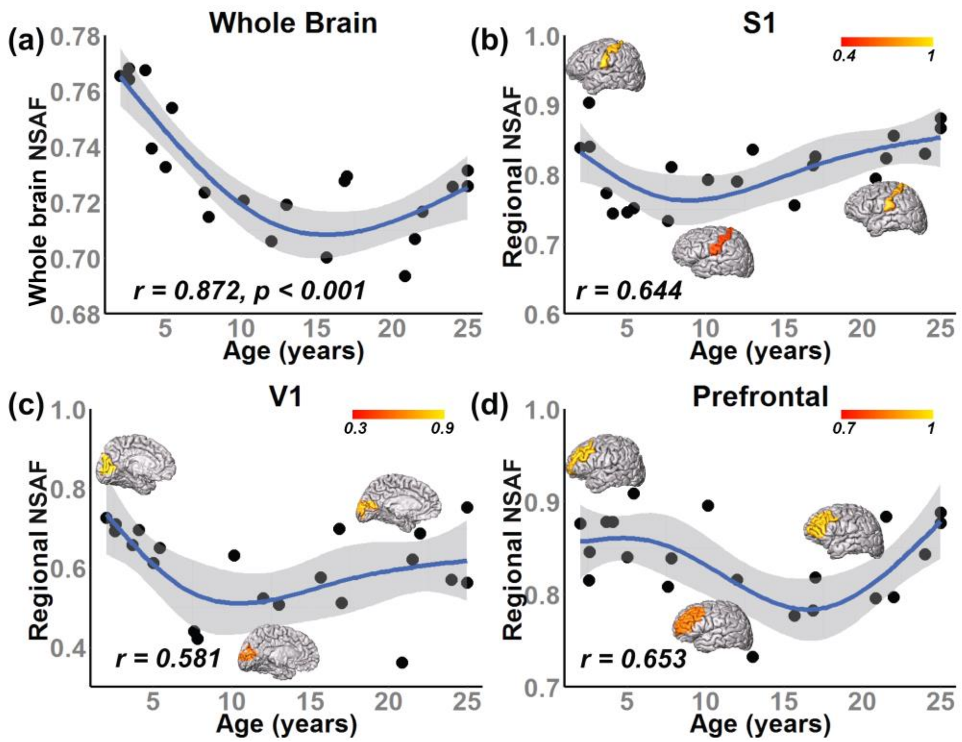

Figure 4.4: Developmental curve of whole brain NSAF fitted with quadratic model (a) and regional NSAF fitted with cubic model from three representative regions: primary somatosensory cortex (S1) (b), visual cortex (V1) (c) and prefrontal cortex (d), respectively. Each black diamond in the scatter plot represents the NSAF from one subject. Regional NSAF displayed on a three-dimensional reconstructed brain from 3 typical developing subjects at 2, 12 and 22 years of age were shown in panels (b-d).

4.3.2 Study 2: SAFs underlie brain network reconfiguration and the sensitivity of NSAF in typically and atypically developing children

<u>SAFs underlie brain network reconfiguration in typically and atypically developing children:</u> Figure 4.5 demonstrates the developmental curve of whole brain fiber numbers of SAF and LAF as well as whole brain NSAF in ASD and TD groups. Absolute fiber numbers of whole brain SAF and LAF significantly increase with age from 2 to 7 years in both groups ($p < 0.05$, Figure 4.5a-4.5b). All subjects’ whole brain NSAF values are larger than 0.5, indicating the number of SAF is more than half of the whole brain

cortico-cortical fiber number. Whereas the whole brain NSAF value significantly decreased from 2-7 years of age in the TD group (p=0.018), the whole brain NSAF value in ASD showed no association with age (p=0.48, Figure 4.5c).

Similarly, whereas a significant negative correlation (p=0.03) was observed between whole brain NSAF and global efficiency in the TD group, no correlation was found in the ASD group (p=0.78), shown in Figure 4.6.

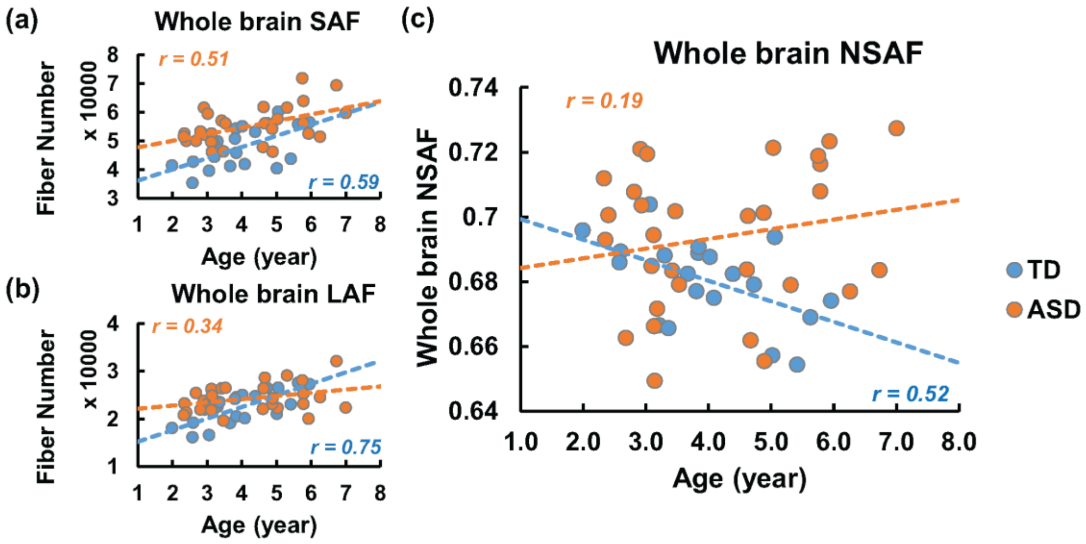

Figure 4.5: Developmental curve of whole brain SAF fiber number (a), LAF fiber number (b) and whole brain NSAF (c) in both ASD and TD groups. Each circle in the scatter plots represents one child with ASD (orange) or TD (blue). The dashed lines (blue for TD and orange for ASD) were linearly fitted from these measurements. R values (blue for TD and orange for ASD) are correlation coefficients of measurements and age.

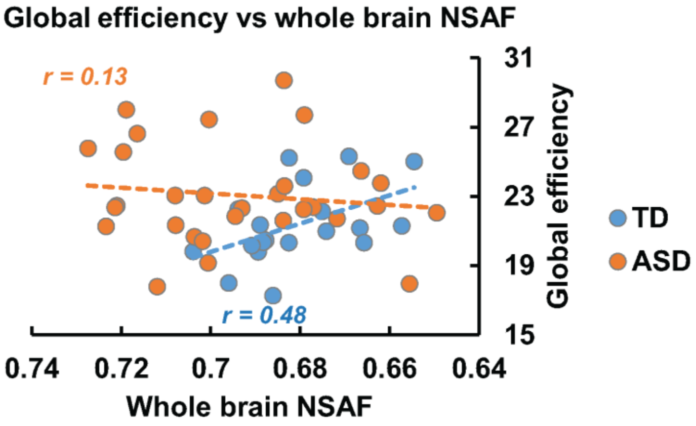

Figure 4.6: Relationship between whole brain NSAF and global network efficiency in both ASD and TD groups. Each circle in the scatter plots represents one child with ASD (orange) or TD (blue). The dashed lines (blue for TD and orange for ASD) were linearly fitted from these measurements. R values (blue for TD and orange for ASD) are correlation coefficients.

Atypical maturation of SAFs connecting higer-order brain regions in children with ASD aged 2-7 years: Figure 4.7 demonstrates the developmental curves of regional NSAF from two representative higher-order functional regions in TD and ASD. The three-dimensionally reconstructed LAF (green) and SAF (red) connected to the cortical region are also shown on the top of Fig.2. In higher-order functional regions, in the TD group the NSAF value decreased significantly from 2 to 7 years in both prefrontal cortex (p=0.05, Fig.2a) and DMN-hub (p=0.04, Fig.2b). In contrasts, in ASD the NSAF values from these two regions were not significantly associated with age (p>0.05, Fig.2), indicating atypical maturation of short-range connectivity. On the other hand, in the TD group the NSAF from primary sensory regions such as V1 and S1 were not significantly associated with age (p>0.05). Similarly, in ASD, associations between regional NSAF of S1 or V1 and age were also not observed.

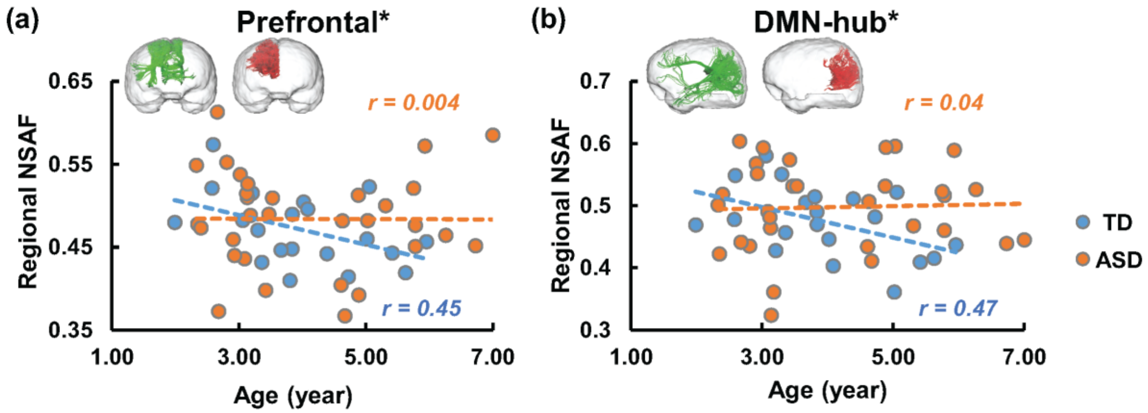

Figure 4.7: Developmental curve of regional NSAF from two higher-order functional regions: prefrontal cortex (a) and default-mode network hub (b). Each circle in the scatter plot represents the NSAF from one child with TD (blue) or ASD (orange). The dashed lines (blue for TD and orange for ASD) were linearly fitted from regional NSAF value. R values (blue for TD and orange for ASD) are correlation coefficients of regional NSAF and age.

4.4 Discussion

In this study, we proposed a metric called NSAF, defined as the ratio of SAF in the total cortico-cortical connectivity fibers traced from a given cortical gyrus (regional NSAF) or entire brain (whole brain NSAF), to quantify the SAF or short-range cortico-cortical connection during brain development. The normative developmental patterns of whole brain and regional NSAF were demonstrated from early childhood to young adulthood (from 2 to 25 years). Specifically, the NSAF values declined first, followed by an increase in both whole brain and regional levels. Heterogeneous developmental curves of regional NSAF were observed across three functional regions, including S1, V1 and prefrontal cortex (Figure 4.4b-4.4d), by dropping to their lowest NSAF values at different time points. In addition, the initiate decreasing of whole brain NSAF in young children with TD (2-7 years) was highly associated with the increases of global efficiency, a structural network property based on graph theory, while no such association was found in ASD. Atypical maturation of SAF, reflecting by atypical developmental pattern of regional NSAF, was also observed in higher-order brain regions (prefrontal and DMN-hub) in children with ASD. Taken together, SAF play an important role in the brain network reconfiguration and the spatiotemporal sensitivity of NSAF makes it a potential biomarker to characterize normal brain development and detect neuropathology like ASD.

4.4.1 Regional difference of NSAF normative developmental trajectories from early childhood to adulthood

From early childhood to adulthood, synaptogenesis and synaptic pruning continuously reshape the structural architecture and neural connection in developmental human brain (Cowan et al., 1984; Innocenti, 1981; LaMantia and Rakic, 1990 and 1994). Using histological approach, prior studies have observed synaptic overproduction in infancy, persistence of high levels of synaptic density to adolescence, followed by a decrease after adolescence (e.g. Huttenlocher et al., 1982, Huttenlocher, 1990, Petanjek et al., 2011). In addition, distinct regional variations in the timelines of synaptogenesis and synaptic elimination during human brain development were reported. Specifically, these progressive and regressive events have been found beginning earlier in primary sensorimotor regions and later in the prefrontal cortex (e.g. Huttenlocher et al., 1982, Huttenlocher, 1990, Petanjek et al., 2011). In the present study, a similar pattern has been observed in our regional NSAF, with somatosensory cortex reach its lowest value earlier than visual cortex and prefrontal cortex (Figure 4.4), suggesting its relevance with these cellular or molecular processing in developmental human brain. The proposed NSAF may reflect the balance between strengthening (including myelination) of certain fibers and pruning of others.

4.4.2 Whole brain NSAF decreases highly correlates with global network efficiency increases

Information processing in the human brain arises from both interactions between adjacent brain areas (short-range connections) and from distant projections (long-range connections) that form distributed systems. SAFs comprise the majority of the cortico-cortical WM fibers in the human brain (Schüz and Braitenberg, 2002) and are thought to work as part of the cortico-cortical networks to execute associative brain functions (Arnold, 1838; Meynert, 1872). During the childhood, absolute brain size increases in conjunction with a disproportionate enlargement of cortical surface area were observed in previous studies (e.g. Kaas, 2006; Rakic, 2009; Toro et al., 2008). This expansion comes with a cost to information processing efficiency (Kaas, 2006). Structural network studies of developing brains (e.g. Dennis et al., 2013; Hagmann et al., 2010; Huang et al., 2015; Yap et al., 2011) found network efficiency significantly increase with age and also suggested that emergence of the maturing brain networks are associated with both enhancement of some WM fibers and synaptic pruning of other fibers. In TD from our study, whole brain NSAF was observed to decrease during early childhood, and significantly correlated with increase in network efficiency (Figure 4.6). Specifically, in older TD children, lower whole brain NSAF was associated with less SAFs, showing higher global network efficiency in these children. However, an atypical whole brain NSAF trajectory was found in the children aged 2-7 years with ASD, and no significant association was found between NSAF and network efficiency in these children. These findings converge to suggest that the balance of SAF (short-range connection) and LAF (long-range connection) is important for efficient cortical processing and such balance in ASD might be disrupted.

4.4.3 Atypical maturation of SAFs connecting higher-order brain regions in children with ASD aged 2-7 years

Functional over-connectivity within local networks has been observed in ASD in previous studies with different imaging modalities (e.g. Ghanbari et al., 2015; Keown et al., 2013; Muria et al., 2007; Supekar et al., 2013; Schmitz et al., 2006;). For example, increased activation in ASD in the left inferior and obital frontal gyrus during a motor inhibition task was found with functional MRI (Schimitz et al., 2006). Using MEG, ASD shown increase of short-range connectivity in the frontal lobe in the delta band (Ghanbari et al., 2015). Increased coherences in the theta (3-6 Hz) frequency band, particularly marked in short-distance frontal and left temporal electrode pairs was observed in ASD with EEG (Murias et al., 2007). However, there is less evidence for local or short-range over-connectivity were found with structural or diffusion MRI (see review: Vissers et al., 2012; Wass, 2011 for details).

In our study, gradual decreases of NSAF in higher-order brain regions were found in normal brain development and the NSAF metric revealed that the age-dependent trajectories of short-range connections in children with ASD are altered in higher-order but not in primary sensory brain regions (Figure 4.7). The non-uniform alterations indicate that higher-order brain regions are of specific interest in children with ASD aged 2-7 years. The findings may also offer structural basis for the functional “over-connectivity” described in ASD (e.g. Courchesne et al., 2007; Keown et al., 2013; Rudie et al., 2013; Supekar et al., 2013; Vissers et al., 2012; Wass, 2011). In addition, our previous work with the same dataset found atypical age-dependent changes of FA and radial diffusivity (RD) widely and heterogeneously distributed in DWM regions or long-range WM connectivity of children with ASD (see Chapter 3 for detail). Taken together, atypical trajectories of both SAF (short-range connection) in superficial WM and WM integrity in deep WM were found in young children with ASD, suggesting age-related change may play an important role of both short-range and long-rang connection in individual with ASD.

4.5 Limitations of current study and future perspectives

Several limitations should be noted. First, relatively small sample sizes are reported. Second, all data presented are cross-sectional and further description of developmental trajectories requires a longitudinal dataset. Third, a deterministic approach of dMRI-based tractography was used to trace the whole brain association fibers. It is known the dMRI-based tractography is oversimplified compared to the underlying neuroanatomy. However, as long as it provides reproducible results, it is an important tool to delineate the macroscopic architecture of the human brain WM and to investigate its status under both normal and pathological conditions (Zhang et al., 2010).

Acquisition and analysis of dMRI data from more healthy subjects are under way to better characterize the normative developmental pattern of NSAF. The analysis of the relationship between NSAF and regional network properties is also interesting to explore with both typical and atypical developmental children.

4.6 Conclusion

The proposed NSAF metric, based on dMRI tractography, reflects the balance between SAF and LAF across brain regions. The NSAF is spatiotemporally heterogeneous, decreasing in early childhood and increasing later with lowest NSAF reached at various ages among cortical gyri. The decrease of whole brain NSAF was highly correlated with global network efficiency increase in young children with TD but not ASD, indicating the important role of balance between SAF and LAF during the brain development. Altered maturation of short-range connection in higher-order brain regions were found in children with ASD, suggesting the NSAF could be a potential biomarker for delineation normal brain development and diagnosis of several mental disorders. In addition, NSAF can be characterized both regionally and across the entire brain, yielding regional and whole brain measurements. With its noninvasive nature, the NSAF can be readily derived from routine dMRI and T1 weighted images typically acquired in less than 10 minutes.

Chapter 5

Conclusion and Outlook

As mentioned in previous chapters, both diffusion MRI (dMRI) and perfusion MRI (pMRI) have been wildly used in studying human brain. This thesis deals with applying these advanced neuroimaging methods to develop new analysis techniques to delineate the typically and atypically development of human brain during early stages, namely from birth to early childhood.

ASL has become a reliable way too to study the regional CBF in the brain from infants to adults. Since it is noninvasive and does not need invasive tracers (compared to PET), it is a viable technique to measure the CBF in preterm brain. However, studies using ASL in preterm brains are relative rare since it is challenging due to the extremely slow blood velocity. There has been no study that characterized the regional CBF dynamics of brain development, which covered a comprehensive age range (32 PMW to 45 PMW) during the whole 3rd trimester. In the first part of thesis work (Chapter 2), a 3D GRASE pCASL sequence has been optimized to adapt to the extremely slow blood flow in neonate population and CBF measurements obtained from the optimized pCASL protocol were of moderate-to-high reproducibility. Global CBF (averaged whole brain CBF) was found to double its amount during the 3rd trimester with heterogeneous CBF increasing rate across brain regions in healthy neonates. Specifically, frontal CBF increases faster than that in the occipital region from 32 to 45 PMW. These CBF increases were highly associated with the microstructural changes (FA decreases) in the frontal brain regions. The availability of such optimized pCASL protocol adapted to slow blood flow in neonate population could be used to investigate the relationship among structure, function and metabolism in the neonate brain under both normal and pathological conditions (e.g. hypoxic-ischemic encephalopathy, congenital heart disease).

Although atypical age-dependent changes of deep white matter (WM) microstructure or long-range structural connection play a central role in abnormal brain maturation of children with autism spectrum disorder (ASD) with dMRI, their early manifestations have not been systematically characterized. In the second part of the thesis (Chapter 3), we surveyed the entire brain core WM to detect differences in WM microstructural development between 31 children with ASD and 19 age-matched children with typical development (TD), between ages of 2-7 years, using fractional anisotropy (FA) and radial diffusivity (RD) from diffusion tensor imaging (DTI). Exclusively, unidirectional FA increases and RD decreases in widespread WM tracts in children with ASD before age of 4 years, with bi-directional changes found for children with ASD between ages of 2-7 years. Compared to progressive development that raised FA and lowered RD during 2-7 years in the TD group, flattened curves of WM maturation were found in multiple major long-range WM tracts of all five tract groups, particularly associational and limbic tracts, in the ASD group with trend lines of ASD and TD crossed around 4 years. We found atypical age-dependent changes of FA and RD widely and heterogeneously distributed in long-range WM fibers of children with ASD. The early higher WM microstructural integrity before 4 years reflects abnormal neural patterning, connectivity, and pruning that may contribute to aberrant behavioral and cognitive development. In the future, longitudinal study that monitors the WM development in young children (age range from around 2 to 7 years) with ASD will be helpful to provide more evidences about the altered developmental trajectories in ASD.

To further study the WM in early brain development (unlike the deep WM or long-range structural connection examined in Chapter 3), a novel index named normal short-range association fibers (NSAF) was proposed to examine the superficial WM or short-range connection development in the third part of this thesis work (Chapter 4). This NSAF, defined as the ratio of the number of short-range association fibers (SAF) to the number of all cortico-cortical fibers traced from a given gyrus with DTI tracktography, was first measured in 21 healthy subject aged from young childhood to adulthood (2 to 25 years). The NSAF showed spatiotemporal sensitivity across brain regions in typical brain development, with NSAF declined to its lowest value earlier in primary somatosensory cortex (~9 years), primary visual cortex (~14 years) and late in prefrontal cortex (~17 years). Explored the relationship between SAFs and brain network reconfiguration and the sensitivity of NSAF in typical and atypical developmental human brain, NSAF was measured in 20 children with TD and 31 children with ASD (2-7 years). In TD, the whole brain NSAF decrease was highly associated with global network efficiency from graph theory analysis. However, such correlation was not found in ASD children. In addition, regional NSAF values in prefrontal cortex and default-mode network hub decreased significantly in children with TD, but not ASD, indicating the atypical mutation of short-range connection in ASD in high-order functional regions. Taken together, the spatiotemporal properties, sensitivities of proposed NSAF make it a potential biomarker for delineating short-range connectivity in typical and atypical developmental (e.g. ASD) human brain. This short-range connection hasn't been well documented in human brain yet. In future studies, it would be interesting to see how this short-range structural connection (e.g. NSAF calculated from dMRI) is coupled with short-range functional connection, which could be obtained from functional MRI. Furthermore, with regional CBF information obtained from ASL, the studies can reveal the physiological basis for structural and functional short-range connection development in human brain.

Appendix A

Linear and nonlinear fitting of age-dependent FA and RD curves

In this appendix, comparisons between linear and nonlinear fitting of age-dependent FA and RD curves were performed. Linear and nonlinear (logarithmic) fitting were conducted between FA or RD measurements and age and F-test was used to find out the best fitting curve. FA or RD measurements were averaged from the clusters identified from GLM described above. The following equation was fit, $y=f(t) + b + \varepsilon$, where $f(t)$ was linear or logarithmic function, y was FA or RD measurement from children with ASD or TD, t was age and ε was an error term. F-test was used to find the best fitting curve. We first tested if the measurement y was age dependent. If so, we further tested which of the following curves, linear and logarithmic, fitted the data best. Age-dependent curves of FA and RD measurements from the largest cluster of one representative tract in each of four tract groups were adopted for selection between linear and nonlinear fitting. The resultant linear (solid line) and logarithmic (dashed line) fitting curves with FA or RD measurements from children with TD (blue) and ASD (red) are shown in Appendix A Figure. Table 1A and 1B list the statistics of comparing linear and nonlinear (logarithmic) fitting with FA and RD measurements, respectively. No statistical difference between linear and logarithmic fitting was found for all the measurements in representative WM tracts.

Appendix A Table 1: Comparison of linear and logarithmic fitting with age-dependent FA (A) and RD (B) measurements from the largest cluster of representative tracts.

Table 1A:

Tracts	Age dependence		F-test between linear and logarithmic				Best fitting curve for either ASD or TD group
			F value		p value		
	TD	ASD	TD	ASD	TD	ASD	
BCC	**	NS	0.9790	--	NS	--	linear/logarithmic
FX-L	***	NS	0.9792	--	NS	--	linear/logarithmic
ALIC-L	**	NS	0.8565	--	NS	--	linear/logarithmic
SFO-R	***	NS	0.9700	--	NS	--	linear/logarithmic

*Statistical significance $p < 0.05$, $p < 0.01$, and $p < 0.0001$ are indicated by bold *, **, and ***, respectively. NS: not significant.*

Table 1B:

Tracts	Age dependence		F-test between linear and logarithmic				Best fitting curve for either ASD or TD group
			F value		p value		
	TD	ASD	TD	ASD	TD	ASD	
BCC	***	NS	1.0113	--	NS	--	linear/logarithmic
FX-L	***	NS	0.8761	--	NS	--	linear/logarithmic
ALIC-L	***	*	0.9960	0.9800	NS	NS	linear/logarithmic
SFO-R	***	***	0.9387	0.9203	NS	NS	linear/logarithmic

*Statistical significance p < 0.05, p < 0.01, and p < 0.0001 are indicated by bold *, **, and ***, respectively. NS: not significant.*

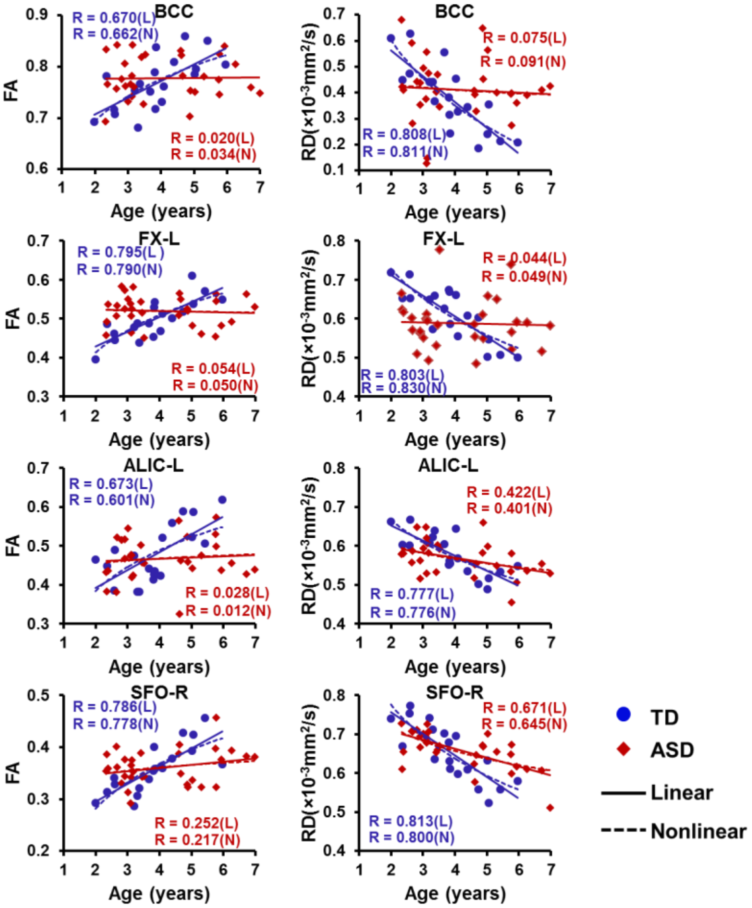

Appendix A Figure: The linear (solid line) and nonlinear (dashed line) fitting of age-dependent changes of FA and RD measurement from the largest cluster in representative tracts, namely BCC (commissural tract), FX-L (limbic tract), ALIC-L (projection tract), SFO-R (association tract) of children with ASD (red diamonds and red lines) and TD (blue circles and blue lines). One red diamond point or blue circle point in each scatter plot indicates FA or RD measurement from one child with ASD or TD, respectively. L and N after R values indicate linear and nonlinear (logarithmic) fitting, respectively.

Appendix B

Correlation between clinical score and FA or RD in subgroup of children with ASD

In this appendix, the relationship between clinical score and DTI-derived measurements has been explored. To test if there is any relationship of higher WM microstructural integrity and poorer clinical behavior or symptom during the overgrowth period of less than 4 years of age, we correlated averaged FA or RD measurement of each WM tract to each of the following scores, Autism Diagnostic Interview (ADI), Childhood Autism Rating Scale (CARS) and Clancy Autism Behavior Scale (CABS). Interestingly, higher FA measurements of CGH-R and lower RD measurements of CGH-L, both indicating higher microstructural integrity of these tracts, are associated to higher CABS (Appendix B Figure), suggesting enhanced WM microstructural development before less than 4 years is associated with poorer clinical ASD symptoms.

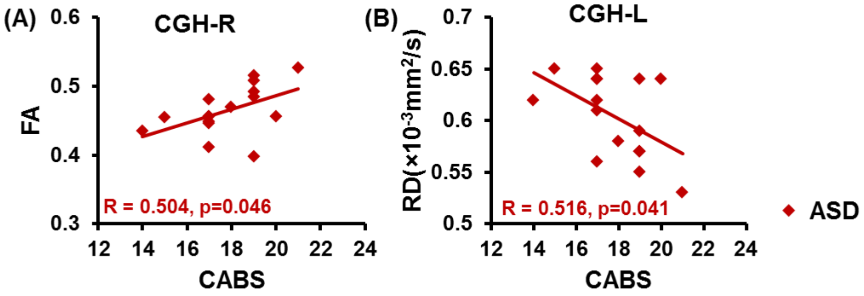

Appendix B Figure: Significant correlation of FA of CGH-R (A) and RD of CGH-L (B) to CABS. Each red diamond represents measurement from one child with ASD in age of 2-to-4 years. Linear trend line is also shown.

Appendix C

List of percentage values of voxels with significant age-group interactions within each white matter tract or tract group

In this appendix, the percentage values of affected voxels within each WM tract and each tract group in bar plots in Figure 3.5-3.6 are listed in following table.

Tract	Affected percentage values of atypical age-dependent FA changes	Affected percentage values of atypical age-dependent RD changes
Commissural tract group		
Entire tract group	2.3%	0.03%
GCC	1.7%	0
BCC	3.9%	0.03%
SCC	0.8%	0.05%
Tapetum-R	0	0
Tapetum-L	0	0
Limbic system tract group		
Entire tract group	7.5%	2.1%
BFX	0.7%	0
CGC-R	0	0
CGC-L	3.7%	0
CGH-R	0	0
CGH-L	0	0
FX-R	14.1%	0
FX-L	26.5%	10.5%
Projection tract group		
Entire tract group	1.3%	1.2%
CST-R	0	0
CST-L	0	0
ALIC-R	0.7%	1.2%
ALIC-L	5.0%	3.8%
PLIC-R	0	0
PLIC-L	0	0
RLIC-R	0.1%	0
RLIC-L	0.6%	0
ACR-R	1.8%	3.8%
ACR-L	0.5%	1.4%
SCR-R	0.5%	0.5%
SCR-L	3.9%	3.3%
PCR-R	3.7%	0
PCR-L	0	1.6%
PTR-R	2.3%	1.7%
PTR-L	0	0
Association tract group		
Entire tract group	5.8%	2.9%
SS-R	1.5%	0
SS-L	7.2%	2.5%
EC-R	7%	5.1%
EC-L	18%	6.1%

SLF-R	0.8%	0.1%
SLF-L	0.05%	2.1%
SFO-R	28.4%	13.6%
SFO-L	0	1.4%
UNC-R	13.5%	0
UNC-L	19.2%	14.9%
Brainstem tract group		
Entire tract group	0.2%	0.29%
MCP	0	0.18%
ML-R	0	0
ML-L	0	0
ICP-R	0	0
ICP-L	0	0
SCP-R	0	0
SCP-L	0	0
CP-R	0.44%	1.3%
CP-L	1.8%	0

Reference

Alexander AL, Lee JE, Lazar M, Boudos R, DuBray MB, Oakes TR, Miller JN, Lu J, Jeong EK, McMahon WM, Bigler ED, Lainhart JE. 2007. Diffusion tensor imaging of the corpus callosum in Autism. NeuroImage. 34:61-73.

Allen G. 2005. The cerebellum in autism. Clin Neuropsychiatry. 2(6):321-337.

Alsop DC, Detre JA, Golay X, Günther M, Hendrikse J, Hernandez-Garcia L, Lu H, MacIntosh BJ, Parkes LM, Smits M, Osch MJ. 2015. Recommended implementation of arterial spin-labeled perfusion MRI for clinical applications: A consensus of the ISMRM perfusion study group and the European consortium for ASL in dementia. Magn Reson Med. 73(1):102-116.

Altman DI, Powers WJ, Perlman JM, Herscovitch P, Volpe SL, Volpe JJ. 1988. Cerebral blood flow requirement for brain viability in newborn infants is lower than in adults. Ann Neurol. 24:218-226.

Amaral DG, Schumann CM, Nordahl CW. 2008. Neuroanatomy of autism. Trends Neurosci. 31:137-145.

APA. 2013. Diagnostic and Statistical Manual of Mental Disorders, 5th ed. Arlington, VA: American Psychiatric Association.

Attwell D, Laughlin SB. 2001. An energy budget for signaling in the grey matter of the brain. J Cereb Blood Flow Metab. 21(10):1133-1145.

Arnold F. 1838. Untersuchungen im Gebiete der Anatomie und Physiologie: Mit Besonderer Hinsicht auf Seine Anatomischen Tafeln. Zurich: S. Hohr.

Aslan S, Xu F, Wang PL, Uh J, Yezhuvath US, van Osch M, Lu H. 2010. Estimation of labeling efficiency in pseudocontinuous arterial spin labeling. Magn Reson Med. 63:765-771.

Baenziger O, Jaggi JL, Mueller AC, Morales CG, Lipp AE, Duc G, Bucher HU. 1995. Regional differences of cerebral blood flow in the preterm infant. Eur J Pediatr. 154:919-924.

Baird G, Cass H, Slonims V. 2003. Diagnosis of autism. Bmj 327:488-493.

Bakker CJ, Hoogeveen RM, Viergever MA. 1999. Construction of a protocol for measuring blood flow by two-dimensional phase-contrast MRA. J Magn Reson Imaging. 9:119-127.

Ball G, Srinivasan L, Aljabar P, Counsell SJ, Durighel G, Hajnal JV, Rutherford MA, Edwards AD. 2013. Development of cortical microstructure in the preterm human brain. Proc Natl Acad Sci USA. 110:9541-9546.

Barnea-Goraly N, Menon V, Eckert M, Tamm L, Bammer R, Karchemskiy A, Dant CC, Reiss AL. 2005. White matter development during childhood and adolescence: a cross-sectional diffusion tensor imaging study. Cereb Cortex. 15(12):1848-1854.

Bashat DB, Kronfeld-Duenias V, Zachor DA, Ekstein PM, Hendler T, Tarrasch R, Even A, Levy Y, Sira LB. 2007. Accelerated maturation of white matter in young children with autism: a high b value DWI study. Neuroimage. 37(1):40-47.

Basser PJ, Mattiello J, LeBihan D. 1994. MR diffusion tensor spectroscopy and imaging. Biophys J. 66:259-267.

Basser PJ, Pajevic S, Pierpaoli C, Duda J, Aldroubi A. 2000. In vivo fiber tractography using DT-MRI data. Magn Reson Med. 44(4):625-632.

Bauman M, Kemper T. 1987. Limbic involvement in a second case of early infantile autism. Neurology. 37:147.

Beaulieu C. 2002. The basis of anisotropic water diffusion in the nervous system-a technical review. NMR Biomed. 15(7-8):435-455.

Benes FM, Turtle M, Khan Y, Farol P. 1994. Myelination of a key relay zone in the hippocampal formation occurs in the human brain during childhood, adolescence, and adulthood. Arch Gen Psychiatry. 51(6):477-484.

Behrens TE, Berg HJ, Jbabdi S, Rushworth MF, Woolrich MW. 2007. Probabilistic diffusion tractography with multiple fibre orientations: What can we gain? Neuroimage. 34(1):144-155.

Blencowe H, Cousens S, Oestergaard MZ, Chou D, Moller AB, Narwal R, Adler A, Garcia CV, Rohde S, Say L, Lawn JE. 2012. National, regional, and worldwide estimates of preterm birth rates in the year 2010 with time trends since 1990 for selected countries: a systematic analysis and implications. The Lancet. 379(9832):2162-2172.

Borch K, Greisen G. 1998. Blood flow distribution in the normal human preterm brain. Pediatr Res. 43:28-33.

Bourgeois JP, Jastreboff PJ, Rakic P. 1989. Synaptogenesis in visual cortex of normal and preterm monkeys: evidence for intrinsic regulation of synaptic overproduction. Proc Natl Acad Sci USA. 86:4297-4301.

Bystron I, Blakemore C, Rakic P. 2008. Development of the human cerebral cortex: Boulder Committee revisited. Nat Rev Neurosci. 9:110-122.

Casey BJ, Tottenham N, Liston C, Durston S. 2005. Imaging the developing brain: what have we learned about cognitive development? Trends Cogn Sci. 9(3):104-110.

Catani M, de Schotten MT. 2008. A diffusion tensor imaging tractography atlas for virtual in vivo dissections. Cortex. 44(8):1105-1132.

Chalela JA, Alsop DC, Gonzalez-Atavales JB, Maldjian JA, Kasner SE, Detre JA, 2000. Magnetic resonance perfusion imaging in acute ischemic stroke using continuous arterial spin labeling. Stroke. 31:680-687.

Cheng Y, Chou KH, Chen IY, Fan YT, Decety J, Lin CP. 2010. Atypical development of white matter microstructure in adolescents with autism spectrum disorders. NeuroImage. 50:873-882.

Chugani HT. 1998. A critical period of brain development: studies of cerebral glucose utilization with PET. Preventive medicine. 27(2): 184-188.

Chugani HT, Phelps ME. 1986. Maturational changes in cerebral function in infants determined by 18FDG positron emission tomography. Science. 231:840-843.

Clancy H, Dugdale A, Rendle-Short J. 1969. The diagnosis of infantile autism. Dev Med Child Neurol. 11:432-42.

Conklin J, Winter JD, Thompson RT, Gelman N. 2008. High-contrast 3D neonate brain imaging with combined T1-and T2-weighted MPRAGE. Magn Reson Med. 59(5): 1190-1196.

Courchesne E, Carper R, Akshoomoff N. 2003. Evidence of brain overgrowth in the first year of life in autism. JAMA. 290(3):337-344.

Courchesne E, Pierce K. 2005. Why the frontal cortex in autism might be talking only to itself: local over-connectivity but long-distance disconnection. Curr Opin Neurobiol. 15(2):225-230.

Courchesne E, Pierce K, Schumann CM, Redcay E, Buckwalter JA, Kennedy DP, Morgan J. 2007. Mapping early brain development in autism. Neuron. 56(2):399-413.

Courchesne E, Karns CM, Davis HR, Ziccardi R, Carper RA, Tigue ZD, Chisum HJ, Moses P, Pierce K, Lord C, Lincoln AJ. 2001. Unusual brain growth patterns in early life in patients with autistic disorder an MRI study. Neurology. 57(2):245-254.

Courchesne E, Redcay E, Morgan JT, Kennedy DP. 2005. Autism at the beginning: microstructural and growth abnormalities underlying the cognitive and behavioral phenotype of autism. Dev Psychopathol. 17(03):577-597.

Cowan WM, Fawcett JW, O'Leary DD, Stanfield BB. 1984. Regressive events in neurogenesis. Science. 225(4668):1258-1265.

Dai W, Garcia D, de Bazelaire C, Alsop DC. 2008. Continuous flow-driven inversion for arterial spin labeling using pulsed radio frequency and gradient fields. Magn Reson Med. 60:1488-1497.

Daniels AM, Mandell DS. 2013. Explaining differences in age at autism spectrum disorder diagnosis: A critical review. Autism. 18:583-597

Dawson G, Toth K, Abbott R, Osterling J, Munson J, Estes A, Liaw J. 2004. Early social attention impairments in autism: social orienting, joint attention, and attention to distress. Dev Psychol. 40:271-283.

delpolyi AR, Mukherjee P, Gill K, Henry RG, Partridge SC, Veeraraghavan S, Jin H, Lu Y, Miller SP, Ferriero DM, Vigneron DB. and Barkovich AJ. 2005. Comparing microstructural and macrostructural development of the cerebral cortex in premature newborns: diffusion tensor imaging versus cortical gyration. Neuroimage. 27(3): 579-586.

Dennis EL, Jahanshad N, McMahon KL, de Zubicaray GI, Martin NG, Hickie IB, Toga AW, Wright MJ, Thompson PM. 2013 Development of brain structural connectivity between ages 12 and 30: a 4-Tesla diffusion imaging study in 439 adolescents and adults. Neuroimage. 64:671-684.

Detre JA, Alsop DC. 1999. Perfusion magnetic resonance imaging with continuous arterial spin labeling: methods and clinical applications in the central nervous system. Eur J Radiol. 30:115-124.

Detre JA, Wang J, Wang Z, Rao H. 2009. Arterial spin-labeled perfusion MRI in basic and clinical neuroscience. Curr Opin Neurol. 22(4):348-355.

Desikan RS, Ségonne F, Fischl B, Quinn BT, Dickerson BC, Blacker D, Buckner RL, Dale AM, Maguire RP, Hyman BT, Albert MS. 2006. An automated labeling system for subdividing the human cerebral cortex on MRI scans into gyral based regions of interest. Neuroimage. 31(3):968-980.

De Vis JB, Hendrikse J, Petersen ET, de Vries LS, van Bel F, Alderliesten T, Negro S, Groenendaal F, Benders MJ. 2015. Arterial spin-labelling perfusion MRI and outcome in neonates with hypoxic-ischemic encephalopathy. Eur Radiol. 25:113-121.

De Vis JB, Petersen ET, Alderliesten T, Groenendaal F, de Vries LS, van Bel F, Benders MJ, Hendrikse J. 2014. Non-invasive MRI measurements of venous oxygenation, oxygen extraction fraction and oxygen consumption in neonates. Neuroimage 95:185-192.

De Vis JB, Petersen ET, de Vries LS, Groenendaal F, Kersbergen KJ, Alderliesten T, Hendrikse J, Benders MJ. 2013. Regional changes in brain perfusion during brain maturation measured non-invasively with Arterial Spin Labeling MRI in neonates. Eur J Radiol. 82:538-543.

Dittmer DS. 1961. Blood and other body fluids. Washington, DC: Federation of American Societies for Experimental Biology. pp 15, 19, 326, 327.

du Plessis AJ. 2009. Cerebral blood flow and metabolism in the developing fetus. Clin Perinatol. 36:531-548.

Edwards AD, Wyatt JS, Richardson C, Delpy DT, Cope M, Reynolds EO. 1988. Cotside measurement of cerebral blood flow in ill newborn infants by near infrared spectroscopy. Lancet 2:770-771.

Engle WA, American Academy of Pediatrics Committee on Fetus and Newborn. 2004. Age terminology during the perintal period. Pediatrics. 114:1362-1364.

Evans AJ, Iwai F, Grist TA, Sostman HD, Hedlund LW, Spritzer CE, Negro-Vilar ROSA, Beam CA and Pelc NJ. 1993. Magnetic Resonance Imaging of Blood Flow with a Phase Subtraction Technique: In Vitro and In Vivo Validation. Investigative radiology. 28(2):109-115.

Ghanbari Y, Bloy L, Edgar JC, Blaskey L, Verma R, Roberts TP. 2015. Joint analysis of band-specific functional connectivity and signal complexity in autism. J Autism Dev Disord. 45(2):444-460.

Gogtay N, Giedd JN, Lusk L, Hayashi KM, Greenstein D, Vaituzis AC, Nugent TF, Herman DH, Clasen LS, Toga AW, Rapoport JL. 2004. Dynamic mapping of human cortical development during childhood through early adulthood. Proc Natl Acad Sci USA. 101(21):8174-8179.

Gogtay N, Lu A, Leow AD, Klunder AD, Lee AD, Chavez A, Greenstein D, Giedd JN, Toga AW, Rapoport JL, Thompson PM. 2008. Three-dimensional brain growth abnormalities in childhood-onset schizophrenia visualized by using tensor-based morphometry. Proc Natl Acad Sci USA. 105(41):15979-15984.

Greisen G, Trojaborg W. 1987. Cerebral blood flow, PaCO2 changes, and visual evoked potentials in mechanically ventilated, preterm infants. Acta Paediatr. 76:394-400.

Hagmann P, Sporns O, Madan N, Cammoun L, Pienaar R, Wedeen VJ, Meuli R, Thiran JP, Grant PE. 2010. White matter maturation reshapes structural connectivity in the late developing human brain. Proc Natl Acad Sci USA. 107(44):19067-19072.

Haznedar MM, Buchsbaum MS, Wei TC, Hof PR, Cartwright C, Bienstock CA, Hollander E. 2000. Limbic circuitry in patients with autism spectrum disorders studied with positron emission tomography and magnetic resonance imaging. Am J Psychiatry. 157:1994-2001.

Hedman AM, van Haren NE, Schnack HG, Kahn RS, Pol H, Hilleke E. 2012. Human brain changes across the life span: a review of 56 longitudinal magnetic resonance imaging studies. Hum Brain Mapp. 33:1987-2002.

Herscovitch P, Raichle ME. 1985. What is the correct value for the brain-blood partition coefficient for water. J Cereb Blood Flow Metab. 5:65-69.

Huang H, Fan X, Weiner M, Martin-Cook K, Xiao G, Davis J, Devous M, Rosenberg R, Diaz-Arrastia R. 2012a. Distinctive disruption patterns of white matter tracts in Alzheimer's disease with full diffusion tensor characterization. Neurobiol Aging. 33:2029-2045.

Huang H, Gundapuneedi T, Rao U. 2012b. White matter disruptions in adolescents exposed to childhood maltreatment and vulnerability to psychopathology. Neuropsychopharmacology. 37:2693-2701.

Huang H, Jeon T, Sedmak G, Pletikos M, Vasung L, Xu X, Yarowsky P, Richards LJ, Kostovic I, Sestan N, Mori S. 2013. Coupling diffusion imaging with histological and gene expression analysis to examine the dynamics of cortical areas across the fetal period of human brain development. Cereb Cortex. 23:2620-2631.

Huang H, Shu N, Mishra V, Jeon T, Chalak L, Wang ZJ, Rollins N, Gong G, Cheng H, Peng Y, Dong Q. 2015. Development of human brain structural networks through infancy and childhood. Cereb Cortex. 25(5):1389-1404.

Huang H, Zhang J, Wakana S, Zhang W, Ren T, Richards LJ, Yarowsky P, Donohue P, Graham E, van Zijl PC, Mori S. 2006. White and gray matter development in human fetal, newborn and pediatric brains. Neuroimage. 33(1):27-38.

Hüppi PS, Warfield S, Kikinis R, Barnes PD, Zientara GP, Jolesz FA, Tsuji MK, Volpe JJ. 1998. Quantitative magnetic resonance imaging of brain development in premature and mature newborns. Ann Neurol. 43(2):224-235.

Huttenlocher PR. 1979. Synaptic density in human frontal cortex-developmental changes and effects of aging. Brain Res. 163(2):195-205.

Huttenlocher PR. 1974. Dendritic development in neocortex of children with mental defect and infantile spasms. Neurology. 24(3):203.

Huttenlocher PR. 1990. Morphometric study of human cerebral cortex development. Neuropsychologia. 28(6):517-527.

Huttenlocher PR, Dabholkar AS. 1997. Regional differences in synaptogenesis in human cerebral cortex. J Comp Neurol. 387:167-178.

Huttenlocher PR, de Courten C, Garey LJ, Van der Loos H. 1982. Synaptogenesis in human visual cortex—evidence for synapse elimination during normal development. Neurosci Lett. 33(3):247-252.

Inder TE, Warfield SK, Wang H, Hüppi PS, Volpe JJ. 2005. Abnormal cerebral structure is present at term in premature infants. Pediatrics. 115(2):286-294.

Innocenti GM. 1981. Growth and reshaping of axons in the establishment of visual callosal connections. Science. 212(4496):824-827.

Innocenti GM, Price DJ. 2005. Exuberance in the development of cortical networks. Nat Rev Neurosci. 6:955-965.

Jacobson M. 1991. Developmental neurobiology. New York: Plenum Press.

Jain V, Duda J, Avants B, Giannetta M, Xie SX, Roberts T, Detre JA, Hurt H, Wehrli FW, Wang DJ. 2012. Longitudinal reproducibility and accuracy of pseudo-continuous arterial spin-labeled perfusion MR imaging in typically developing children. Radiology. 263:527-536.

Jain V, Duda J, Avants B, Giannetta M, Xie SX, Roberts T, Detre JA, Hurt H, Wehrli FW, Wang DJ. 2012. Longitudinal reproducibility and accuracy of pseudo-continuous arterial spin–labeled perfusion MR imaging in typically developing children. Radiology. 263(2):527-536.

Jeon T, Mishra V, Ouyang M, Chen M, Huang H. 2015. Synchronous changes of cortical thickness and corresponding white matter microstructure during brain development accessed by diffusion MRI tractography from parcellated cortex. Front Neuroanat. 9.

Jiang H, van Zijl PC, Kim J, Pearlson GD, Mori S. 2006. DtiStudio: resource program for diffusion tensor computation and fiber bundle tracking. Comput Methods Programs Biomed. 81:106-116.

Jill B, Petersen ET, de Vries LS, Groenendaal F, Kersbergen KJ, Alderliesten T, Hendrikse J, Benders MJ. 2013. Regional changes in brain perfusion during brain maturation measured non-invasively with Arterial Spin Labeling MRI in neonates. Eur Radiol. 82(3):538-43.

Jones DK, Horsfield MA, Simmons A. 1999. Optimal strategies for measuring diffusion in anisotropic systems by magnetic resonance imaging. Magn Reson Med. 42:515-525.

Jopling J, Henry E, Wiedmeier SE and Christensen RD. 2009. Reference ranges for hematocrit and blood hemoglobin concentration during the neonatal period: data from a multihospital health care system.Pediatrics. 123(2): e333-e337.

Kaas JH. 2006. Evolution of the neocortex. Curr Biol. 16:R910-R914.

Kanner L. 1968. Autistic disturbances of affective contact. Acta Paedopsychiatr 35:100-136.

Kapellou O, Counsell SJ, Kennea N, Dyet L, Saeed N, Stark J, Maalouf E, Duggan P, Ajayi-Obe M, Hajnal J, Allsop JM. 2006. Abnormal cortical development after premature birth shown by altered allometric scaling of brain growth. PLoS Med. 3(8):e265.

Keown CL, Shih P, Nair A, Peterson N, Mulvey ME, Müller RA. 2013. Local functional overconnectivity in posterior brain regions is associated with symptom severity in autism spectrum disorders. Cell Rep. 5(3):567-572.

Kostovic I. 1990. Structural and histochemical reorganization of the human prefrontal cortex during perinatal and postnatal life. Prog Brain Res. 85:223-239; discussion 239-240.

Kostovic I, Jovanov-Milosevic N. 2006. The development of cerebral connections during the first 20-45 weeks' gestation. Semin Fetal Neonatal Med. 11:415-422.

Krug DA, Arick J, Almond P. 1980. Behavior checklist for identifying severely handicapped individuals with high levels of autistic behavior. J Child Psychol Psychiatry. 21:221-229.

Kumar A, Sundaram SK, Sivaswamy L, Behen ME, Makki MI, Ager J, Janisse J, Chugani HT, Chugani DC. 2010. Alterations in frontal lobe tracts and corpus callosum in young children with autism spectrum disorder. Cereb Cortex. 20:2103-2113.

LaMantia AS, Rakic P. 1994. Axon overproduction and elimination in the anterior commissure of the developing rhesus monkey. J Comp Neurol. 340(3):328-36.

LaMantia AS, Rakic P. 1990. Axon overproduction and elimination in the corpus callosum of the developing rhesus monkey. J Neurosci. 10(7):2156-2175.

Latora V, Marchiori M. 2001. Efficient behavior of small-world networks. Phys Rev Lett. 87(19):198701.

Lebel C, Beaulieu C. 2011. Longitudinal development of human brain wiring continues from childhood into adulthood. J Neurosci. 31(30):10937-10947.

Lebel C, Gee M, Camicioli R, Wieler M, Martin W, Beaulieu C. 2012. Diffusion tensor imaging of white matter tract evolution over the lifespan. Neuroimage. 60(1):340-352.

Lenroot RK, Gogtay N, Greenstein DK, Wells EM, Wallace GL, Clasen LS, Blumenthal JD, Lerch J, Zijdenbos AP, Evans AC, Thompson PM. 2007. Sexual dimorphism of brain developmental trajectories during childhood and adolescence. Neuroimage. 36(4):1065-1073.

Licht DJ, Wang J, Silvestre DW, Nicolson SC, Montenegro LM, Wernovsky G, Tabbutt S, Durning SM, Shera DM, Gaynor JW, Spray TL, Clancy RR, Zimmerman RA, Detre JA. 2004. Preoperative cerebral blood flow is deminished in neonates with severe congnital heart defects. J Thorac Cardiovasc Surg. 128(6): 841-849.

Limperopoulos C, Soul JS, Gauvreau K, Huppi PS, Warfield SK, Bassan H, Robertson RL, Volpe JJ, du Plessis AJ. 2005. Late gestation cerebellar growth is rapid and impeded by premature birth. Pediatrics. 115:688-695.

Liu P, Chalak LF, Krishnamurthy LC, Mir I, Peng Sl, Huang H, Lu H. 2015. T1 and T2 values of human neonatal blood at 3 Tesla: Dependence on hematocrit, oxygenation, and temperature. Magn Reson Med. 75:1730-1735.

Liu P, Huang H, Rollins N, Chalak LF, Jeon T, Halovanic C, Lu H. 2014. Quantitative assessment of global cerebral metabolic rate of oxygen (CMRO2) in neonates using MRI. NMR Biomed. 27:332-340.

Lord C, Rutter M, Le Couteur A. 1994. Autism Diagnostic Interview-Revised: a revised version of a diagnostic interview for caregivers of individuals with possible pervasive developmental disorders. J Autism Dev Disord. 24:659-685.

Lu H, Clingman C, Golay X, van Zijl PC. 2004. Determining the longitudinal relaxation time (T1) of blood at 3.0 Tesla. Magn Reson Med. 52:679-682.

Marin-Padilla M. 1992. Ontogenesis of the pyramidal cell of the mammalian neocortex and developmental cytoarchitectonics: a unifying theory. J Comp Neurol. 321:223-240.

Massaro AN, Bouyssi-Kobar M, Chang T, Vezina LG, du Plessis AJ, Limperopoulos C. 2013. Brain perfusion in encephalopathic newborns after therapeutic hypothermia. AJNR Am J Neuroradiol. 34:1649-1655.

Maximo JO, Cadena EJ, Kana RK. 2014. The implications of brain connectivity in the neuropsychology of autism. Neuropsychol Rev. 24(1):16-31.

Meek JH, Tyszczuk L, Elwell CE, Wyatt JS. 1998. Cerebral blood flow increases over the first three days of life in extremely preterm neonates. Arch Dis Child Fetal Neonatal Ed. 78:F33-37.

Meynert T. 1872. Vom Gehirn der Saugetiere. Leipzig: Engelmann.

McKinstry RC, Mathur A, Miller JH, Ozcan A, Snyder AZ, Schefft GL, Almli CR, Shimony JS, Shiran SI, Neil JJ. 2002. Radial organization of developing preterm human cerebral cortex revealed by non-invasive water diffusion anisotropy MRI. Cereb Cortex. 12:1237-1243.

Miranda MJ, Olofsson K, Sidaros K. 2006. Noninvasive measurements of regional cerebral perfusion in preterm and term neonates by magnetic resonance arterial spin labeling. Pediatr Res. 60:359-363.

Mori S. 2007. Introduction to Diffusion Tensor Imaging, 1 ed. Elsevier, Italy.

Mori S, Crain BJ, Chacko VP, Van Zijl P. 1999. Three-dimensional tracking of axonal projections in the brain by magnetic resonance imaging. Ann Neurol. 45(2):265-269.

Mori S, Oishi K, Jiang H, Jiang L, Li X, Akhter K, Hua K, Faria AV, Mahmood A, Woods R, Toga AW, Pike GB, Neto PR, Evans A, Zhang J, Huang H, Miller MI, van Zijl P, Mazziotta J. 2008. Stereotaxic white matter atlas based on diffusion tensor imaging in an ICBM template. NeuroImage. 40:570-582.

Mori S, Zhang J. 2006. Principles of diffusion tensor imaging and its applications to basic neuroscience research. Neuron. 51(5):527-539.

Mosconi MW, Mohanty S, Greene RK, Cook EH, Vaillancourt DE, Sweeney JA. 2015. Feedforward and Feedback Motor Control Abnormalities Implicate Cerebellar Dysfunctions in Autism Spectrum Disorder. J Neurosci. 35.

Mukherjee P, Miller JH, Shimony JS, Philip JV, Nehra D, Snyder AZ, Conturo TE, Neil JJ, McKinstry RC. 2002. Diffusion-tensor MR imaging of gray and white matter development during normal human brain maturation. Am J Neuroradiol. 23(9):1445-1456.

Murias M, Webb SJ, Greenson J, Dawson G. 2007. Resting state cortical connectivity reflected in EEG coherence in individuals with autism. Biol Psychiatry. 62(3):270-273.

Nagaraj U.D, Evangelou IE, Donofrio MT, Vezina LG, McCarter R, du Plessis AJ, Limperopoulos C. 2015. Impaired global and regional cerebral perfusion in newborns with complex congenital heart disease. J Pediatr. 167:1018-1024.

Oishi K, Huang H, Yoshioka T, Ying SH, Zee DS, Zilles K, Amunts K, Woods R, Toga AW, Pike GB, Rosa-Neto P. 2011. Superficially located white matter structures commonly seen in the human and the macaque brain with diffusion tensor imaging. Brain Connect. 1(1):37-47.

Oishi K, Zilles K, Amunts K, Faria A, Jiang H, Li X, Akhter K, Hua K, Woods R, Toga AW, Pike GB. 2008. Human brain white matter atlas: identification and assignment of common anatomical structures in superficial white matter. Neuroimage. 43(3):447-457.

Partridge SC, Mukherjee P, Henry RG, Miller SP, Berman JI, Jin H, Lu Y, Glenn OA, Ferriero DM, Barkovich AJ, Vigneron DB. 2004. Diffusion tensor imaging: serial quantitation of white matter tract maturity in premature newborns. Neuroimage. 22(3):1302-1314.

Paus T, Keshavan M, Giedd JN. 2008. Why do many psychiatric disorders emerge during adolescence? Nat Rev Neurosci. 9(12):947-957.

Penagarikano O, Abrahams BS, Herman EI, Winden KD, Gdalyahu A, Dong H, Sonnenblick LI, Gruver R, Almajano J, Bragin A, Golshani P, Trachtenberg JT, Peles E, Geschwind DH. 2011. Absence of CNTNAP2 leads to epilepsy, neuronal migration abnormalities, and core autism-related deficits. Cell. 147:235-246.

Petanjek Z, Judaš M, Šimić G, Rašin MR, Uylings HB, Rakic P, Kostović I. 2011. Extraordinary neoteny of synaptic spines in the human prefrontal cortex. Proc Natl Acad Sci USA. 108(32):13281-13286.

Pierpaoli C, Basser PJ. 1996. Toward a quantitative assessment of diffusion anisotropy. Magn Reson Med. 36(6):893-906.

Pienaar R, Paldino MJ, Madan N, Krishnamoorthy KS, Alsop DC, Dehaes M, Grant PE. 2012. A quantitative method for correlating observations of decreased apparent diffusion coefficient with elevated cerebral blood perfusion in newborns presenting cerebral ischemic insults. Neuroimage. 63:1510-1518.

Rabinowicz T. 1986. The differentiated maturation of the cerebral cortex. in: Falkner, F., Tanner, J.M., (Eds.), Human Growth, Vol. 2. New York: Plenum. pp 385-410.

Radua J, Via E, Catani M, Mataix-Cols D. 2011. Voxel-based meta-analysis of regional white-matter volume differences in autism spectrum disorder versus healthy controls. Psychol Med. 41:1539-1550.

Raichle ME. 1998. Behind the scenes of functional brain imaging: a historical and physiological perspective. Proc Natl Acad Sci USA. 95(3):765-772.

Rakic P. 1972. Mode of cell migration to the superficial layers of fetal monkey neocortex. J Comp Neurol. 145:61-83.

Rakic P. 1988. Specification of cerebral cortical areas. Science. 241:170-176.

Rakic P. 1995. Radial versus tangential migration of neuronal clones in the developing cerebral cortex. Proc Natl Acad Sci USA. 92:11323-11327.

Rakic P. 2009. Evolution of the neocortex: a perspective from developmental biology. Nature Rev Neurosci. 10(10):724-735.

Reveley C, Seth AK, Pierpaoli C, Silva AC, Yu D, Saunders RC, Leopold DA, Frank QY. 2015. Superficial white matter fiber systems impede detection of long-range cortical connections in diffusion MR tractography. Proc Natl Acad Sci USA. 112(21):E2820-8

Rueckert D, Sonoda LI, Hayes C, Hill DLG, Leach MO, Hawkes DJ. 1999. Nonrigid registration using free-form deformations: application to breast MR images. IEEE Trans Med Imaging. 18:712-721.

Rudie JD, Dapretto M. 2013. Convergent evidence of brain overconnectivity in children with autism? Cell Rep. 5(3):565-566.

Satterthwaite TD, Shinohara RT, Wolf DH, Hopson RD, Elliott MA, Vandekar SN, Ruparel K, Calkins ME, Roalf DR, Gennatas ED, Jackson C, Erus G, Prabhakaran K, Davatzikos C, Detre JA, Hakonarson H, Gur RC, Gur RE. 2014. Impact of puberty on the evolution of cerebral perfusion during adolescence. Proc Natl Acad Sci USA. 111:8643-8648.

Sepulcre J, Liu H, Talukdar T, Martincorena I, Yeo BT, Buckner RL. 2010. The organization of local and distant functional connectivity in the human brain. PLoS Comput Biol. 6(6):e1000808.

Schneider JF, Il'yasov KA, Hennig J, Martin E. 2004. Fast quantitative diffusion-tensor imaging of cerebral white matter from the neonatal period to adolescence. Neuroradiology. 46(4):258-266.

Schmahmann JD, Pandya DN. 2008. Disconnection syndromes of basal ganglia, thalamus, and cerebrocerebellar systems. Cortex. 44:1037-1066.

Schmitz N, Rubia K, Daly E, Smith A, Williams S, Murphy DG. 2006. Neural correlates of executive function in autistic spectrum disorders. Biol Psychiatry. 59(1):7-16.

Schüz A, Braitenberg V. 2002. The human cortial white matter: Quantitative aspects of cortico-cortical long-range connectivity. Cortical Areas: Unity and Diversity, eds Schüz A, Miller R (Taylor and Francis, London), 377–385.

Sidman RL, Rakic P. 1973. Neuronal migration, with special reference to developing human brain: a review. Brain Res. 62:1-35.

Sidman RL, Rakic P. 1982. Development of the human central nervous system. Histology and Histopathology of the Nervous System. (IL): Springfield. P. 3-145.

Silbereis JC, Pochareddy S, Zhu Y, Li M, Sestan N. 2016. The Cellular and Molecular Landscapes of the Developing Human Central Nervous System. Neuron. 89:248-268.

Sivaswamy L, Kumar A, Rajan D, Behen M, Muzik O, Chugani D, Chugani H. 2010. A diffusion tensor imaging study of the cerebellar pathways in children with autism spectrum disorder. J Child Neurol. 25(10):1223–1231.

Shaw P, Eckstrand K, Sharp W, Blumenthal J, Lerch JP, Greenstein DE, Clasen L, Evans A, Giedd J, Rapoport JL. 2007. Attention-deficit/hyperactivity disorder is characterized by a delay in cortical maturation. Proc Natl Acad Sci USA. 104(49):19649-19654.

Shrout PE, Fleiss JL. 1979. Intraclass correlations: uses in assessing rater reliability. Psychol Bull. 86:420-428.

Shukla DK, Keehn B, Smylie DM, Muller RA. 2011. Microstructural abnormalities of short-distance white matter tracts in autism spectrum disorder. Neuropsychologia. 49:1378-1382.

Smith SM, Jenkinson M, Johansen-Berg H, Rueckert D, Nichols TE, Mackay CE, Watkins KE, Ciccarelli O, Cader MZ, Matthews PM, Behrens TE. 2006. Tract-based spatial statistics: voxelwise analysis of multi-subject diffusion data. NeuroImage. 31:1487-1505.

Smith SM, Nichols TE. 2009. Threshold-free cluster enhancement: addressing problems of smoothing, threshold dependence and localisation in cluster inference. NeuroImage .44:83-98.

Song SK, Yoshino J, Le TQ, Lin SJ, Sun SW, Cross AH, Armstrong RC. 2005. Demyelination increases radial diffusivity in corpus callosum of mouse brain. Neuroimage. 26(1):132-140.

Sowell ER, Thompson PM, Tessner KD, Toga AW. 2001. Mapping continued brain growth and gray matter density reduction in dorsal frontal cortex: Inverse relationships during postadolescent brain maturation. J Neurosci. 21(22):8819-8829.

Sowell ER, Thompson PM, Toga AW. 2004. Mapping changes in the human cortex throughout the span of life. Neuroscientist. 10(4):372-392.

Sowell ER, Thompson PM, Welcome SE, Henkenius AL, Toga AW, Peterson BS. 2003. Cortical abnormalities in children and adolescents with attention-deficit hyperactivity disorder. The Lancet. 362(9397):1699-1707.

Sowell ER, Bookheimer SY. 2012. Promise for finding brain biomarkers among infants at high familial risk for developing autism spectrum disorders. Am J Psychiatry. 169(6):551-553

Stejskal EO, Tanner JE. 1965. Spin diffusion measurements: spin echoes in the presence of a time-dependent field gradient. J Chem Phys. 42(1):288-292.

Sundaram SK, Kumar A, Makki MI, Behen ME, Chugani HT, Chugani DC. 2008. Diffusion tensor imaging of frontal lobe in autism spectrum disorder. Cereb Cortex. 18:2659-2665.

Supekar K, Uddin LQ, Khouzam A, Phillips J, Gaillard WD, Kenworthy LE, Yerys BE, Vaidya CJ, Menon V. 2013. Brain hyperconnectivity in children with autism and its links to social deficits. Cell Rep. 5(3):738-747.

Thompson PM, Vidal C, Giedd JN, Gochman P, Blumenthal J, Nicolson R, Toga AW, Rapoport JL. 2001. Mapping adolescent brain change reveals dynamic wave of accelerated gray matter loss in very early-onset schizophrenia. Proc Natl Acad Sci USA. 98(20):11650-11655.

Toga AW, Thompson PM, Sowell ER. 2006. Mapping brain maturation. Trends Neurosci. 29(3):148-159.

Toro R, Perron M, Pike B, Richer L, Veillette S, Pausova Z, Paus T. 2008. Brain size and folding of the human cerebral cortex. Cereb Cortex. 18(10):2352-2357.

Travers BG, Adluru N, Ennis C, Tromp DP, Destiche D, Doran S, Bigler ED, Lange N, Lainhart JE, Alexander AL. 2012. Diffusion tensor imaging in autism spectrum disorder: a review. Autism Res. 5(5):289-313.

Varela M, Petersen ET, Golay X, Hajnal JV. 2015. Cerebral blood flow measurements in infants using look–locker arterial spin labeling. J Magn Reson Imaging. 41(6):1591-1600.

Varela M, Hajnal JV, Petersen ET, Golay X, Merchant N, Larkman DJ. 2011. A method for rapid in vivo measurement of blood T1. NMR Biomed. 24:80-88.

Vissers ME, Cohen MX, Geurts HM. 2012. Brain connectivity and high functioning autism: a promising path of research that needs refined models, methodological convergence, and stronger behavioral links. Neurosci Biobehav Rev. 36(1):604-625.

Wakana S, Jiang H, Nagae-Poetscher LM, Van Zijl PC, Mori S. 2004. Fiber tract–based atlas of human white matter anatomy 1. Radiology. 230(1):77-87.

Wakana S, Caprihan A, Panzenboeck MM, Fallon JH, Perry M, Gollub RL, Hua K, Zhang J, Jiang H, Dubey P, Blitz A, van Zijl P, Mori S. 2007. Reproducibility of quantitative tractography methods applied to cerebral white matter. NeuroImage .36:630-44.

Walker L, Gozzi M, Lenroot R, Thurm A, Behseta B, Swedo S, Pierpaoli C. 2012. Diffusion tensor imaging in young children with autism: biological effects and potential confounds. Biol Psychiatry. 72(12):1043-1051.

Wang J, Licht DJ, Jahng GH, Liu CS, Rubin JT, Haselgrove J, Zimmerman RA, Detre JA. 2003. Pediatric perfusion imaging using pulsed arterial spin labeling. J Magn Reson Imaging. 18(4):404-413.

Wang Z, Fernández-Seara M, Alsop DC, Liu WC, Flax JF, Benasich AA, Detre JA. 2008. Assessment of functional development in normal infant brain using arterial spin labeled perfusion MRI. Neuroimage. 39:973-978.

Wass S. 2011. Distortions and disconnections: disrupted brain connectivity in autism. Brain Cogn. 75(1):18-28.

Weinstein M, Ben-Sira L, Levy Y, Zachor DA, Itzhak EB, Artzi M, Tarrasch R, Eksteine PM, Hendler T, Bashat DB. 2011. Abnormal white matter integrity in young children with autism. Hum Brain Mapp. 32(4):534-543.

Wheeler-Kingshott CA, Cercignani M. 2009. About ‘axial’ and ‘radial’ diffusivities. Magnet Reson Med. 61(5):1255-1260.

Williams LA, Gelman N, Picot PA, Lee DS, Ewing JR, Han VK, Thompson RT. 2005. Neonatal brain: regional variability of in vivo MR imaging relaxation rates at 3.0 T- initial experimence. Radiology. 235(2): 595-603.

Wintermark P, Hansen A, Gregas MC, Soul J, Labrecque M, Robertson RL, Warfield SK. 2011. Brain perfusion in asphyxiated newborns treated with therapeutic hypothermia. AJNR Am J Neuroradiol. 32:2023-2029.

Wolff JJ, Gu H, Gerig G, Elison JT, Styner M, Gouttard S, Botteron KN, Dager SR, Dawson G, Estes AM, Evans AC. 2012. Differences in white matter fiber tract development present from 6 to 24 months in infants with autism. Am J Psychiatry. 169(6):589-600.

Woods RP, Grafton ST, Holmes CJ, Cherry SR, Mazziotta JC. 1998. Automated image registration: I. General methods and intrasubject, intramodality validation. J Comput Assist Tomogr. 22:139-152.

Wu WC, St Lawrence KS, Licht DJ, Wang DJ. 2010. Quantification issues in arterial spin labeling perfusion magnetic regionance imaging. Top Magn Reson Imaging. 21(2): 65-73.

Yakovlev PI, Lecours AR. 1967. The myelogenetic cycles of regional maturation of the brain. Regional development of the brain in early life. 3-70.

Yap PT, Fan Y, Chen Y, Gilmore JH, Lin W, Shen D. 2011. Development trends of white matter connectivity in the first years of life. PloS one. 6(9):e24678.

Ye FQ, Frank JA, Weinberger DR, McLaughlin AC. 2000. Noise reduction in 3D perfusion imaging by attenuating the static signal in arterial spin tagging (ASSIST). Magn Reson Med. 44(1): 92-100.

Yu Q, Ouyang A, Chalak L, Jeon T, Chia J, Mishra V, Sivarajan M, Jackson G, Rollins N, Liu S. 2015. Structural development of human fetal and preterm brain cortical plate based on population-averaged templates. Cereb Cortex. bhv201.

Yu Q, Peng Y, Mishra V, Ouyang A, Li H, Zhang H, Chen M, Liu S, Huang H. 2014. Microstructure, length, and connection of limbic tracts in normal human brain development. Front Aging Neurosci. 6:228.

Zhang Y, Zhang J, Oishi K, Faria AV, Jiang H, Li X, Akhter K, Rosa-Neto P, Pike GB, Evans A, Toga AW. 2010. Atlas-guided tract reconstruction for automated and comprehensive examination of the white matter anatomy. Neuroimage. 52(4):1289-1301.

Zhao X, Leotta A, Kustanovich V, Lajonchere C, Geschwind DH, Law K, Law P, Qiu S, Lord C, Sebat J, Ye K, Wigler M. 2007. A unified genetic theory for sporadic and inherited autism. Proc Natl Acad Sci USA 104:12831-12836.

Biographical Information

Minhui Ouang, was born in Guilin, China 1989. She received her Bachelor of Engineering (B.E.) degree from Biomedical Engineering Department, School of Medicine, Tsinghua University, Beijing, China in July, 2011. She began her graduate study in the joint Biomedical Engineering Graduate Program at UTA, UTSW and UTD in Sept 2012. She completed her Ph.D in Dec 2016 from the laboratory of Dr. Hao Huang at Advanced Imaging Research Center (AIRC), UTSW, then Radiology Research at Children's Hospital of Philadelphia, University of Pennsylvania. Her dissertation was titled "Multi-modality magnetic resonance imaging at typical and atypical developmental human brain".

Peer-reviewed Journal Papers

[1] **Ouyang M**, Cheng H, Mishra V, Gong G, Mosconi M, Sweeney J, Peng Y, Huang H, (2016) Atypical age dependent effects of autism on white matter microstructure in children of 2-7 years. *Human Brain Mapping*, 37(2):819-832.

[2] **Ouyang M**, Liu P, Jeon T, Chalak L, Heyne R, Rollins N, Licht D, Detre A, Roberts T, Lu H, Huang H, (2016) Heterogeneous increase of regional cerebral blood flow during preterm brain development: Preliminary assessment with pseudo-continuous arterial spin labeled perfusion MRI. *NeuroImage,* (In Press)

[3] **Ouyang M**, Kang H, Slinger M, Roberts T, Huang H, (2016) Short-range structural and functional connectivity in developmental brains. *Frontiers in Neuroscience,* (abstract accepted)

[4] Feng L, Jeon T, Yu Q, **Ouyang M**, Peng Q, Mishra V, Pletikos M, Sestan N, Miller M, Mori S, Hsiao S, Liu S, Huang H, (2016) Population-averaged macaque brain atlas with high-resolution ex vivo DTI integrated into in vivo space, *Brain Structure and Function*, (under review)

[5] Cao M, Yong H, Dai Z, Liao X, Jeon T, **Ouyang M**, Chalak L, Bi Y, Rollins N, Huang H, (2016) Early development of functional network segregation revealed by connectomic analysis of the preterm human brain. *Cerebral Cortex*, bhw038.

[6] Jeon T, Mishra V, **Ouyang M**, Chen M, Huang H, (2015) Coherent changes of cortical thickness and corresponding white matter microstructure during brain development accessed by diffusion MRI tractography from parecellated cortex. *Frontiers in Neuroanatomy,* 9:158.

[7] Xu H, Zhang D, **Ouyang M**, Hong B, (2013). Employing an active mental task to enhance the performance of auditory attention based brain-computer interfaces. *Clinical Neurophysiology*, 124(1):83-90.

Peer-reviewered Conference Paper and Abstracts

[1] **Ouyang M,** Jeon T, Mishra V, Du H, Wang Y, Peng Y, Hong B, Huang H. “Global and regional cortical connectivity maturation index of developmental human brain with quantification of short-range association tracts.” *Proceedings of ISMRM,* 2016 Singapore

[2] **Ouyang M,** Ouyang A, Yu Q, Chalak L, Huang H. “Distinctive microtructural changes of association white matter tracts during preterm human brain development.” *Proceedings of ISMRM,* 2016 Singapore

[3] **Ouyang M**, Jeon T, Mishra V, Du H, Wang Y, Peng Y, Huang H. “Global and regional cortical connectivity maturation index (CCMI) of developmental human brain with quantification of short-range association tracts.” *Proc. SPIE 9788,* Medical Imaging 2016: Biomeical Applications in Molecular, Structural, and Functional Imaging, 97881B-7.

[4] Jeon T, Sotiras A, **Ouyang M**, Chen M, Chalak L, Davatzikos C, Huang H. “Spatiotemporal dynamics and patterns of cortical mean kurtosis and fractional anisotropy in the preterm brains.” *Proceedings of ISMRM,* 2016 Singapore

[5] Feng L, Li H, Oishi K, Mishra V, **Ouyang M**, Jeon T, Peng Y, Liu S, Huang H. “Age-specific gray and white matter DTI atlas for human brain at 33 and 36 postmenstrual weeks” *Proceedings of ISMRM,* 2016 Singapore

[6] **Ouyang M,** Jeon T, Muller J, Mishra V, Du H, Wang Y, Peng Y, Hong B, Huang H. “Cortical connectivity maturation index human brain based on short-range association tracts.” *OHBM,* 2016 Geneva

[7] Peng Q, Ouyang M, Cao M, Feng L, He Y, Huang H. “Clustering on the functional connectivity strength of preterm human brain” *OHBM,* 2016 Geneva

[8] Feng L, Li H, Oishi K, Mishra V, **Ouyang M**, Jeon T, Lee L, Heyne R, Chalak L, Peng Y, Liu S, Huang H. “Age-specific gray and white matter DTI atlas for human brain at 33, 36 and 39 postmenstrual weeks.” *OHBM,* 2016 Geneva

[9] **Ouyang M,** Jeon T, Mishra V, Du H, Wang Y, Peng Y, Huang H. “Maturation index of developing human brain based on long- and short-range association fibers.” *SPIE Medical Imaging,* 2016 San Diego

[10] **Ouyang M,** Liu P, Lu H, Jeon T, Chalak L, Chia J, Wiethoff A, Rollins N, Huang H. “3D GRASE pseudo-continuous arterial spin labeling (pCASL) of preterm human brain.” *Proceedings of ISMRM,* 2015 Toronto

[11] Mishra V, Oishi K, Li H, Jeon T, **Ouyang M**, Chalak L, Chia JM, Peng Y, Rollins N, Mori S, Huang H. “Population-averaged age-specific DTI templates of preterm human brain at 33, 36 and 39 gestational weeks”. *Proceedings of ISMRM,* 2015 Toronto

[12] Cao M, Jeon T, Dai Z, Liao X, **Ouyang M**, Chalak L, He Y, Huang H. “Early development of functional connectome in preterm infants”. *OHBM,* 2015 Hawaii

[13] **Ouyang M,** Cheng H, Gong G, Mosconi M, Seeney J, Peng Y, Huang H. “Abnormal WM microstructural trajectories of autistic children from 2 to 7 years of age.” *Proceedings of ISMRM,* 2014 Milan

[14] **Ouyang M,** Liu P, Lu H, Chalak L, Chia J, Wiethoff A, Rollins N, Huang H. “Exploring spatiotemporal dynamics of the cerebral blood flow of perinatal human brains with arterial spin labeling.” *Proceedings of ISMRM,* 2014 Milan

[15] **Ouyang M,** Rao U, Gundapuneedi T, Huang H. “Integration of functional and structural connectivity from resting state fMRI and DTI to study healthy maltreated adolescents.” *Proceedings of ISMRM,* 2013 Utah

[16] Gao H, **Ouyang M**, Zhang D, Hong B. “An auditory brain-computer interface using virtual sound field.” In *Engineering in Medicine and Biology Society, EMBC, 2011 Annual International Conference of the IEEE,* 4568-4571.